Annealing induced recrystallization of radiation damaged titanite and allanite

Dissertation
zur Erlangung des Doktorgrades
der Naturwissenschaften im Fachbereich
Geowissenschaften
der Universität Hamburg

vorgelegt von

Tobias Beirau
aus Glinde

Hamburg
2012

Als Dissertation angenommen vom Fachbereich Geowissenschaften der Universität Hamburg

auf Grund der Gutachten von Prof. Dr. Ulrich Bismayer
und Dr. habil. Boriana Mihailova

Tag der mündlichen Prüfung: 29.06.2012

Hamburg, den 14. Mai 2012

Prof. Dr. Oßenbrügge
Sprecher Fachbereich Geowissenschaften

Contents

Abstract

Minerals can become metamict over geological time periods as a result of structural damage induced by α-decay events resulting from incorporated radiogenic elements. The structural state and the thermally induced recrystallization behavior of metamict titanite were studied by Raman spectroscopy, synchrotron single-crystal X-ray diffraction, nanoindentation and complementary high-resolution transmission electron microscopy.

The results of the Raman spectroscopic measurements show that Raman scattering collected from metamict titanite is still anisotropic, which is typical of single crystals and indicates oriented, basically coherent structural elements. The observed Raman scattering dependence on the sample orientation is on the other hand much more pronounced for heavily metamict than for weakly metamict titanite samples. Radiation-induced anisotropic effects are related to the specific atomic arrangements in the structure of metamict titanite. This leads to the opportunity to study separately the structural transformations of the crystalline and amorphous fractions in metamict titanite by using Raman spectroscopy. That is possible because the Raman modes in the spectra collected from a plane nearly perpendicular to the chains of corner-sharing TiO_6 octahedra arise predominantly from phonon modes in crystalline nanoregions with radiation-induced defects. In contrast to the contribution of atomic vibrations in radiation-induced amorphous nanoregions, which is better pronounced in spectra collected from a plane containing TiO_6 chains. The results show that radiation-induced periodic faults in the crystalline matrix are related to the disturbance of SiO_4-TiO_6-SiO_4-TiO_6 rings comprising TiO_6 octahedra from different chains. The radiation-induced amorphization by contrast is related to the partial change of Ti coordination from octahedral to pyramidal and/or tetrahedral, which leads to a rising Ti-O bond strength. This in turn violates the Ti-O-Ti intrachain linkages in the titanite structure. Hence, the planes containing Si-O-Ti-O bond rings are less susceptible to a self-accumulation of radiation-induced defects resulting in the development of amorphous regions as compared to the perpendicular plane containing Ti-O bond chains. Multistep annealing gradually suppresses the structural defects in the crystalline fraction of the titanite as the improvement of the SiO_4-TiO_6 connectivity within planes near perpendicular to the

TiO_6 chains reaches saturation near 900 K. Annealing-induced recrystallization of the radiation-induced amorphous nanoregions takes place in the temperature range between approximately 650 and 950 K, with a maximum near 750 K.

To determine the influence of radiation damage on the behavior of the elastic material properties of titanite, nanoindentation measurements were performed on partially metamict titanite (sample E2312) and for comparison additionally on nearly undamaged crystalline titanite (Rauris sample) and titanite glass. Metamict titanite E2312 shows hardness (H) and elastic modulus (E) values close to those of titanite glass. Rauris titanite shows strong anisotropy and the H and E values are clearly larger than those of E2312. Thermally induced stepwise recrystallization of metamict titanite E2312 leads to a decrease in the hardness until approximately 950 K and afterwards to an increase at higher temperatures, while the elastic modulus increases continuously (H and E values measured always at room temperature). Changes of the hardness and elastic modulus are related to increasing long-range order and vanishing amorphous interface areas in the titanite structure.

In further studies the structural recovery of the metamict epidot group mineral allanite (sample number R1) produced by thermal annealing was followed by powder X-ray diffraction, single-crystal synchrotron X-ray diffraction and infrared spectroscopy.

Allanite contains in contrast to titanite structural OH groups. But no evidences for a marked influence of this OH groups on the recrystallization behavior were found. Corresponding to structural recovery the measured high-temperature annealing XRD patterns and IR spectra of metamict allanite R1 reveal a marked increase in correlation length. The structural recovery of the allanite is also indicated by a detected decrease in the unit-cell volume during annealing. The synchrotron X-ray diffraction results show, that major changes in the crystallinity of metamict allanite occur within the first hour of annealing. A kinetic analysis following Sharp-Hancock points to the fact, that the recrystallization process follows at least two different structural mechanisms of reorganization. During the annealing experiments at 823 and 1073 K, no chemical decomposition of allanite was observed.

1 Introduction

Nuclear waste forms

The management of nuclear waste forms and their permanent disposal is of rising importance because the amount of nuclear power stations worldwide is still expected to increase (Joskow and Parsons, 2012). Over the last 70 years the quantity of generated Pu and other actinides as for instance Np, Am and Cm produced in nuclear reactors has reached more than 2000 tons (Ewing, 2011). The global production of Pu in reactors amounts to approximately 70 - 80 t/year (Ewing, 2008, 2011). Nuclear reactors mostly use ^{235}U (half-life = 7.04 * 10^8 years) and ^{239}Pu (half-life = 2.4 * 10^5 years) as main sources for fission energy; these isotopes are also used as the fissile material in nuclear weapons (Ewing, 2011). The fission of ^{235}U and ^{239}Pu generates short-lived fission product elements like ^{137}Cs and ^{90}Sr with half-lives of approximately 30 years but also more stable radioactive elements like ^{99}Tc and ^{129}I with half-lives of 213000 years and 16 million years (Ewing, 2008). The major part of spent nuclear fuel (SNF) is UO_2, but particularly the formed transuranium elements with long half-lives such as ^{239}Pu and ^{237}Np (half-live = 2.1 * 10^6 years) which amount to ~1 at.% of the UO_2 in SNF, have a massive influence on nuclear-waste management strategies, because together with the isotopes of U, they cater for most of the radiotoxicity after 1000 years (Ewing, 2008, 2011).

The current strategy to deal with the SNF and nuclear waste forms is to store them in geological repositories (Ewing, 2007a, 2008, 2011). Another possibility is to ‘burn’ or reduce the inventories of separated higher-quality Pu and minor actinides in ‘burner’ reactors, using fast neutrons, to produce mixed oxide (MOX) fuel (made up of U and Pu) or to incorporate actinides in an inert matrix fuel (IMF) (Ewing, 2007a, 2008, 2011). After a once-through burn-up the MOX and IMF used fuels will be disposed in a geologic repository, too (Ewing, 2007a). Finding a suitable geological repository for the nuclear waste is still a great challenge.

A frequently investigated possibility for immobilizing actinides separated from spent nuclear fuel is the embedding in suitable long-term physical and chemical durable mineral-based ceramic materials (Weber et al., 1997, 1998; Muller et al., 2001; Farnan

et al., 2007), e.g. titanite (Stefanovsky et al., 2000; Vance et al. 2000; Muller et al., 2001). Necessarily possible materials for immobilizing actinides should be able to incorporate considerable amounts of neutron absorbers like Gd and Hf into their structure (Vance et al., 2000). Also they should ensure extremely small leaching rates of incorporated actinides and neutron absorbers (Vance et al., 2000). In order to develop embedding techniques several complex oxides, including silicates (e.g. zircon and titanite) and niobates (e.g. pyrochlore) have been investigated (Ewing, 2007a, 2008).

Radiation damage

In minerals, actinides can occur as natural constituents of the crystal structure. After some time the long-range ordered crystal structure is destroyed by self-radiation damage resulting from α- and β-decay events of the radiogenic impurities and becomes metamict (Ewing et al., 1988; Hawthorne et al., 1991; Weber et al., 1997, 1998, 2009; Muller et al., 2001; Farnan et al., 2007; Ewing, 2007b, 2011). During an α-decay event in crystalline materials the periodically ordered structure is damaged by two different types of particle, the α-particle ($^{4}_{2}He^{2+}$) and the 'recoil nucleus' (Hawthorne et al., 1991; Ewing, 2007b, 2011). The small α-particle displaces only several hundreds of atoms by elastic collisions on its way of 15 – 22 μm (most of all close to its end of range) releasing most of its energy (4.5 – 5.8 MeV for actinides) by ionization processes which form Frenkel defects in the material (Hawthorne et al., 1991; Ewing, 2007b, 2011). The heavier 'recoil nucleus' has a lower kinetic energy (86 keV for ^{235}U recoil from decay of ^{239}Pu) but it leads to a displacement of several thousands of atoms because nearly all of its energy will be evolved in elastic collisions with other atoms on its path of 30 – 40 nm length through the crystal lattice (Ewing, 2007b, 2011). In zircon ($ZrSiO_4$) approximately 5000 atoms are displaced per decay event (Salje et al., 2012). This leads to atomic recoil or collision cascades in the system and from overlapping and interacting with the defects in the lattice, aperiodic regions will emerge (Hawthorne et al., 1991; Trachenko et al., 2001; Ewing, 2007b). For comparison a β-decay event leads to only 0.1 displacements (Ewing, 2011). These radiation induced structural amorphization processes generate the metamict state (Hawthorne et al., 1991; Ewing,

1994), which is characterized by a high degree of structural disorder with coexisting defect-rich crystalline and amorphous nanoregions (Salje et al., 2011b). The metamict state is a metastable thermodynamic state and a structural recovery can be induced by thermal annealing (Vance and Metson, 1985; Hawthorne et al., 1991; Paulmann et al., 2000; Zhang et al., 2002). Annealing leads to the recrystallization of the radiation-amorphized nanoregions and the suppression of the inherent structural defects (Frenkel defects and other local defects) in the crystalline fraction of the metamict sample (Janeczek and Eby, 1993; Ewing, 1994; Paulmann et al., 2000; Zhang et al., 2002; Bismayer et al., 2010, Salje et al., 2011b, 2012).

Natural U- and Th-containing metamict minerals (e.g. zircon, titanite, allanite and pyrochlore) which were exposed to nuclear radiation over geological timescales (in most cases for ~ 1 Ga or longer) are considered to be possible analogues to obtain a better understanding of the long-term effects of radiation on condensed matter, which might be used for encapsulating and immobilizing nuclear waste forms (Ewing et al., 1988, 2000; Ewing, 2007a). This work is focused on the structural features of the natural metamict minerals titanite and allanite.

Titanite

Titanite, also referred to as sphene (Taylor and Brown, 1976), is an accessory mineral with the nominal chemical composition $CaTiSiO_5$. It occurs in metamorphic and igneous rocks and can incorporate various impurities (Higgins and Ribbe, 1976). The ideal titanite structure (Figure 1) consists of chains of corner-sharing TiO_6-octahedra, cross-linked by isolated SiO_4-tetrahedra forming a $TiOSiO_4$ framework which hosts Ca^{2+} ions in irregular sevenfold coordinated polyhedra (Speer and Gibbs, 1976).

At room temperature (RT) pure titanite crystallizes in the monoclinic space group $P2_1/a$ (standard setting $P2_1/c$) and is antiferroelectric as a result of Ti^{4+}-cation off-center displacements inside the TiO_6 octahedra which are in the same direction within a single chain but opposite between two adjacent chains (Speer and Gibbs, 1976; Taylor and Brown, 1976; Zhang et al., 1995; Kek et al., 1997; Salje et al., 2011b). Near 500 K pure titanite undergoes a displacive phase transition to the monoclinic paraelectric space

group A2/a (standard setting C2/c) due to the loss of antiferroelectric coupling of the Ti off-centered displacements from different chains (Speer and Gibbs, 1976; Taylor and Brown, 1976; Bismayer et al., 1992; Salje et al., 1993; Zhang et al., 1995; Kek et al., 1997; Malcherek et al., 2001). Near 825 K a subsequent isosymmetrical phase transition occurs consisting of decoupling of the Ti off-centered displacements within a chain (Salje et al., 1993; Zhang et al., 1997; Kek et al., 1997; Chrosch et al., 1997; Malcherek et al., 1999, 2001). Because of the presence of impurities and faults the room temperature antiferroelectric ordering is destroyed in natural metamict titanites and therefore, at ambient conditions the average crystal structure of metamict titanite has the paraelectric space group A2/a (C2/c) (Higgins and Ribbe, 1976; Speer and Gibbs, 1976; Hughes et al., 1997; Bismayer et al., 1999).

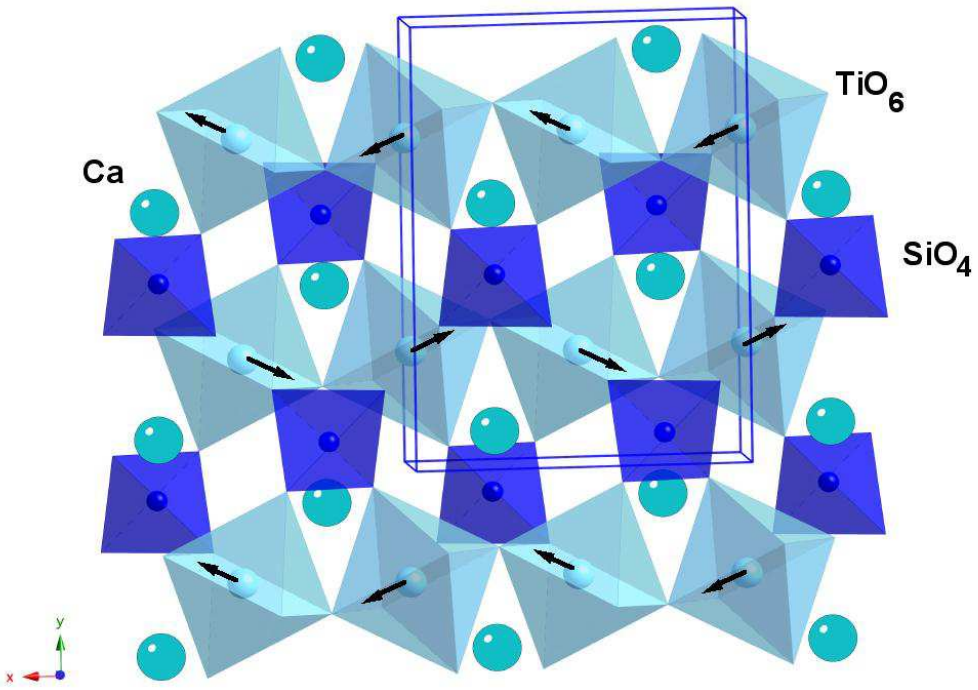

Figure 1: Crystal structure of titanite $CaTiSiO_5$. The arrows indicate the direction of Ti position displacements in the $P2_1/a$ space group (image created using CrystalMaker).

In nature, the Ca atoms in the titanite structure may be replaced by various impurities like Na, REEs, Y and the radiogenic elements U and Th (Hawthorne et al., 1991). The incorporated amount of U and Th could vary from a few hundred up to a few thousand ppm (Ewing et al., 2000). Through the α-decay events of these elements the periodically ordered structure becomes partially destroyed and hence metamict (Hawthorne et al., 1991; Salje et al., 2011b). This leads to coexisting of crystalline and amorphous nanoregions as seen by high resolution transmission electron microscopy (HR-TEM) (Lumpkin et al., 1991; Hawthorne et al., 1991). Decay-induced Frenkel-defect pairs and increased atomic distances in the structure lead to the swelling of the crystalline matrix of about 3% (Chrosch et al., 1998; Salje et al., 2012).

It has been proposed that the radiation induced modification of the structure of titanite follows the so-called direct impact mechanism (Salje et al., 2012). According to this model a direct impact (induced by α-decay and recoil effect) damages the crystalline structure and leaves a recoil region with thousands of displaced atoms (Salje et al., 2012). By overlapping of several of these regions, percolation paths are generated in two steps (Salje et al., 2012). At the first percolation transition only the crystalline matrix percolates, whereas at the second, both crystalline and amorphous parts of the structure percolate (Salje et al., 2011a).

$CaTiSiO_5$ may incorporate in its structure up to 21.5 wt.% Gd_2O_3 (0.25 formula units (f.u.) Gd^{3+}) and 9.3 wt.% UO_2 (0.07 f.u. U^{4+}) as Gd and U substitutable for Ca (Stefanovsky et al., 2000). The solid solubility limits of U, Pu and the neutron absorbing elements Hf and Gd for titanite have been determined by Vance et al. (2000). They found solubilities of 0.02 f.u. Pu^{4+}, of 0.05 f.u. Pu^{3+} and 0.5 and 0.3 f.u. Hf and Gd, respectively.

In addition, the octahedrally coordinated Ti position can be occupied by impurity cations for example Al, Fe, Ta and Nb (Paul et al., 1981; Hollabaugh and Foit, 1984; Muir et al., 1984; Groat et al., 1985; Hawthorne et al., 1991; Chrosch et al., 1998). The tetrahedrally coordinated Si in the titanite structure can be substituted by Ti atoms (Hollabaugh and Rosenburg, 1983) and structural O^{2-} can be replaced by $(OH)^-$ and F^- (Hawthorne et al., 1991; Meyer et al., 1996), when a charge compensation of vacancies or cation substitution effects is required.

Using Mössbauer spectroscopy it has been shown that even the radiation-amorphized regions exhibit a significant degree of short-range order (Salje et al., 2011a). An increased disorder in vicinity of the Ti positions in metamict titanite with increasing degree of metamictization and a partial reduction of the Ti coordination from sixfold to five- and/or fourfold has been assumed from the results of X-ray absorption spectroscopic (XAS) analyses (Hawthorne et al., 1991; Farges et al., 1997). On the basis of infrared spectroscopic (IRS) measurements Zhang et al. (2002) proposed the possible existence of TiO_5 complexes in heavily metamict titanite.

Annealing experiments on metamict minerals can give further knowledge about the structural stability and the mesoscopic-scale atomic rearrangements in radiation-damaged materials. Infrared spectroscopy of titanite samples with various degrees of metamictization clearly demonstrated the reduction of defects on the short-range length scale at elevated temperatures (Zhang et al., 2002). Synchrotron single-crystal X-ray diffraction (XRD) measurements of heavily metamict titanite samples showed a significant increase in the correlation length on the long-range scale above 650 K and a decrease of the unit-cell volume (Paulmann et al., 2000).

By resonance-ultrasound-spectroscopy of radiation-damaged titanite a massive softening of the shear moduli in the annealing range from 600-1000 K and a huge hardening at annealing temperatures above 1000 K have been detected (Salje et al., 2011b). Recrystallization occurs in metamict titanite at annealing temperatures above 575 K (Salje et al., 2011b, 2012). Hence, via thermal annealing in the temperature range of 575 - 1000 K amorphized recoil beads, the metamict sections of the sample, embedded in the crystalline matrix of the metamict titanite structure begin to shrink by about 3% as a result of recrystallization, but the interfacial mismatch prevents the reconstruction of a fully coherent lattice. The resulting volume reduction of the amorphized beads leads to a disconnection from the crystalline matrix, referred to as ‘rattling’. Hence, the shrinked recrystallized areas can lead to increased interatomic distances (‘holes’) in the matrix which consequently becomes porous. Annealing temperatures above 1000 K activate grain growth effects in the material which lead to the disappearance of the mismatched or so called soft interfaces and a coherent lattice can be developed, therefore the sample hardens (Salje et al., 2011b, 2012).

Allanite

Allanite is a sorosilicate mineral belonging to the epidote group and occurs in metamorphic and magmatic rocks. The general chemical allanite composition is $(Ca,Ce,REE)_2(Fe^{2+},Fe^{3+})(Al,Fe^{3+})_2O[Si_2O_7][SiO_4](OH)$ (Janeczek and Eby, 1993). The allanite structure is characterized by octahedral-tetrahedral framework topology (Figure 2). The framework consists of two types of chains of edge-sharing octahedra extending parallel to the b axis: a chain of M2 octahedra and a chain of M1 and M3 octahedra. The octahedrally-coordinated M1 and M2 sites can be occupied by cations inclusive Fe^{3+}, Al^{3+} and Mn^{3+}. The M3 position in the crystal structure can be occupied by Fe^{2+}, Fe^{3+} and Ti. The octahedral chains are cross-linked by SiO_4 (Si3 site) and Si_2O_7 (Si1 and Si2 sites) groups which together with the octahedra form two extraframework coordination polyhedra (A1 and A2) which can be occupied by Ca, Mn, Ce, La, Y, Th or other cations (Dollase, 1971; Hawthorne, 1987; Janeczek and Eby, 1993). A large range of substitutions has been recorded and more than 25 wt.% of REE can be occupied at the cation sites. The mineral allanite crystallizes in the monoclinic space group $P2_1/m$ with lattice unit-cell parameters, depending on the chemical composition, of a = 8.9 - 9.0 Å, b = 5.7 - 5.8 Å, c = 10.1 - 10.2 Å; β = 114.8 - 116.0º (Paulmann and Bismayer, 2001). It commonly shows thermoluminescence due to defects and impurities (Mitchell, 1973). Allanite becomes metamict as a result of structural damage produced by α- and β-decay of incorporated U and Th, as described in the chapter 'Radiation damage'. The degree of this damage depends on the individual radiation dose (Ewing, 1987; Ewing et al., 1987; Malczewski and Grabias, 2008). Similar to other radiation damaged materials, thermal annealing of metamict allanite results in partial recrystallization and structural recovery. The thermal behavior and recrystallization process in allanite strongly depends on the degree of the radiation damage as well as on the annealing atmosphere (Janeczek and Eby, 1993). Heating the mineral to 1273 K destroys its crystal structure completely (Cobic et al., 2010). In contrast to other well studied metamict minerals like zircon ($ZrSiO_4$) (Weber, 1990) or titanite ($CaTiSiO_5$) (Hawthorne et al., 1991), allanite contains OH groups in its crystal structure which were usually considered to act as a catalyst in the thermal recrystallization of metamict minerals (Zhang et al., 2000). The recrystallization of metamict allanite in air may lead to simultaneous oxidation of the

divalent octahedrally coordinated cations which favors the loss of structural OH groups or absorbed water (Bonazzi and Menchetti, 1994; Cobic et al., 2010).

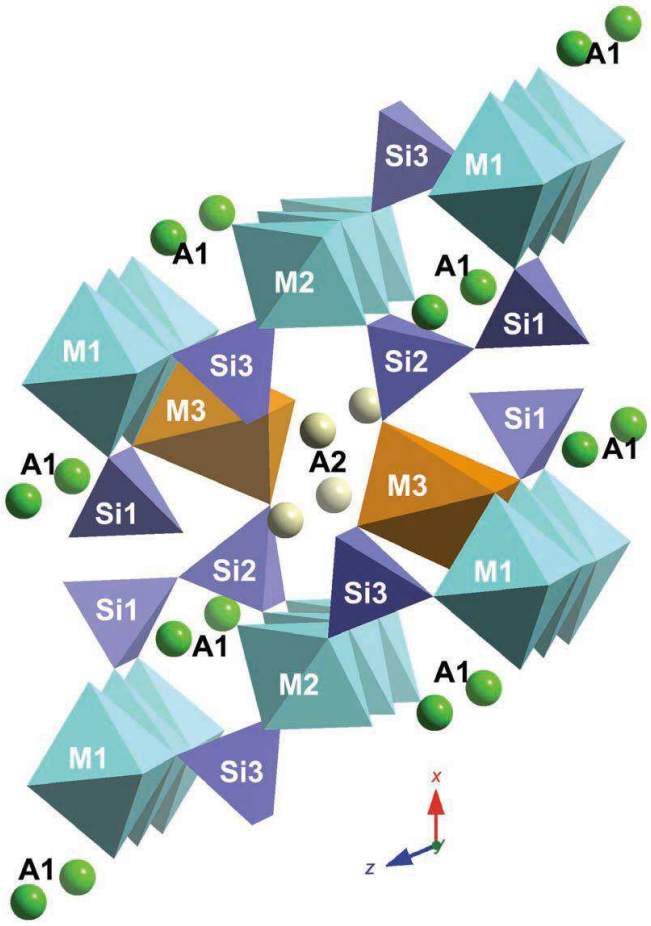

Figure 2: Crystal structure of allanite viewed along [010] (image created using CrystalMaker).

Objectives of the current study

The aim of this work is to study the influence of long-term nuclear radiation on the atomic structure of crystalline materials and to obtain a better understanding of thermally induced recrystallization processes in them. The metamict minerals titanite and allanite have been chosen as model systems because of their characteristic radiation-induced amorphization and local structural features related to materials proposed for nuclear waste immobilization. In contrast to titanite, allanite contains OH groups in its structure. To gain a deeper insight into the processes occurring during self-radiation damage and thermally induced recrystallization, the study of metamict minerals is essential for finding suitable matrix materials for the safety long-term disposal of actinide bearing waste forms. To investigate the metastable metamict state, especially the kinetically driven recrystallization and the resulting structural transformations in situ analytical techniques were used: synchrotron single-crystal X-ray diffraction (XRD), Raman spectroscopy, infrared (IR) spectroscopy, transmission electron microscopy (TEM) and nanoindentation. Vibrational spectroscopy was used because it has a length-scale of sensitivity of a few unit cells and it has therefore been used for studying amorphous and nanometric materials. Synchrotron X-ray diffraction allows on the other hand to obtain a picture integrated over the mesoscopic scale of materials to disentangle their long-range order.

2 Experimental techniques and theoretical background

Sample characterization and preparation

Titanite samples

Reference samples

As a reference material, nonmetamict titanite from Rauris, synthetic titanite (Tanaka et al., 1988) and titanite glass were used. The titanite glass was synthesized in a Pt/Ir crucible by annealing polycrystalline titanite at ca 1700 K for 2 min with a hydrogen burner and subsequent quenching in air to room temperature (RT). The preservation of the chemical stoichiometry in the glass was verified by electron microprobe analysis (Camebax microbeam SEM system), averaging over 100 spatial points. The natural undamaged titanite sample from Rauris in Austria (Rauris titanite) has a light green color and contains Fe (1.8%) and Al (3.8%) (Meyer et al., 1996).

Metamict titanite samples

The natural metamict titanite samples used in this study stem from the collection at the Department of Mineralogy, Royal Ontario Museum (ROM), Toronto, Ontario, Canada. Their catalogue numbers and localities are M28696, also referred to as Cardiff, (Cardiff U-mine, Ontario, Canada), M28173 (Gjerstad, Norway) and M28658 (Maevatanana, Republic of Madagascar). These samples have been thoroughly analyzed by other research groups using various methods, including microprobe analysis, XRD, Mossbauer spectroscopy, infrared spectroscopy etc. (Vance and Metson, 1985; Hawthorne et al., 1991; Zhang et al., 2000, 2002; Bismayer et al., 2010; Salje et al., 2011a, 2012). Heavily metamict titanite is rather inhomogeneous and this is probably the reason for the variation in the U and Th content of titanite from the Cardiff locality (ROM catalogue number M28696) reported in different papers (Hawthorne et al., 1991; Chrosch et al., 1998; Salje et al., 2012). The concentration of U in sample M28173

given by Hawthorne et al. (1991) was astonishingly high (2620 ppm), for that reason it was remeasured in this work by microprobe analysis, using a Cameca microbeam SX100 SEM system, 15 keV, 40 nA, a beam spot diameter on the same surface approximately 1 μm and averaging over 10 points. The analysis indeed revealed an U content which is lower than that for sample M28696 (Table 1) and thus better matches the index of structural damage estimated from XRD and IRS analysis. According to Hawthorne et al. (1991) the damage index (a parameter ranging from 1 to 10 and denoting increased structural damage or decreased crystallinity, estimated from the peak resolution in powder XRD patterns) is 3, 8 and 10 (greatest) for samples M28658, M28173 and M28696, respectively. In Table 1 the main characteristics of the samples are summarized.

Metamict titanite with the ROM catalogue number E2335 was chosen as a model metamict titanite for studying the annealing-induced structural alteration because this sample exhibits phase homogeneity on the length scale of XRD sensitivity and a relatively low degree of chemical impurities (Salje et al., 2011b; Hawthorne et al., 1991). Salje et al. (2011a) determined the fraction of the amorphized material in E2335 to be 0.24. The crystals are black to black-brown and become brownish transparent during annealing. The E2335 titanite sample (Table 1) contains 135 ± 24 ppm U and 764 ± 141 ppm Th (Salje et al., 2012).

The metamict titanite sample with the catalog number E2312 stems from the locality Sebastapol Township, Ontario, Canada (Hawthorne et al. 1991). According to the damage index scale defined by Hawthorne et al. (1991) from 1 to 10 (where 10 is the maximum), denoting increasing structural damage in the crystal by radiogenic irradiation, the E2312 sample has a damage index of 6 concerning to powder X-ray measurements and an index of 7 concerning to powder infrared measurements (Hawthorne et al., 1991) (Table 1). The metamict titanite sample E2312 contains 182 ± 13 ppm U, 768 ± 57 ppm Th, 1.64 wt.% F and 2.89 wt.% Fe_2O_3 (Hawthorne et al., 1991; Salje et al., 2012). It has been dated at approximately 1053 Ma by using U-Pb isotopic data (Salje et al., 2012). The black to black-brown crystals became brownish transparent after annealing and showed a glassy luster.

Table 1: Chemical and structural characteristics of the studied metamict samples.

ROM catalogue number	U (ppm)	Th (ppm)	Reference	Age (Ma)	Reference	Damage index [a]		Dose [b] (10^{18} α-event/g)	F (wt.%) [a]	Fe_2O_3 (wt.%) [a]
						XRD	IR			
M28658	22	1	Hawthrone et al. (1991)	2502 [c]	Tucker et al. (1999)	3	3	0.2 [d]	0.27	0.6
E2335	135±24	764±141	Salje et al. (2012)	1086	Salje et al. (2012)	9	8	1.19±0.22	0.34	1.35
M28173	305±100	410±110	our data	1000 [c]	Vance and Metson (1985)	8	9	1.4±0.4	1.21	3.66
M28696	473±64	498±56	Salje et al. (2012)	1035	Salje et al. (2012)	10	10	2.17±0.29	2.68	3.57
E2312	182±13	768±57	Salje et al. (2012)	1053	Salje et al. (2012)	6	7	1.33±0.1	1.64	2.89

[a] after Hawthrone et al. (1991);

[b] calculated after Nasdala et al. (2001); the uncertainties are calculated from the uncertainties in the U and Th contents;

[c] the time used to calculate the dose was approximated with the age of the rocks from the same type and locality given in the corresponding papers;

[d] no available literature data about the uncertainties in the U and Th contents.

Radiation Dose calculation

The Doses (D_α) (number of α-decay events per mg) of the metamict titanite samples shown in Table 1 were calculated after Nasdala et al. (2001) from

$$D_\alpha = 8 \cdot \frac{c_U \cdot N_A \cdot 0.9928}{M_{238} \cdot 10^6} \cdot \left(e^{\lambda_{238} t} - 1\right) + 7 \cdot \frac{c_U \cdot N_A \cdot 0.0072}{M_{235} \cdot 10^6} \cdot \left(e^{\lambda_{235} t} - 1\right) + 6 \cdot \frac{c_{Th} \cdot N_A}{M_{232} \cdot 10^6} \cdot \left(e^{\lambda_{232} t} - 1\right) \quad (2.1)$$

Were the coefficients 8, 7 and 6 are related to the number of α-decays per nucleus (Geisler-Wierwille, 1999), c_U and c_{Th} are the actinide concentrations in ppm (Table 1), N_A is Avogadro's number (≈ 6,022*10^{23} mol^{-1}) and M_{238} (=238.05 u), M_{235} (=235.04 u) and M_{232} (=232.04 u) are the molecular weights of the parent isotopes. λ_{238} (=1.55125*10^{-10} a^{-1}), λ_{235} (=9.84850*10^{-10} a^{-1}) and λ_{232} (=0.49475*10^{-10} a^{-1}) are the decay constants (Steiger and Jäger, 1977) and t is the sample age (Table 1). A present U composition of 99.28% ^{238}U and 0.72% ^{235}U is presumed. (Nasdala et al., 2001)

Allanite sample

Metamict allanite samples from the collection of the Fersman Mineralogy Museum of the Russian Academy of Sciences in Moscow, Russia, were studied. The sample number of the allanites is R1 and the locality is Savvushka, Altai, Russia. The metamict allanite sample R1 contains approximately 2.87 wt.% ThO_2 and 18.4 wt.% REE oxides (Table 3). The crystals are black-brown to black, opaque and have a vitreous luster. Massive postcollisional alkaline granite intrusions were emplaced between the Permian and Jurassic periods in the northern Altai Mountains (Jahn et al., 2000). The zircon in these rocks has been dated at 200 - 250 Ma using U - Pb and Rb - Sr isochrones (Vladimirov et al., 1997).

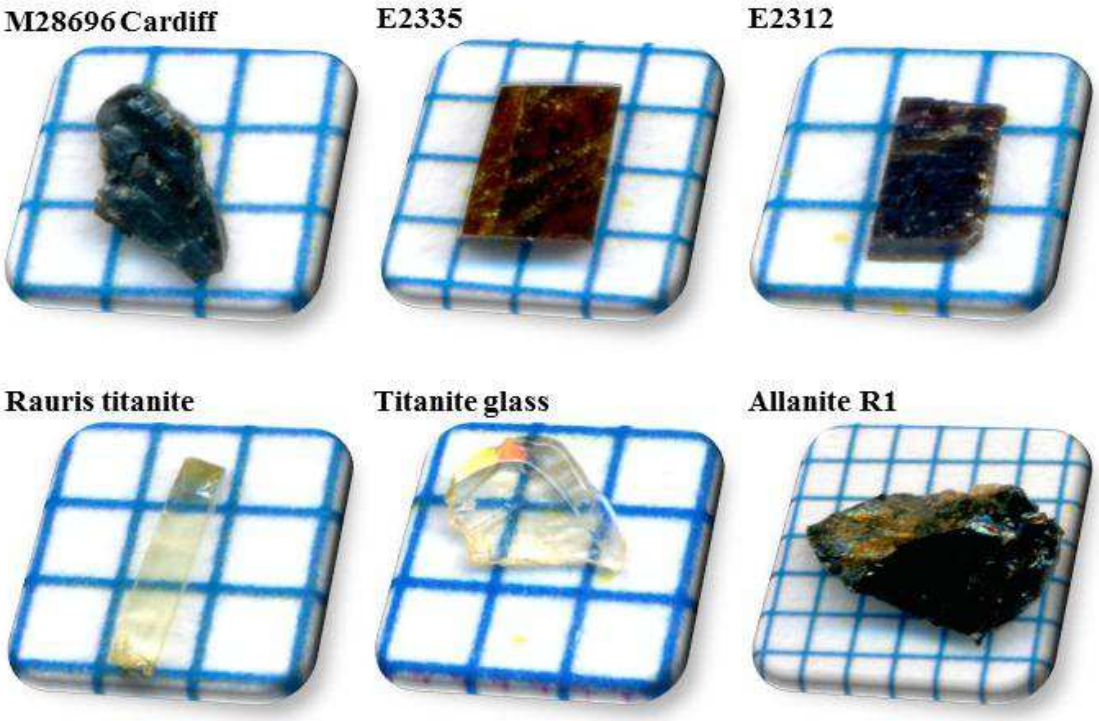

Figure 3: Photographs of selected titanite and allanite samples. Each blue square has a size of 1 mm^2.

Raman spectroscopy

Theory

The following summary of Raman scattering phenomena follows previous descriptions by Kiefer (1995), Putnis (1992) and Bismayer (1990).

In the year 1928 the Raman effect, a process of inelastic light scattering, was discovered by Raman and Krishnan (1928). Classically described, the electromagnetic field of an incident light source (usually a monochromatic laser beam) induces an instantaneous dipole moment in a molecule, by deforming the surrounding electron cloud, hence a change of polarization occurs. The induced dipole moment subsequently oscillates with the frequency of the incident light and emits radiation with the same frequency, which is called Rayleigh scattering.

The electric vector of the incident radiation

$$E = E_0 \cos \omega_0 t \tag{2.2}$$

induces the dipole moment in the scatterer, given by

$$\mu = \alpha E \tag{2.3}$$

where α is the polarizability of the system, E_0 the amplitude and ω_0 is the angular frequency of the incident electric field.

(2.2) inserted into (2.3) leads to (Kiefer, 1995)

$$\mu = \alpha E_0 \cos \omega_0 t. \tag{2.4}$$

During the light scattering process most of the incident light is elastically scattered, without a change in energy. A small part of the photons of the incident light also interacts inelastically with optical vibrational modes (optical phonons in crystalline solids) of the molecules or the crystal lattice of the scatter medium which leads to a

periodic modification of the polarizability in the system. Hence, the oscillation of the induced dipole moment is modulated by self-oscillations of the scatter medium. As a result additional inelastic light scattering occurs and the scattered light will contain additional frequency components (see equation (2.7)).

The normal vibrations of a molecule or a lattice are described by the model of a harmonic oscillator, according to which the time-related change of the amplitude of vibration is given by

$$q = q_0 \cos \omega_R t \tag{2.5}$$

where q is the classical atomic displacement amplitude of the given vibrational mode, ω_R the circular frequency and t the time (Kiefer, 1995).

The polarizability of the system follows this oscillation and as a result of the very small changes in the bond length during the vibration, it can be developed around the equilibrium position q = 0 (Kiefer, 1995)

$$\alpha = \alpha(q) = \alpha_0 + \left(\frac{\partial \alpha}{\partial q}\right)_0 q + \cdots \tag{2.6}$$

Inserting (2.5) in (2.6) and afterwards (2.6) in (2.4) leads, after trigonometric transformation, to (Kiefer, 1995):

$$\begin{aligned} \mu = \quad & \alpha_0 E_0 \cos \omega_0 t && \text{(Rayleigh scattering)} \\ & + \frac{1}{2}\left(\frac{\partial \alpha}{\partial q}\right)_0 q_0 E_0 \cos (\omega_0 - \omega_R) t && \text{(Stokes scattering)} \\ & + \frac{1}{2}\left(\frac{\partial \alpha}{\partial q}\right)_0 q_0 E_0 \cos (\omega_0 + \omega_R) t && \text{(anti-Stokes scattering).} \end{aligned} \tag{2.7}$$

During the inelastic interactions of the incident beam photons with the optical vibrational modes, the optical phonons, the Raman scattered light has lost (Stokes Raman scattering; $\omega_s=\omega_0-\omega_R$) or has gained energy (anti-Stokes Raman scattering; $\omega_s=\omega_0+\omega_R$) concerning to the Rayleigh scattered light. Consequently the concerned molecule has gained or has lost vibrational energy, respectively. As a result, the Stokes

Raman signal shifts to higher and the anti-Stokes Raman signal to lower wavenumbers, as related to the spectral position of the Rayleigh scattering. After the absorption of a photon of the exciting light source (inelastic collision of a photon with a phonon) the molecule is excited to a short-lived virtual-energy level. During its relaxation back to the first excited vibrational state a photon with lower energy is emitted, because the molecule has gained vibrational energy from the incident light (Figure 4). This process is called Stokes scattering. In the case of anti-Stokes scattering, the molecule is already located in an excited vibrational state and the photon interaction is the same as in Stokes scattering, but it relaxes back to the ground state and a photon with higher energy is emitted, hence the molecule has lost vibrational energy (Figure 4). From quantum-mechanical point of view, the Stokes- and anti-Stokes scattering in solids can be described as phonon creation or annihilation, respectively.

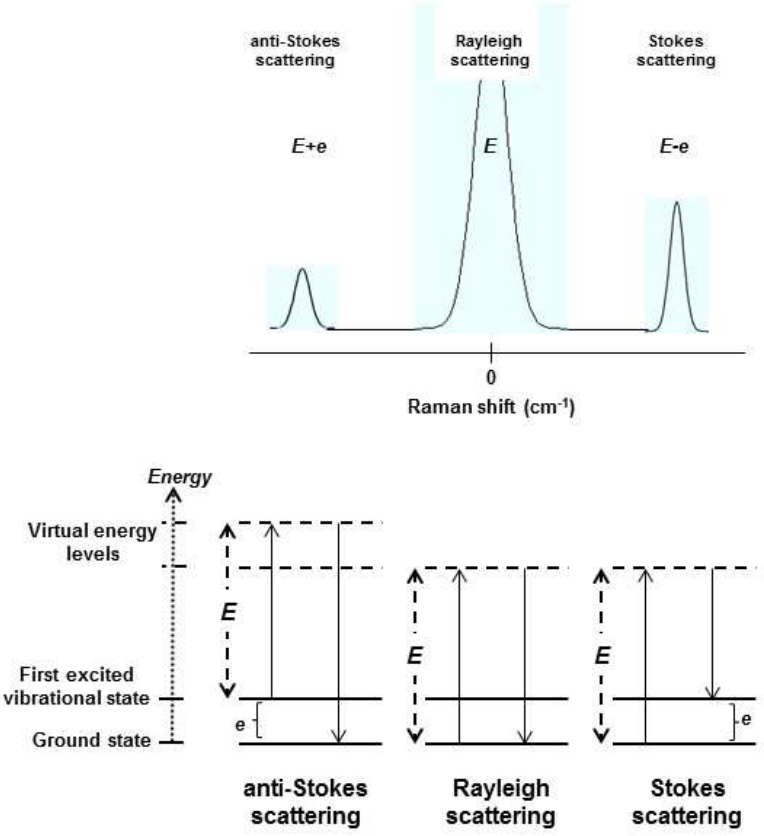

Figure 4: Sketches of anti-Stokes, Rayleigh and Stokes scattering (after Putnis, 1992).

Experimental setups and procedures

In this study the Raman spectroscopic measurements were performed on polished plane-parallel specimens cut in random orientation, using a Horiba Jobin-Yvon T64000 triple monochromator system operating in a subtractive regime and equipped with a liquid N_2-cooled charge-coupled device (CCD) detector and an Olympus BH41 microscope. The spectra were collected in back-scattering geometry without analyzer of the scattering light, using the 514.5-nm line of an Ar^+-ion laser and a long-working distance objective with magnification 50×. The laser spot diameter on the sample surface was approximately 2 μm and the laser power surface density delivered to the sample was 1.5 kW/mm^2, as it was verified that such a power density does not change the sample due to undesired overheating. The reached instrumental spectral resolution was ~ 2 cm^{-1}. Since the Raman laboratory is equipped with an air conditioning system ensuring stability of the room temperature and consequently, thermal stability of the gratings, there are no variations of peak positions related to a plausible subtle thermal expansion of the dispersive element. The Raman spectroscopic system was always calibrated to the position of the Si peak at 520.5 cm^{-1} with a precision of ± 0.35 cm^{-1} and the spectra were measured in the same spectral range, i.e., the gratings were always positioned in the same manner to avoid any inaccuracy in the peak positions related to the slight non-linearity of the signal on the CCD detector. As a result, the achieved experimental precision in determining the peak positions was ~ 0.5 cm^{-1}. For each sample Raman spectra from multiple points (approximately 10 per sample) were collected to check the reproducibility of the spectra, i.e., the homogeneity of the samples with respect to the Raman scattering signals. It was found, that under the experimental conditions used, the spatial variations of the Raman spectra are negligible, if the orientation of the sample is kept. This means that the efficient scattering volume (of order of cubic micrometers) is indeed much larger than the expected nanometric length scale of structural inhomogeneity in metamict titanite. Additionally, measurements with the 488.0 nm line of the Ar^+-ion laser were done to identify possible photoluminescence signals.

Because metamict titanite does not have a specific cleavage plane, Raman spectra from the prepared polished specimens were collected in different orientations at RT, by rotating the sample within the plane perpendicular to the laser beam, in order to check

the influence of the structural anisotropy on the Raman scattering. The repeatability of the spectral features detected at RT was verified by measuring at least two different cuts from each titanite sample. The in situ temperature Raman experiments on the M28696 Cardiff titanite sample were conducted in two different orientations rotated by approximately 90° against each other, which exhibited the strongest difference in the Raman spectra at RT. Raman scattering was recorded using a LINKAM heating/cooling stage. The optimal output laser power under which the sample remained stable during laser irradiation was 600 mW with a filter of optical density 1 and 400 mW with a filter of optical density 2 for temperatures below and above 575 K, respectively.

The in-situ annealing of the M28696 Cardiff titanite sample was done in steps from RT to 825 K inside a LINKAM heating stage (with a heating rate of 10 K min^{-1} and a temperature uncertainty ± 0.1 K) allowing equilibration time of 15 min at each temperature step and 7.5 min for recording the spectrum. The in-situ Raman spectra were measured at temperatures 294, 350, 400, 450, 500, 525, 550, 575, 600, 625, 650, 675, 700, 725, 750, 775, 800, 825 K and finally (after 60 min at 825 K) again at 294 K.

The Raman spectra of the metamict titanite sample E2335 were measured after each annealing step and subsequent cooling to room temperature from two different orientations with respect to the directions of the incident-light propagation and polarization. Spectra of E2312 titanite were also measured in two orientations, but in the same plane, only with different sample rotation angles of 135° and 45°, because at these sample positions the spectra show the most prominent differences. Similarly to the Raman spectra of non-annealed samples, the Raman scattering collected from different spatial areas of E2335 titanite after the subsequent annealing step showed a good reproducibility. Nevertheless, the spectra which were subsequently analyzed were recorded from the same region of the sample, with an uncertainty of ~ 20 micrometers.

Multistep annealing of the metamict titanite samples E2335 and E2312 was carried out in a Thermo Scientific Laboratory Chamber Furnace K114. Ensuring a thermal stability of ± 2 K the heating temperature was controlled by an AHLBORN THERM 2420 temperature-measuring device equipped with a NiCr-Ni thermocouple. E2335 titanite

was annealed in a temperature range of 423 - 1173 K with steps of 50 K and E2312 titanite in temperature steps of 600, 950 and 1220 K. The annealing time at each temperature was 2 h and the heating period before each annealing step was approximately 35 min. The samples were cooled to room temperature and Raman spectra were recorded after each annealing step (at E2312 titanite additionally nanoindentation measurements were performed).

All measured Raman spectra were reduced by the Bose-Einstein occupation factor ($I_{reduced} = I_{measured}/(n(\omega,T) + 1)$, $n(\omega,T) = 1/(e^{\hbar\omega/kT} - 1)$) to eliminate the their temperature dependence and fitted by Lorentzian functions using the software package Origin 8.5, in order to determine the peak positions, full widths at half maximum (FWHM) and integrated intensities. The spectra measured after each annealing step were fitted with the same number of Lorentzians as used for non-annealed metamict titanite and no constrains on the peak parameters when fitting the spectrum profiles were applied.

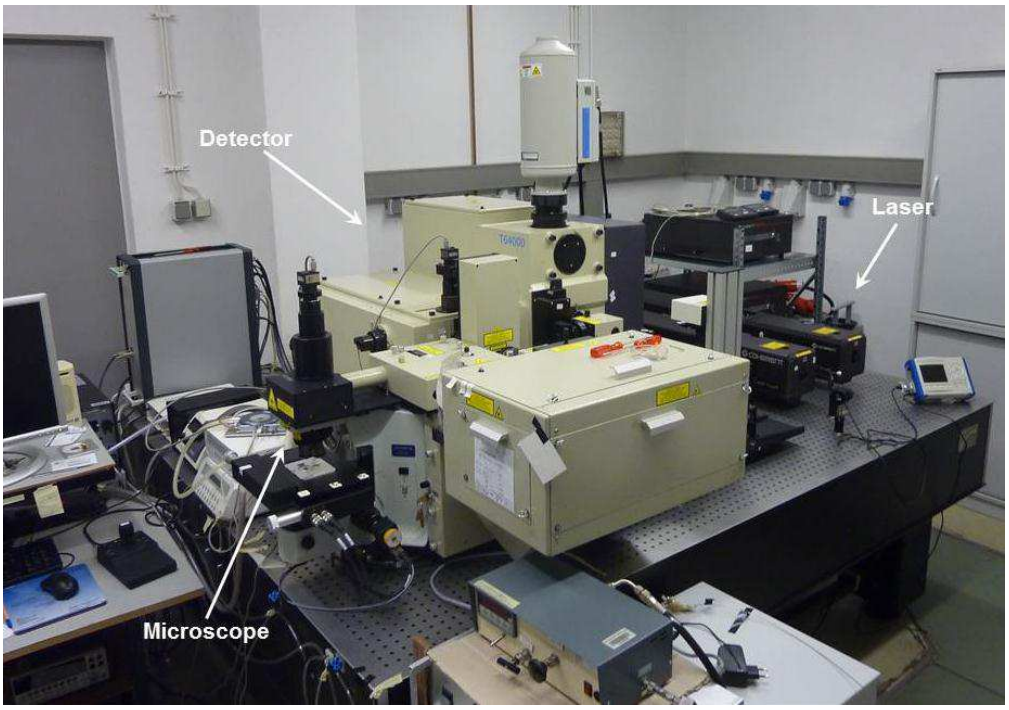

Figure 5: Raman spectrometer: Horiba Jobin-Yvon T64000 triple monochromator system, equipped with a liquid N_2-cooled charge-coupled device (CCD) detector and an Olympus BH41 microscope. The laser is an Ar^+-ion laser.

Fourier transform infrared spectroscopy (FTIR)

Theory

The chapter "Infrared absorption spectroscopy" in the book "Structure and Dynamics" (Dove, 2003) gives a good overview about the infrared spectroscopic method.

During infrared-absorption spectroscopic experiments the sample is irradiated by a polychromatic infrared beam and a transmission spectrum is recorded. The photons of the incident light can propagate through the crystal when the time-varying electric field component of the electromagnetic wave correlates with the atomic vibrations. Hence, the resonance absorption of the energy of the photons of the incident light is only possible, if the frequency of the propagating photon and the phonon modes of the crystal coincide. The requirement (selection rule) for IR activity of an optical mode is a change of the dipole moment of the crystal or molecule due to the offset of the centers of gravity of positively and negatively charged particles. (Dove, 2003)

As referred by Jaggi and Vij (2006) the advantage of the Fourier transform spectroscopy is the possibility of analyzing various frequency compounds simultaneously in a single operation. In FTIR spectroscopy the sample is irradiated by a single infrared pulse with a particular range of frequencies. The resonance frequencies resulting from the interaction with the sample will be dominant in the detected signal. Applying Fourier transformation on the resonance signal leads to the possibility to calculate the frequency response. (Jaggi and Vij, 2006)

Experimental setups and procedures

As a reference, the IR spectrum of a pure synthetic titanite sample was measured at RT using a Bruker IFS 113v Fourier-transform spectrometer with instrumental resolution of 2 cm^{-1}. The conventional pellet technique was used for IR measurements and the matrix material for the 185–625 cm^{-1} region was CsI, whereas KBr was used for the 500–1200 cm^{-1} range. The powdered sample and dried CsI or KBr powder (with sample to matrix ratio of 1 : 300 by weight) were mixed in a Spex mill (without grinding ball) for 20 min. Approximately 300 mg of the sample/CsI mixture and 200 mg of the sample/KBr

powder were pressed under vacuum at a compression of 10 tons cm^{-2} to form a reference pellet of 13 mm diameter. Overall 512 scans were accumulated for the spectrum recorded under vacuum.

For FTIR measurements of metamict allanite R1 also the conventional pellet technique was used. The matrix material was KBr (1 mg powdered allanite R1 sample and 200 mg KBr powder). The FTIR spectra were measured with a BRUKER EQUINOX IFS 55 spectrometer equipped with a DLATGS-detector. Between 128 and 320 scans were accumulated for each allanite spectrum with a spectral resolution of 0.5 cm^{-1} over the range between 400 cm^{-1} and 4000 cm^{-1}. The spectra were measured at room temperature and analyzed with the Bruker Opus/2 software. The powdered allanite R1 samples were annealed for 20 min at 723, 823 and 923 K and afterwards measured at RT as KBr pellets.

Group-theory analysis of pure titanite

The first-order infrared absorption and Raman scattering spectra of pure titanite can be described by the corresponding optically active irreducible representations at the center of the Brillouin zone (Γ-point) (Kroumova et al., 2003). In Table 2 the Γ-point phonon modes associated with the occupied Wyckoff positions in the two titanite phases C2/c and $P2_1/c$ are given. 31 Raman signals were experimentally resolved in the spectra of synthetic single-crystal titanite (Figure 8), which is less than the number of expected Raman-active modes for the room temperature phase $P2_1/c$ ($24A_g + 24B_g = 48$ in total), but more than the Raman-active modes allowed in C2/c ($9A_g + 12B_g = 21$ in total) (Salje et al., 1993). The smaller number of experimentally observed Raman peaks than the number predicted by group theory is most probably due to the weak intensities of some modes and/or overlapping of peaks generated from modes of different symmetry but involving the same type of atomic vibrations in terms of stretching, bending etc.

Raman spectra collected with a dispersive spectrometer and a linearly polarized laser are always partially polarized, even when no analyzer was used on the scattered light, due to the inherent transmission efficiency of the gratings. Thus some discussion about the orientation dependence of the Raman scattering intensities for pure single-crystal

titanite is required. For the used experimental set-up, the strongest contribution to the Raman spectra comes from the scattered light which has a polarization $\mathbf{E}_s$ parallel to the polarization of the incident light $\mathbf{E}_i$. The both matrix representations of the Raman polarizability tensors for A_g and B_g modes in a monoclinic system with unique axis b are

$$A_g: \begin{pmatrix} a & 0 & d \\ 0 & b & 0 \\ d & 0 & c \end{pmatrix} \text{ and } B_g: \begin{pmatrix} 0 & e & 0 \\ e & 0 & f \\ 0 & f & 0 \end{pmatrix}.$$

Table 2: Site-symmetry analysis of the allowed Brillouin-zone-center phonon modes in pure titanite; R stands for Raman-active, IR for infrared-active.

P_12/c	**C2/c**
Ca (4e): $3A_g + 3A_u + 3B_g + 3B_u$	**Ca (4e): $A_g + A_u + 2B_g + 2B_u$**
Ti (4e): $3A_g + 3A_u + 3B_g + 3B_u$	**Ti (4b): $3A_u + 3B_u$**
Si (4e): $3A_g + 3A_u + 3B_g + 3B_u$	**Si (4e): $A_g + A_u + 2B_g + 2B_u$**
O1 (4e): $3A_g + 3A_u + 3B_g + 3B_u$	**O1 (4e): $A_g + A_u + 2B_g + 2B_u$**
O2 (4e): $3A_g + 3A_u + 3B_g + 3B_u$	**O2 (8f): $3A_g + 3A_u + 3B_g + 3B_u$**
O3 (4e): $3A_g + 3A_u + 3B_g + 3B_u$	**O3 (8f): $3A_g + 3A_u + 3B_g + 3B_u$**
O4 (4e): $3A_g + 3A_u + 3B_g + 3B_u$	
O5 (4e): $3A_g + 3A_u + 3B_g + 3B_u$	
$\Gamma_{optic} = 24A_g$ (R) + $23A_u$ (IR) + $24B_g$ (R) + $22B_u$ (IR)	**$\Gamma_{optic} = 9A_g$ (R) + $11A_u$ (IR) + $12B_g$ (R) + $13B_u$ (IR)**
$\Gamma_{acoustic} = A_u + 2B_u$	**$\Gamma_{acoustic} = A_u + 2B_u$**

X-ray diffraction (XRD)

Theory

X-rays are suitable for investigating the structure of crystals because their wavelength and the interatomic distances from crystals are of the same order of magnitude (in the order of 10^{-10} m). Hence X-rays can be diffracted by the periodically ordered atomic array, more precisely due to their interaction with the electron shells of the atoms. The frequency of electromagnetic X-ray waves is of about 10^{18} Hz. Their oscillating electric field induces the electron clouds of the atoms in the target matter to oscillate themselves and hence to emit X-rays. Diffraction is referred by Dove (2003) as a process of coherent elastic scattering from the long-range order in periodically ordered structures. As described by Giacovazzo et al. (2002) the diffraction process could be seen as reflections of the incident monochromatic X-ray beams at a family of lattice planes under a certain angle θ (glancing angle). The planes are parallel to each other with a consistent spacing d. Constructive interference of the diffracted beams will occur if their path difference Γ is an integral multiple n of the wavelength λ (Γ=nλ).

$$\sin\theta = \frac{\Gamma}{2d} \tag{2.8}$$

leading to the Bragg equation which describes the condition for constructive interference:

$$n\lambda = 2d\sin\theta \tag{2.9}$$

Due to the fact that X-rays are scattered by the electrons in a sample, they supply information on the electron-density distribution in the crystal structure. The scattering power of each atom depends on the number of electrons. Hence, heavy atoms are stronger scatterer than light atoms and also neutral and charged atoms of the same species will scatter differently. X-ray scattering power of the atoms (atomic scattering factor) decreases with increasing scattering angle ($sin\ \theta/\lambda$) because of the shapes of the

orbitals. At higher *sin θ/λ* values especially the electrons from inner shells will contribute to the scattering, hence at smaller values the scattering is mostly influenced by valence electrons. The X-ray atomic scattering factor could be expressed by

$$f(\boldsymbol{Q}) = \int \rho_{el}(\boldsymbol{r}) \exp(i\boldsymbol{Q} * \boldsymbol{r}) d\boldsymbol{r} \qquad (2.10)$$

the electron density is given by $\rho_{el}(\boldsymbol{r})$, **Q** is the scattering vector and **r** is a vector separating two particles. (Dove, 2003)

Synchrotron radiation

Synchrotron X-ray radiation is produced when charged particles, e.g. electrons or positrons, are accelerated by an accelerating field to nearly the speed of light in a circular orbit under a very high vacuum. Strong magnets guide the charged particles on the circular path. By passing the curvatures of the synchrotron accelerating ring the electrons or positrons are decelerated and hence they emit X-ray radiation. In contrast to a laboratory X-ray source, were the experimentally used X-rays results from induced electron transitions in the atoms of a target material hit by accelerated electrons, synchrotron radiation is emitted as a continuous distribution of X-ray wavelengths. By using a monochromator, the requested wavelength could be selected. Also the intensity of the synchrotron radiation is much higher and the divergence of the polarized emitted beam much smaller. (Giacovazzo et al., 2002; Dove, 2003)

Experimental setups and procedures

Synchrotron single-crystal X-ray diffraction studies of the metamict samples M28696 Cardiff titanite, E2312 titanite and R1 allanite were carried out at beamline F1 at HASYLAB/DESY using a Kappa-diffractometer equipped with a CCD detector (MarCCD165). With a wavelength of 0.5600 Å and a sample-to-detector distance of 80 mm for the titanite and 60 mm for the allanite samples. Progressive annealing

experiments were performed at M28696 titanite (600, 850 and 950 K) and R1 allanite (798, 898, 948, 998, 1023 and 1073 K) with a heating period of 15 min and at E2312 titanite (600, 950 and 1220 K) with a heating period of 2 h at each temperature step. In addition, isothermal annealing experiments with a wavelength of 0.5 Å and heating at 823 K for 2.6 h were carried out at allanite R1. The annealing was done with a N_2 gas-stream heating device. The heating device was calibrated using a NiCr–Ni thermocouple previous to the experiment, giving a thermal stability of ±3K. Scans with a step width of 0.3° in different phi-positions were done for each annealing step and an exposure time of 15 s per frame.

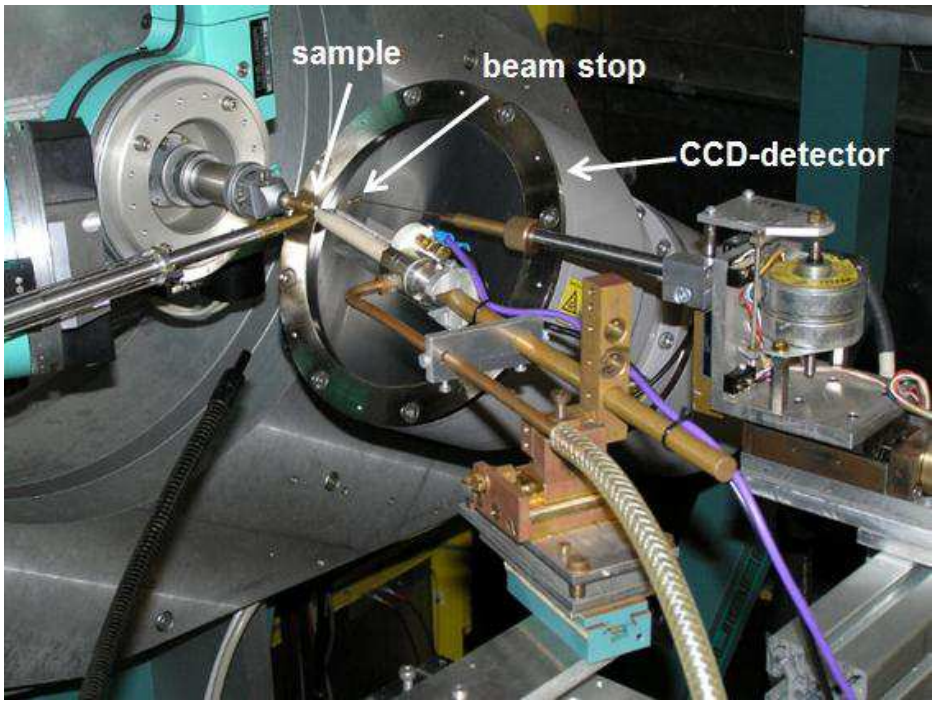

Figure 6: Kappa-diffractometer of F1 beamline at HASYLAB/DESY.

The integrated intensities were obtained by defining a box with xy-center and xy-half-width around the Bragg reflection, large enough to cover the whole reflection and the surrounding background region. After calculating the average intensity on the outer rim,

every pixel (outer rim) with intensity three times less than the standard deviation from the average intensity value ($I < 3\sigma(I)$) was taken as background signal, giving the new average background value. This new background was then subtracted from the total intensity inside the integration box. This process was done frame by frame leading to the final integrated intensity data.

Rocking curve fits of the measured integrated intensities of E2312 titanite were performed with the implemented Voigt function, a convolution of a Gaussian and a Lorentzian peak shape, of the IGOR Pro software (WaveMetrics, Version: 6.2.2.2). The calculated shape factor is a shape parameter that adjusts the relative contributions of the Gaussian and the Lorentzian part of the Voigt profile (Armstrong, 1967; Schreier, 1992). A shape factor value of zero indicates a pure Gaussian shape, a value of 1 means a 50/50 distribution of Gaussian and Lorentzian shape and infinity indicates a pure Lorentzian shape. The Voigt function is of the form (Armstrong, 1967; Humlicek, 1982)

$$K(x,y) = \frac{y}{\pi}\int_{-\infty}^{+\infty} \frac{\exp(-t^2)}{y^2+(x-t)^2}\,dt \qquad (2.11)$$

with

$$y = \frac{\alpha_L}{\alpha_D}(ln2)^{1/2} \qquad (2.12)$$

where y is the ratio of Lorentz to Gauss (or Doppler) widths, α_L is the Lorentz half-width and α_D the Gauss (or Doppler) half-width. (Armstrong, 1967)

The crystallographic orientation of the titanite samples and their face indices were obtained using a Nonius KappaCCD single crystal diffractometer with Mo Kα-radiation. Indexing of diffraction spots was performed using the program Denzo (Otwinowski and Minor, 1997) and the obtained unit cell setting of titanite corresponds to that described by Hawthorne et al. (1991).

X-ray powder diffraction

In contrast to a single crystal sample, as in single crystal X-ray diffraction, in X-ray powder diffraction a fine powdered crystalline sample is used for diffraction experiments. Monochromatic X-rays are diffracted at the small crystallites, which are uniformly distributed in orientation in the powder. Because of their statistically distribution, there will be always a quantity of crystallites orientated in the right position to meet the Bragg-conditions for a specific family of lattice planes. (Dove, 2003)

The powder XRD patterns of metamict titanite were recorded using a Philips XPert powder diffractometer with Bragg Bretano geometry and Cu-Kα radiation. The progressive annealing experiments with 1800 s at each temperature step were performed on the diffractometer using an Anton Paar platinum strip heater with a temperature resolution of ±1 K.

Transmission electron microscopy (TEM)

Theory

During transmission electron microscopy measurements electrons are accelerated onto the sample focused by electromagnetic lenses to illuminate a small area. The incident electron beam will be diffracted by the periodically ordered atoms in the crystal and the diffracted beams could be recombined to form an image, which shows the density of the scattering material in the sample as a two-dimensional projection (Putnis, 1992).

Experimental setup and procedure

The intrinsic nanometer-scale structural inhomogeneity of the studied metamict titanite E2335 was probed by TEM. Titanite pieces of random orientation and size between 0.1 and 1 μm were dispersed in ethanol and mounted on a carbon coated copper grid using an ultrasonic sprayer. The TEM experiments were performed with an FEI TECNAI F30 microscope equipped with a Super-twin lens, operating at 300 kV using a scanning

TEM unit with a HAADF detector and a 1x1K slow scan CCD camera. Measurements were conducted using a double tilt halter at room temperature.

Nanoindentation

Theory, experimental setup and procedure

Nanoindentation experiments were performed on metamict titanite E2312, nonmetamict Rauris titanite and titanite glass with an Agilant Nano Indenter G200, equipped with a standard diamond XP indentation head (XP_TB15689 tip) with Berkovich geometry (Pharr, 1998). The Continuous Stiffness Measurement (CSM) technique was used for the mechanical tests. During CSM the sample stiffness was measured continuously in the course of the loading process of the indenter by imposing a small dynamic oscillation on the force or displacement signal and measuring the amplitude and phase of the corresponding displacement or force signal with a frequency-specific amplifier (Oliver and Pharr, 2004). Five to seven indents were distributed all over the sample surface with an indentation depth limit of 2000 nm. The average hardness (H) and elastic modulus (E) of the titanite samples were calculated from the load-displacement data (Oliver and Pharr, 2004). During the indentation process elastic and plastic deformation occurs in the sample and in the course of the unloading process, only the elastic part of deformation recovers. The hardness is determined by

$$H = \frac{P_{max}}{A} \tag{2.13}$$

where P_{max} is the maximum load and A the contact area (Oliver and Pharr, 2004).
The elastic modulus E of the sample is calculated by

$$E = \frac{1-\nu^2}{\left(\frac{1}{E_{eff}} - \frac{1-\nu_i^2}{E_i}\right)} \tag{2.14}$$

where E_i and ν_i are the Young´s modulus and Poisson´s ratio of the indenter (for the diamond indenter E_i=1141 GPa and ν_i=0.07) and ν is the Poisson´s ratio of the sample (Oliver and Pharr, 2004). The effective elastic modulus E_{eff} is defined by

$$E_{eff} = \frac{1}{\beta}\frac{\sqrt{\pi}}{2}\frac{S}{\sqrt{A}} \tag{2.15}$$

where S is the stiffness and β a constant depending on the indenter geometry (for Berkovich geometry β = 1.034) (Pharr, 1998). The E_{eff} considers that elastic displacement takes place in the sample and in the indenter (Oliver and Pharr, 2004).

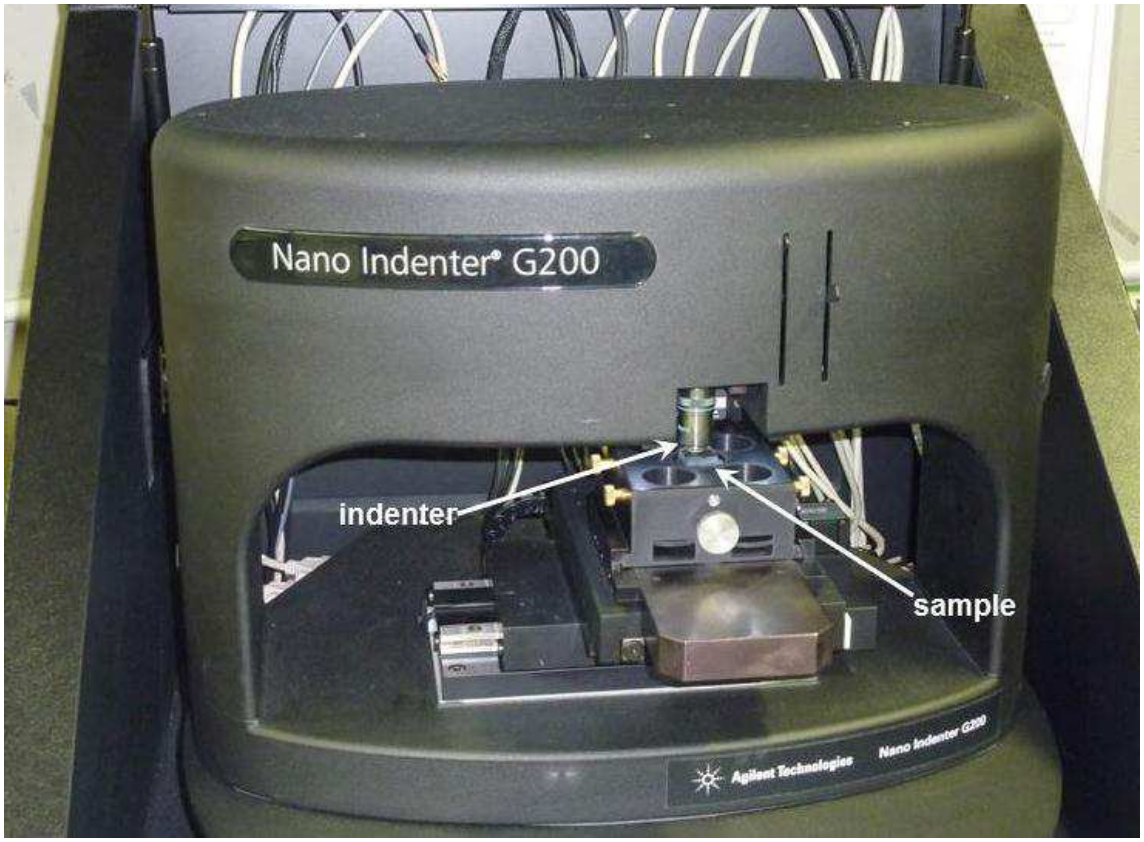

Figure 7: Agilant Nano Indenter G200, equipped with a standard diamond XP indentation head (XP_TB15689 tip) which had Berkovich geometry.

Electron microprobe analysis and X-ray fluorescence analysis

Theory

As described by Rollinson (1993) the principles of electron microprobe analysis (EMPA) and X-ray fluorescence (XRF) analysis are very similar. The main difference is the nature of the incident beam that excites the deep electron levels in the sample. In the case of EMPA, the excitation is caused by an electron beam and in the case of XRF by an X-ray beam. This leads to the occurrence of secondary X-rays in the sample which have element specific wavelengths. To obtain the specific element concentration, the measured intensities are compared with the intensities of a standard with a known concentration of the element.

Experimental setup and procedure

The chemical composition of allanite sample R1 (Table 3) was determined by electron microprobe analysis using a CAMECA Camebax microbeam SEM system, averaging over 40 analysis points with an acceleration voltage of 20 keV and a probe current of 10.5 nA. The electron beam diameter was set at 30 μm because the sample had a large percentage of hydroxides which produce significant volatilization. The on-peak counting time for Th, U and Nd amounted to 60 s, with 30 s counting time for the background. All further elements were measured with a 20 s on-peak counting time and 10 s for the background. The following standards were used: MgO (Mg-Kα), Al_2O_3 (Al-Kα), andradite (Si-Kα, Ca-Kα, Fe-Kα), $MnTiO_3$ (Ti-Kα), YAG (Y-Lα), monazite (La-Lα, Ce-Lα, Nd-Lβ, Th-Mα) and UO_2 (U-Mβ). Data reduction was done with the PAP routine (Pouchou and Pichoir, 1984). The X-ray fluorescence analysis was performed with a Philips PW 1408 spectrometer. A total of 0.3 g of the powdered metamict allanite sample was mixed with $Li_2B_4O_7$ flux in a 1:6 ratio to make a fused pellet.

3 Results

Metamict titanite

Raman spectroscopy of unannealed titanites with different degree of metamictization

The RT Raman spectra shown in Figure 8 are recorded from several titanite samples, including titanite glass, and confirm the different degree of metamictization via the profiles and positions of the excitations. The most damaged metamict titanite sample M28696 stems from Cardiff, while the samples M28173 and M28658 show a lower degree of destruction, respectively. This is indicated by the gradual broadening of the existing Raman peaks and the development of new peaks in the sequence synthetic single crystal titanite – titanite sample M28658 – titanite sample M28173 – titanite sample M28696 (Cardiff) (Figure 8). The Raman scattering of the metamict titanite samples collected in orientation 1 more or less resembles the spectrum of well-crystalline titanite but the peaks become broader with increasing damage index and the strongest Raman signal near 605 cm^{-1} shifts to lower wave numbers. By contrast, measured in orientation 2 the spectra of M28173 and Cardiff (damage index 8 and 10, respectively) considerably differ from the spectrum of pure synthetic titanite. The most prominent difference is the appearance of a very broad peak near 630 and 660 cm^{-1} for M28173 and Cardiff, respectively. It attains but does not reach the wide band near 770 cm^{-1} in titanite glass.

The spectra of all radiation-damaged titanite samples (nearly undamaged M28658, E2335, M28173 and M28696) could be successfully fitted with the same number of Lorentzians, which however differed from the number of fitting functions used for synthetic titanite (Figure 17). The reason is the appearance of new peaks in the range 600 – 900 cm^{-1} due to the symmetry breakdown and development of non-crystalline regions (Figure 8). Also some of the weak peaks observed in the spectrum of crystalline titanite could not be resolved in the spectra of metamict samples and hence, the corresponding Lorentzians were skipped while fitting the spectra.

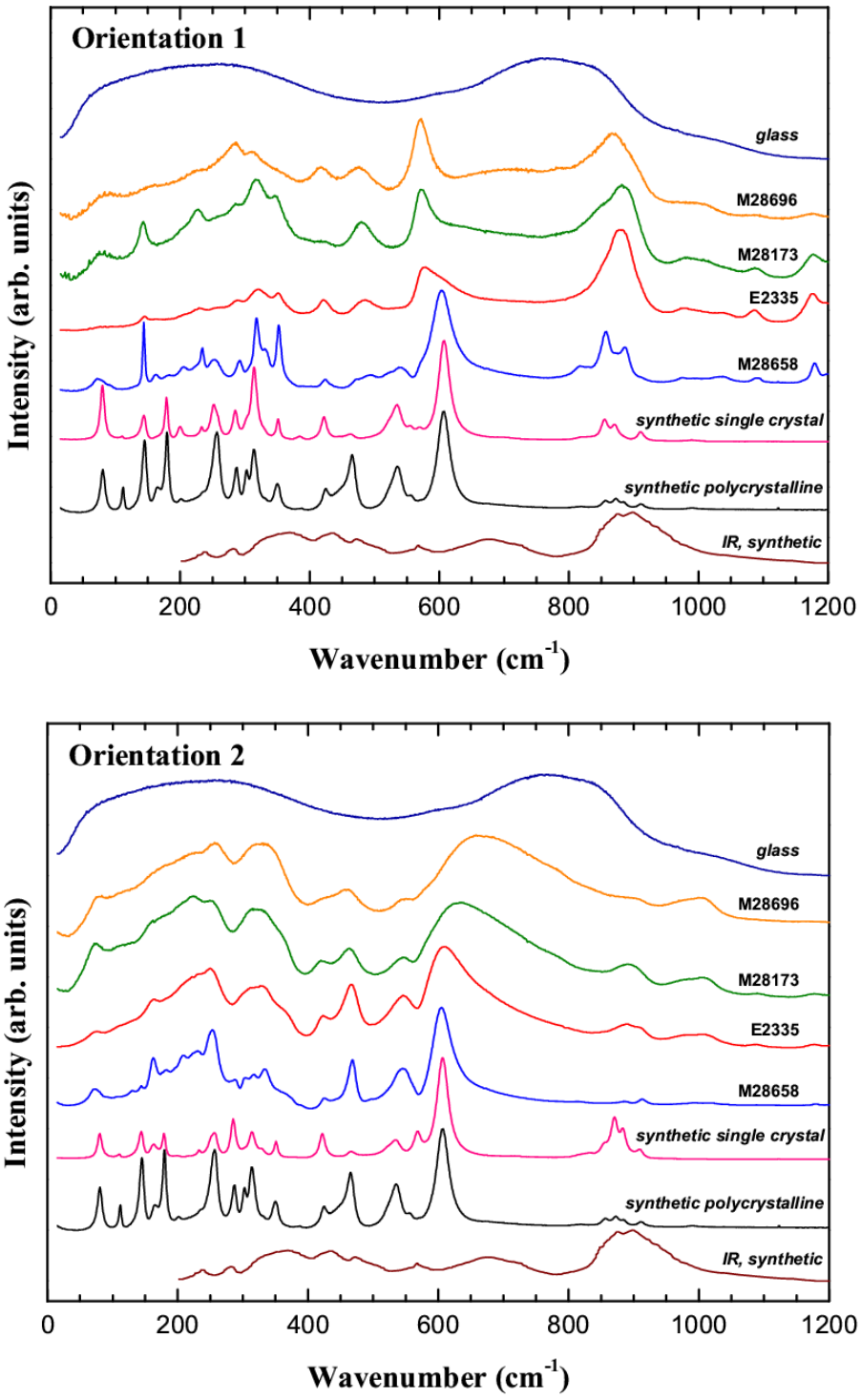

Figure 8: RT Raman spectra of metamict titanite samples with different degree of metamictization (Table 1) (M28696 Cardiff, M28173, E2335 and M28658) measured in two different orientations, designated as orientation 1 and orientation 2, for which the samples show most prominent spectral difference. The signals in the spectra near 1180, 1090 and 1045 cm^{-1} are photoluminescence peaks. For sample E2335 the band near 880 cm^{-1} measured in orientation 1 results from overlapping Raman and photoluminescence signals. For comparison, the Raman spectra of titanite glass, synthetic polycrystalline titanite and synthetic single crystal titanite, as well as the powder IR absorption spectrum of synthetic titanite are included in both plots. The spectra are vertically offset.

Metamict titanite sample M28696 (Cardiff)

Raman spectroscopy

The Raman spectra collected from the Cardiff titanite sample in orientation 1 are shown in Figure 9. All peaks shift to lower wavenumbers with increasing temperature and the same trend is observed for the spectra measured at elevated temperatures in orientation 2 (Figure 9, 10). After annealing to 825 K shifts of the peaks at 284.8 ± 0.6 cm^{-1} (shift to 288.7 ± 0.4 cm^{-1}), at 419.8 ± 0.2 cm^{-1} (shift to 422.8 ± 0.1 cm^{-1}) and at 873.6 ± 0.1 cm^{-1} (878.0 ± 0.1 cm^{-1}) were observed in orientation 1 (Figure 9, 10). The Raman peaks near 873 and 419 cm^{-1} correspond to Si–O stretching and O–Si–O bending modes in orthosilicates (Dowty, 1987), while the peak near 284 cm^{-1} should be related with external SiO_4 modes. The remaining peaks observed in orientation 1 as well as all peaks observed in orientation 2 stay unchanged after annealing.

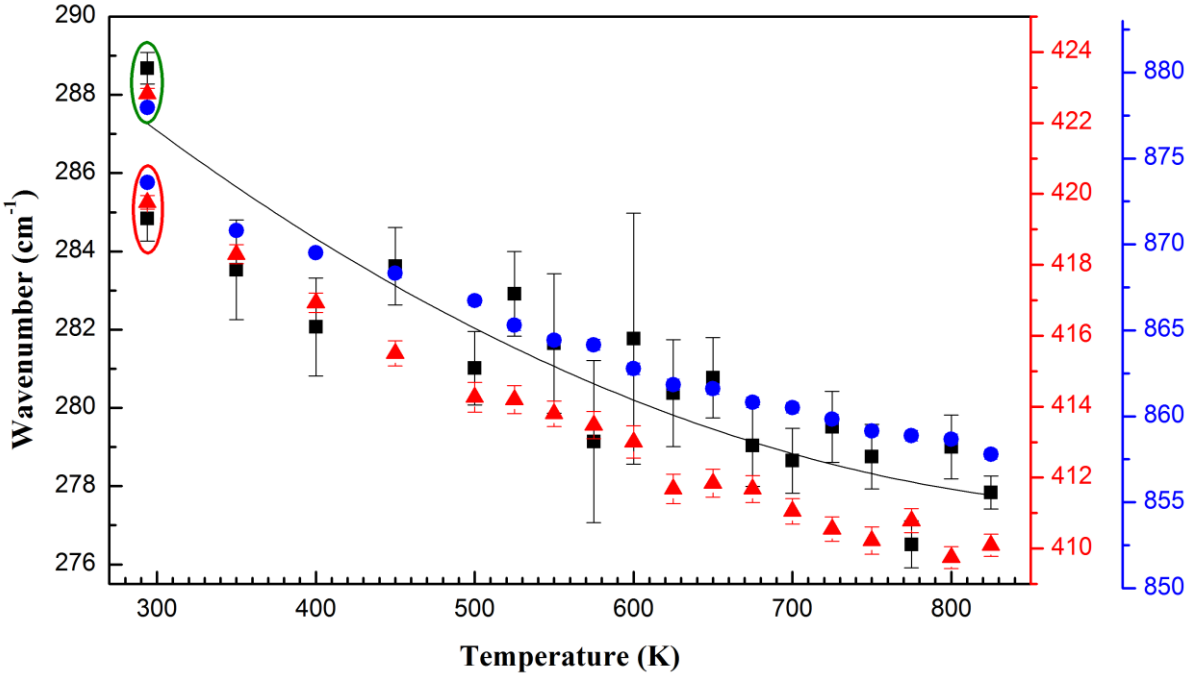

Figure 9: Decreasing wavenumbers of the Raman peaks of M28696 Cardiff titanite near 285 cm^{-1} (black), 420 cm^{-1} (red) and 874 cm^{-1} (blue) during thermal annealing (orientation 1). Shifts to higher wavenumbers measured at RT after the annealing process are marked with a green circle, the red circle marks the peak positions before annealing.

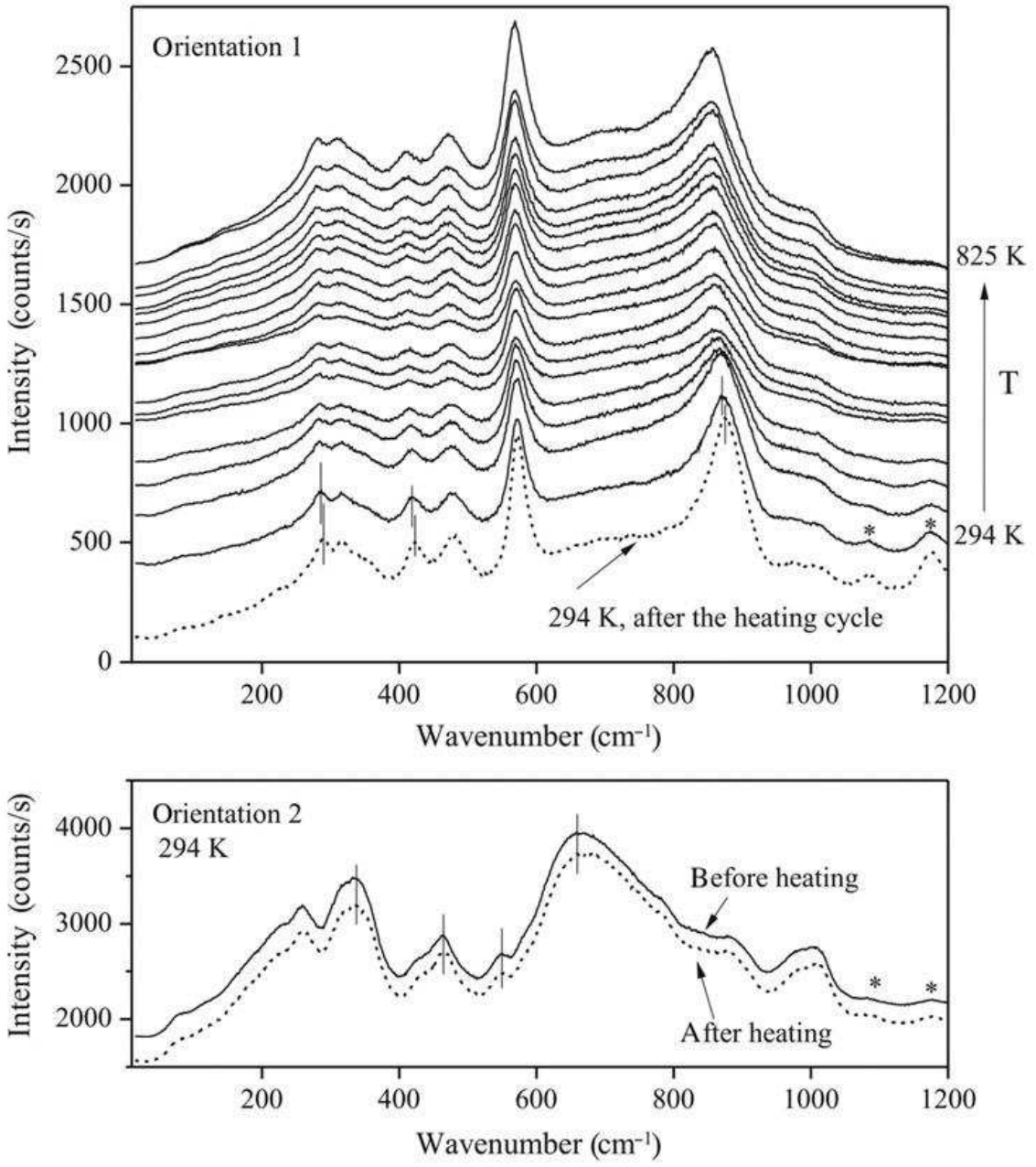

Figure 10: Raman spectra of metamict M28696 Cardiff titanite measured in orientation 1 on heating from 294 to 825 K, as well as at 294 K after annealing (dashed line). The vertical lines in the upper plot mark the Raman peak positions which shift to higher wave numbers after annealing. The bottom plot presents the RT spectra measured in orientation 2 before (solid line) and after annealing (dashed peak), the peak shifts were resolved for this orientation. The asterisks mark the Raman peaks arising from photoluminescence. The spectra are vertically offset.

Synchrotron single-crystal XRD

Figure 11 shows the integrated intensity of the Bragg reflection $(\bar{1}3\bar{1})$ versus the rotation angle φ measured for the M28696 Cardiff titanite sample at RT before and after annealing at three representative temperatures (600, 850 and 950 K). The strong scatter of the rocking curve data points measured before annealing is related to the high structural inhomogeneity and indicates coexistence of spatial regions with different degree of crystallinity. The increasing Bragg intensity correlated with increasing annealing temperature is visible.

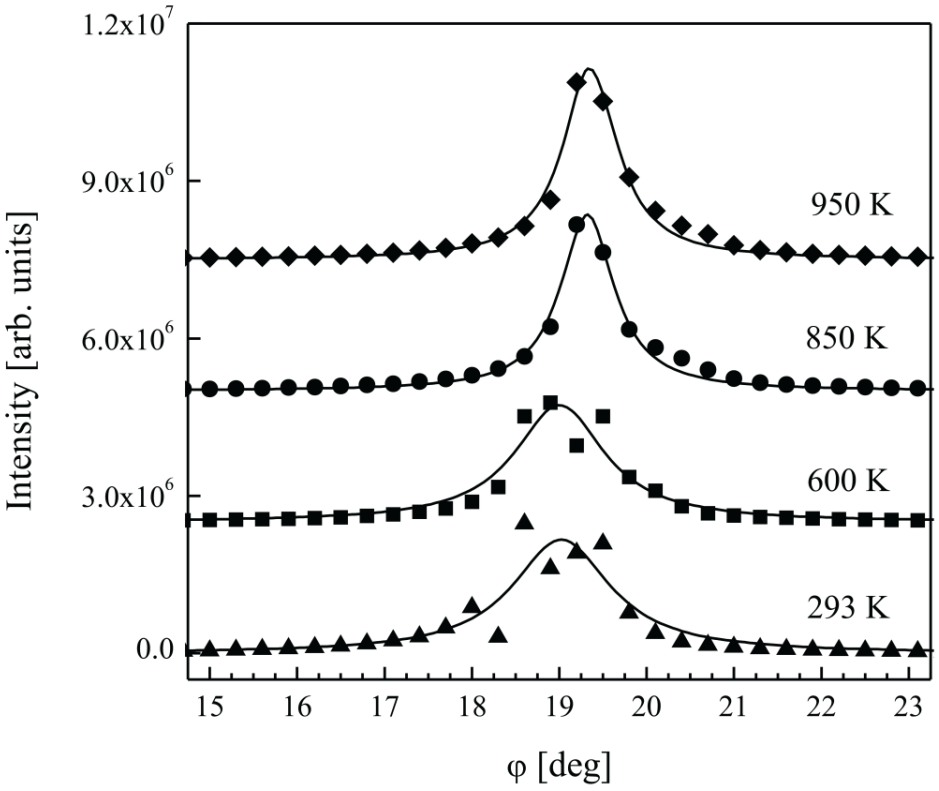

Figure 11: Integrated intensities around the $(\bar{1}3\bar{1})$ Bragg reflection in metamict titanite M28696 from Cardiff measured at RT before (293 K) and after annealing for 15 min at different temperatures (600, 850 and 950 K). The lines represent Lorentzian fits to the experimental data points. The large deviations of the experimental points measured before annealing (293 K) and after annealing at 600K are related to the coexistence of spatial regions with different degrees of crystallinity in the same crystal.

The rocking-curve data of the $(\bar{1}3\bar{1})$ Bragg reflection was fitted using Lorentzian profiles which show a decreasing FWHM with increasing annealing temperature (Figure 12).

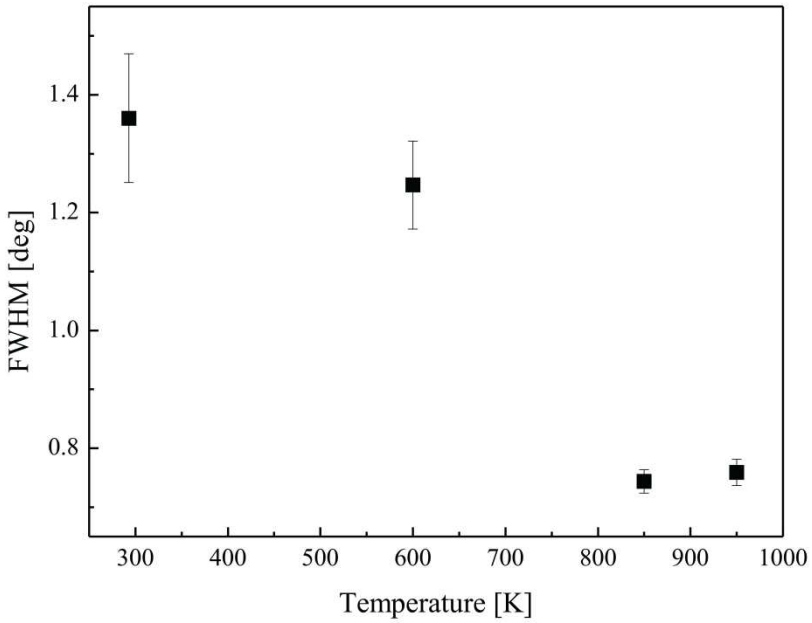

Figure 12: Development of FWHM of the $(\bar{1}3\bar{1})$ Bragg reflection in metamict M28696 Cardiff titanite as a function of annealing temperature determined from the Lorentzian fits to the integrated intensities as a function of the rotation angle φ. The error bars correspond to uncertainties in FWHM stemming from nonlinear curve fitting.

Metamict titanite sample E2335

Transmission electron microscopy

A large number of submicron particles of E2335 metamict titanite were examined by scanning TEM and showed monocrystalline diffraction patterns (Figure 13a). The TEM images were used for more detailed examination of randomly chosen crystals of an E2335 specimen. The crystals, as shown in Figure 13, exhibit structural inhomogeneities and variations in the thickness. The HR-TEM images obtained from different peripheral parts of this crystal provided identical fast Fourier transform (FFT) patterns (inset in Figure 13b).

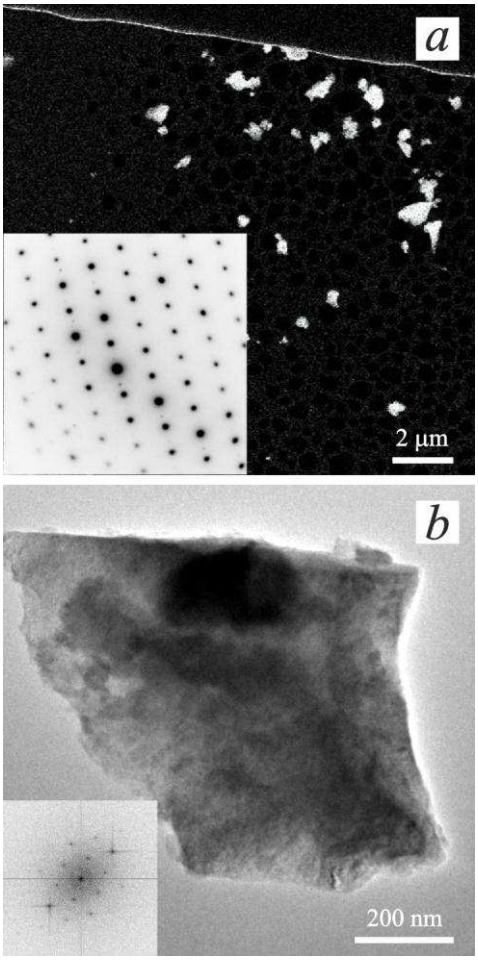

Figure 13: (a) Typical scanning TEM image. (Inset in 13a) Electron diffraction pattern of E2335 titanite. (b) TEM image of a single, randomly chosen E2335 particle. (Inset in 13b) Calculated FFT pattern for the peripheral part, which corresponds to the crystallographic $[1\bar{1}1]$ zone.

Coexisting nanoregions with crystalline fringes and with lack of periodicity are visible in the HR-TEM images (Figure 14a). Periodic faults inside the crystalline nanoregions are also revealed under higher magnification (Figure 14b).

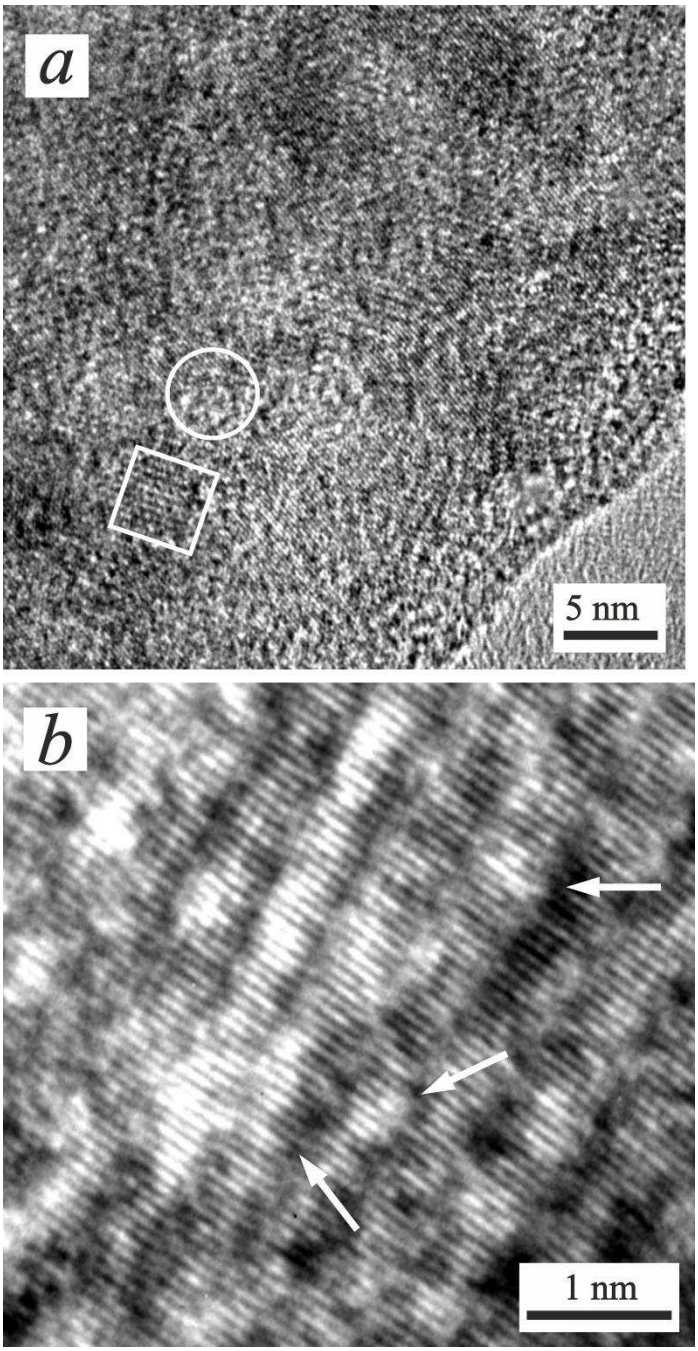

Figure 14: HR-TEM images obtained from different parts of the titanite crystal shown in Figure 13b. The white rectangle and circle in Figure 14a mark crystalline and amorphous nanoregions, respectively. White arrows in 14b point to edge dislocations.

Further TEM images obtained from various parts of the E2335 crystal also show the partially radiation damaged structure. Crystalline and amorphous regions are detectable next to each other (Figure 15).

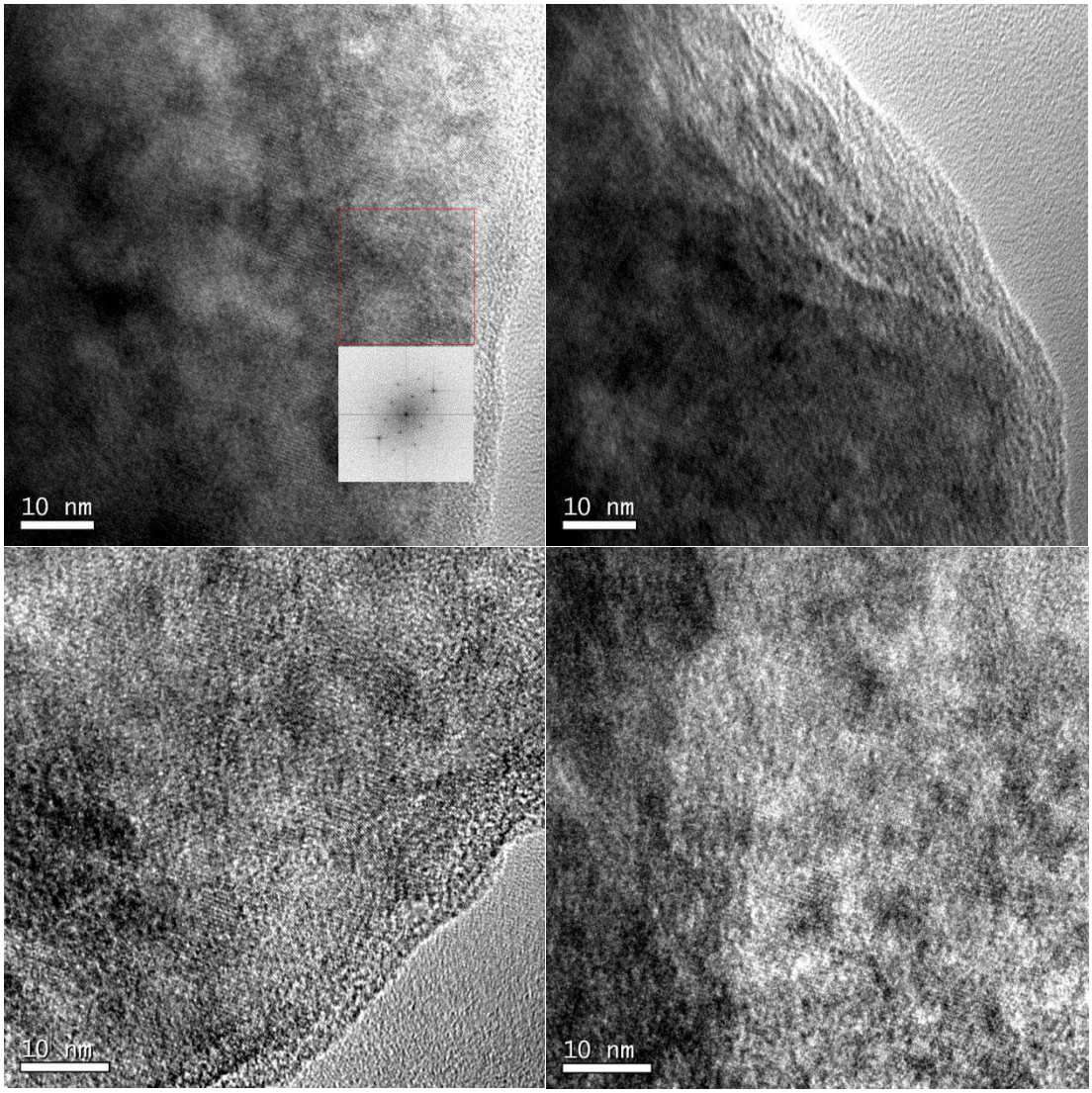

Figure 15: TEM images obtained from various parts of the metamict E2335 titanite crystal, shown in Figure 13b. (Inset in 15) Calculated FFT pattern for the peripheral part, which corresponds to the crystallographic $[1\bar{1}1]$ zone.

Raman spectroscopy

The orientation of the studied E2335 metamict titanite specimen with respect to the direction of the propagation $\mathbf{k}_i$ and the polarization vector $\mathbf{E}_i$ of the incident light is displayed in Figure 16. In Orientation 1 $\mathbf{k}_i$ is perpendicular to the crystallographic plane $(\bar{2}\bar{2}3)$ (Miller indices refer to $C2/c$), while $\mathbf{E}_i$ is perpendicular to $(\bar{2}41)$. In orientation 2 on the other hand the incident light propagates in the direction perpendicular to the crystallographic plane $(\bar{2}41)$, while the polarization $\mathbf{E}_i$ is perpendicular to $(\bar{2}\bar{2}3)$. In both scattering geometries the in-plane rotation of the sample has little effect to the spectrum profile.

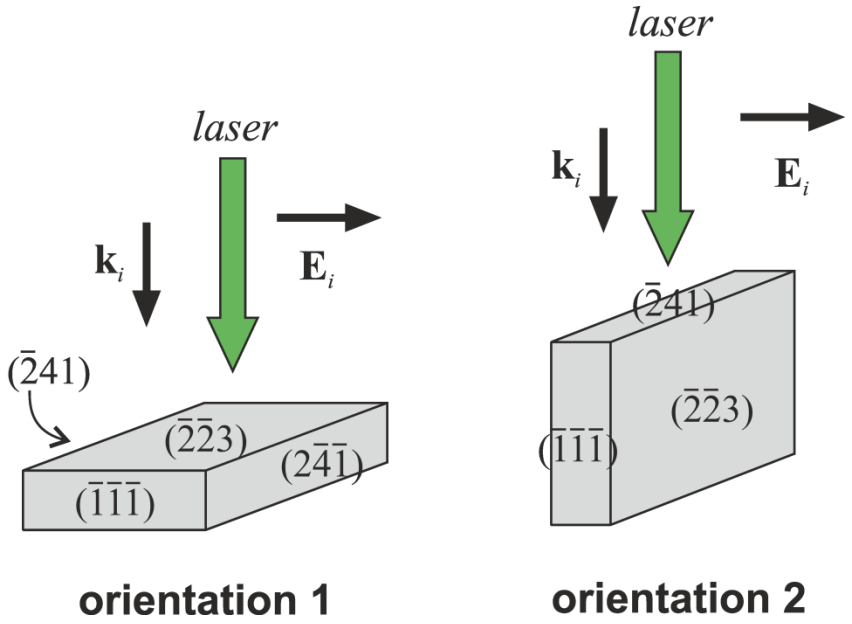

Figure 16: Sketch of the titanite crystal orientation during the Raman scattering measurements; $\mathbf{k}_i$ denotes the direction of the propagation of the incident laser light, whereas $\mathbf{E}_i$ is the polarization of the laser. The Miller indices are given for $C2/c$. No analyzer was used in the Raman experiments. In-plane rotation of the titanite sample had little effect on the spectrum profile, indicating that the difference in the Raman scattering collected in orientation 1 and orientation 2 is related to quasi-planar structural species in the plane parallel to $\mathbf{E}_i$, rather than to quasi-linear structural species along the direction of $\mathbf{E}_i$.

The Raman spectra collected from E2335 compared with the spectra of other titanite samples with different degrees of metamictization (increasing degree of crystallinity from top to bottom) are shown in Figure 8. The two sample orientations are designated

as orientation 1 and 2, following the nomenclature of the Raman spectra described in the results of the Raman spectroscopic measurements of M28696 titanite (Figure 8). The two sample orientations are approximately perpendicular to each other and the Raman spectrum of metamict titanite with a damage index 10 collected in orientation 1 corresponds most closely to the spectrum of well-crystalline titanite, whereas the Raman spectrum collected in orientation 2 substantially differs from that of well-crystalline titanite.

To verify the possibility of separately studying the evolution of defects inside crystalline nanoregions and the amorphous-to-crystalline nanoscale transitions, the Raman spectra of E2335 titanite were analyzed subjected to multi-step annealing in the range of 423 to 1173 K (Figure 17). The Raman spectra from annealed E2335 were effectively fitted using the same number of Lorentzian functions as for non-annealed E2335 (Figure 17).

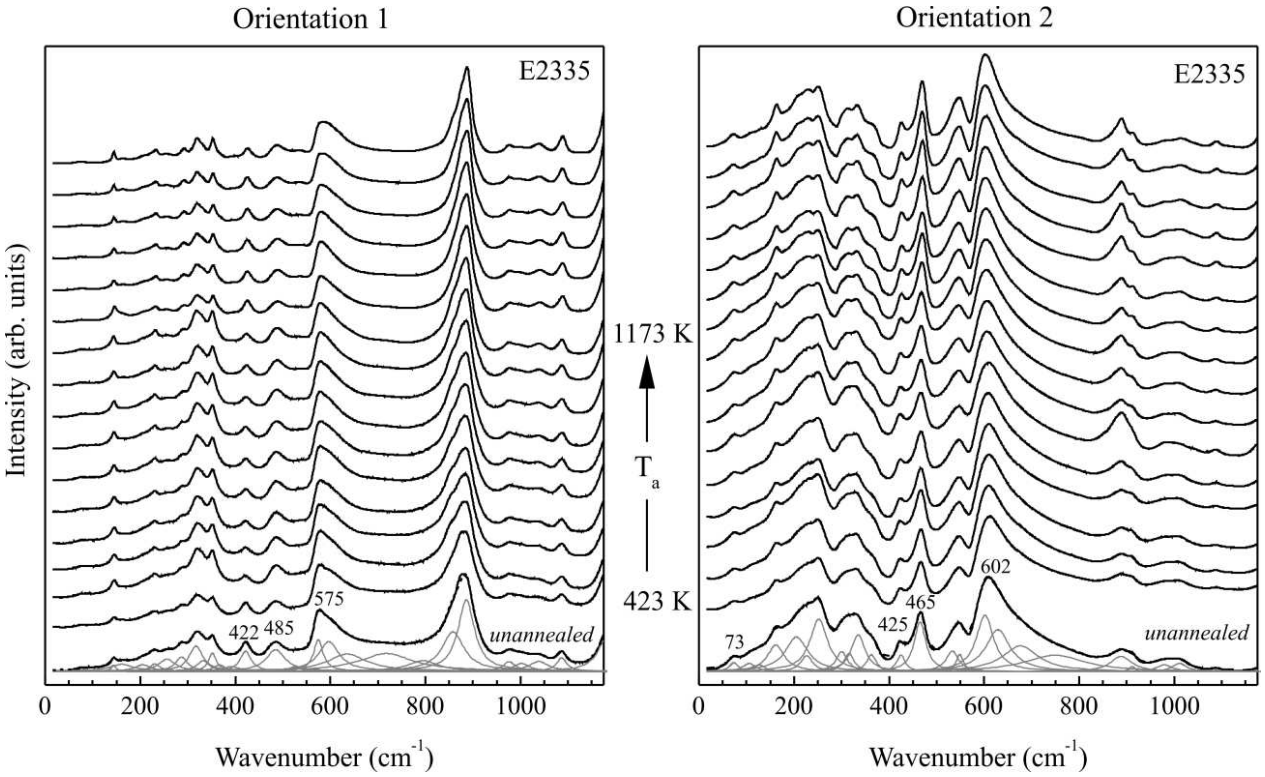

Figure 17: Raman spectra of E2335 titanite measured in orientation 1 and orientation 2 before and after the multi-step annealing at temperatures between 423-1173 K with 50 K step, annealing time at each step of 2 h. The gray lines represent the fitting Lorentzians to the spectra measured before annealing, the dashed lines are the corresponding resultant spectral profiles. The wavenumbers of the peaks further discussed in the text are also given in the plots.

The position of the peak near 600 cm^{-1} arising from the Ti-O bond stretching increases with increasing annealing temperature T_{an} up to T_{an} ~ 900 K, then remains nearly constant in orientation 1 (Figure 18). The FWHM of this peak generally decreases with increasing annealing temperature, as the trend is more pronounced at higher T_{an}.

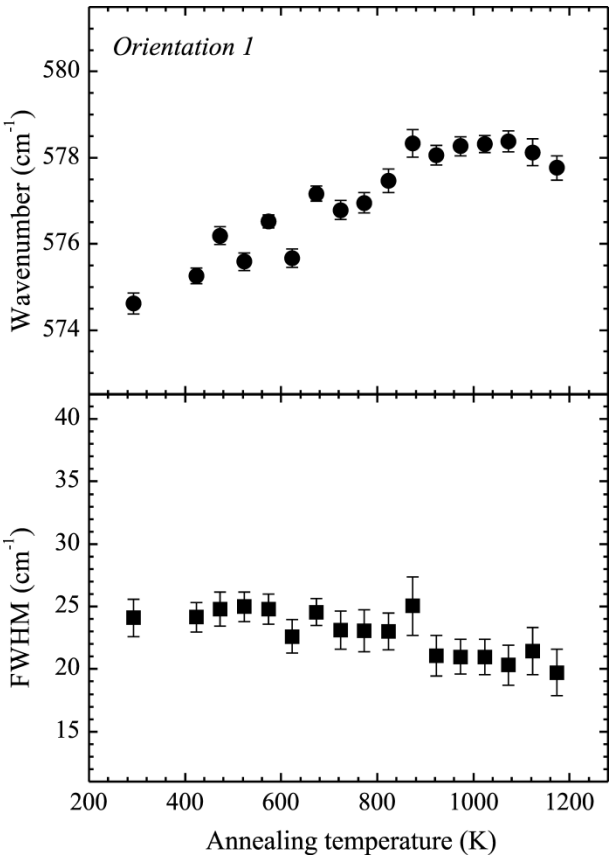

Figure 18: Wavenumber and FWHM versus annealing temperature for the peak near 575 cm^{-1}, arising from Ti-O bond stretching, measured from E2335 titanite in orientation 1 (error bars represent the uncertainties obtained from the spectrum-profile fittings).

The peaks near 422 and 485 cm^{-1} measured in orientation 1 related to SiO_4 bending modes (Figure 19) as well as the external SiO_4 mode near 287 cm^{-1} exhibit the same dependence, an increasing wavenumber and a decreasing FWHM, on the annealing temperature.

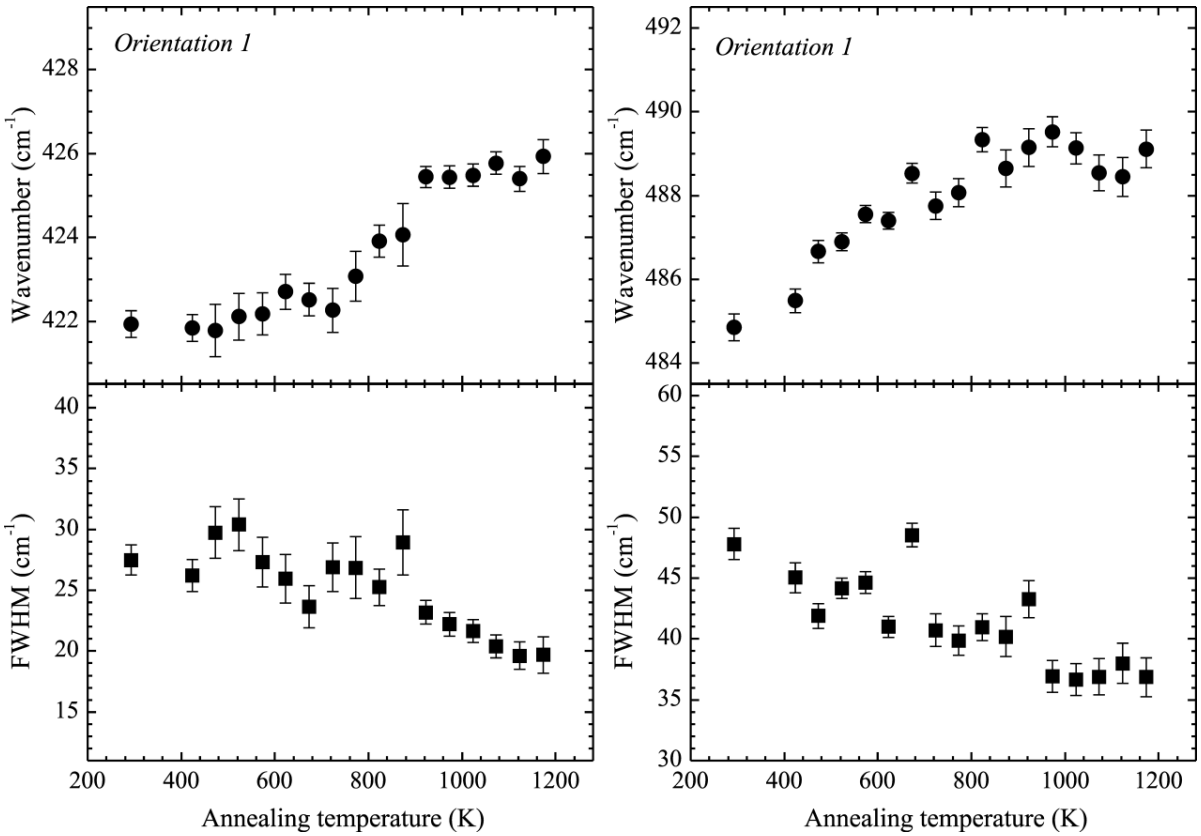

Figure 19: Wavenumber and FWHM versus annealing temperature for the peaks near 422 and 485 cm^{-1} related to bond O-Si-O bending modes measured from E2335 titanite in orientation 1 (error bars represent the uncertainties obtained from the spectrum-profile fittings).

The Raman signal measured in orientation 2 near 603 cm^{-1} is generated by Ti-O bond stretching and decreases in wavenumber with increasing T_{an} (Figure 20). This Raman peak also shows an excess in the FWHM with a maximum near 750 K.

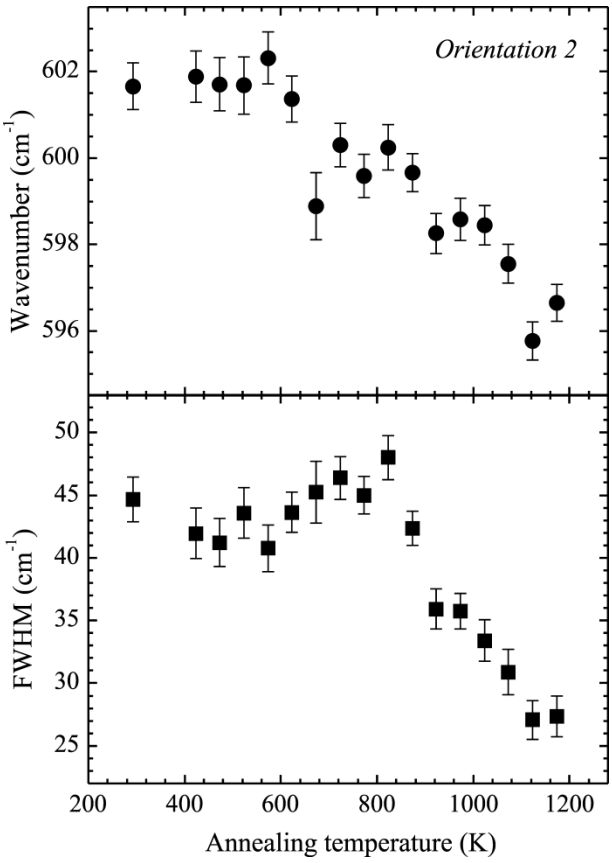

Figure 20: Wavenumber and FWHM versus annealing temperature for the peak near 607 cm^{-1}, arising from Ti-O bond stretching, measured from E2335 titanite in orientation 2 (error bars represent the uncertainties obtained from the spectrum-profile fittings).

The Raman peaks measured in orientation 2 that are related to O-Si-O bond bending vibrations broaden between 650 and 950 K with a strong maximum of the FWHM versus T_{an} near 750 K (Figure 21). Their peak positions remain unchanged up to T_{an} ~ 650 K, then they strongly increase, and above ~ 900 K they are constant.

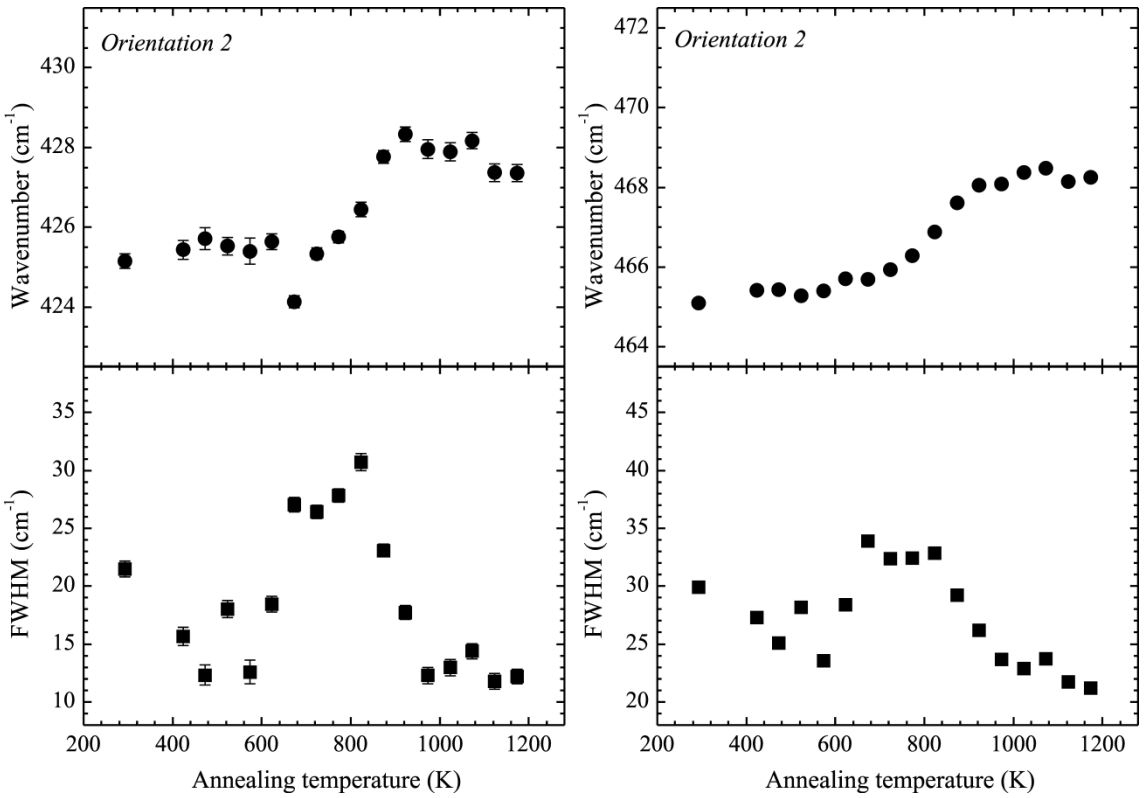

Figure 21: Wavenumber and FWHM versus annealing temperature for the peaks near 422 and 485 cm^{-1} related to bond O-Si-O bending modes measured from E2335 titanite in orientation 2 (error bars represent the uncertainties obtained from the spectrum-profile fittings).

The lowest-energy mode occurring near 72 cm^{-1} observed in orientation 2 also shows a maximum of the FHWM near 750 K and a slight shift to lower wavenumbers (Figure 22).

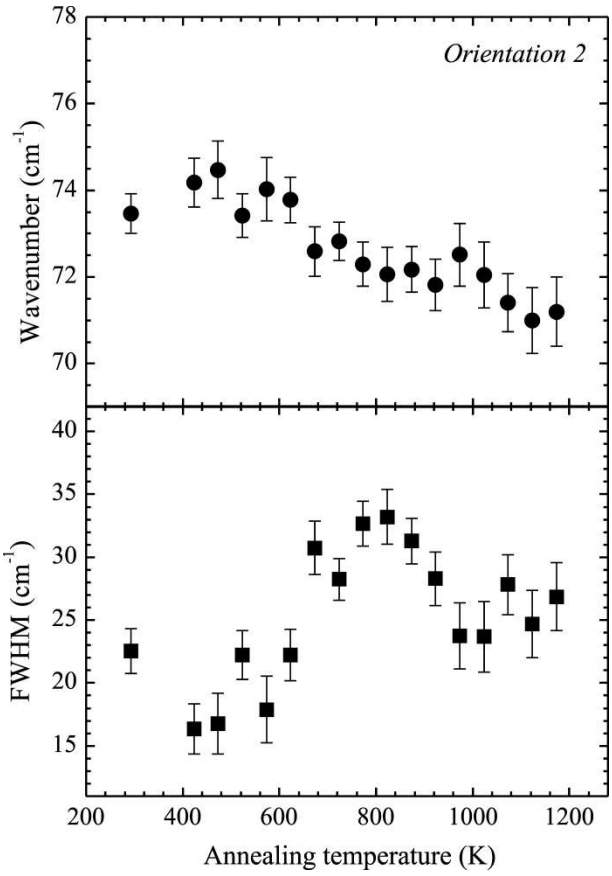

Figure 22: Wavenumber and FWHM versus annealing temperature for the lowest-energy peak near 73 cm^{-1} measured from E2335 titanite in orientation 2 (error bars represent the uncertainties obtained from the spectrum-profile fittings).

Metamict titanite sample E2312

Nanoindentation

The nanoindentation measurement results of the metamict E2312 titanite sample measured at RT and after stepwise annealing for 2 h at 600, 950 and 1220 K, indented perpendicular to the crystallographic plane $(22\bar{3})$ (Figure 24), are shown in Figure 23. The indentation measurements were performed after cooling down to RT respectively. The average hardness (H) of the mineral decreases for T ≤ 950 K from 11.07 ± 0.25 GPa (RT) to 9.08 ± 0.25 GPa (950 K) and increases up to 9.83 ± 0.25 GPa at higher annealing temperatures (1220 K) (Figure 23a). The average elastic modulu (E) increases with rising annealing temperature from 158.4 ± 3.4 GPa (RT) up to 168.4 ± 3.4 GPa (1220 K) (Figure 23b). For comparison, the average H and E values of natural titanite from Rauris indented perpendicular to the crystallographic planes (Figure 24) $(10\bar{1})$ (H = 10.63 ± 0.45 GPa; E = 174.7 ± 3.4 GPa) and $(2\bar{1}3)$ (H = 12.41 ± 0.33 GPa; E = 241.3 ± 2.3 GPa) and of titanite glass (H = 10.41 ± 0.13 GPa; E = 150.3 ± 1.3 GPa) are included. These both samples were thermally untreated. The average hardness and the average elastic modulus of the Rauris titanite sample show strong anisotropy (Figure 23), while our indenter technique did not allow to quantify the anisotropic behavior of the metamict sample E2312.

The nanoindents in the titanite sample E2312 performed after different annealing temperatures are shown in the Figures 25 – 27. Nanoindents in titanite glass (Figure 28) and in nonmetamict Rauris titanite (Figure 29) are also displayed. The triangle shape of the diamond indentation head with Berkovich geometry is recognizable in each case.

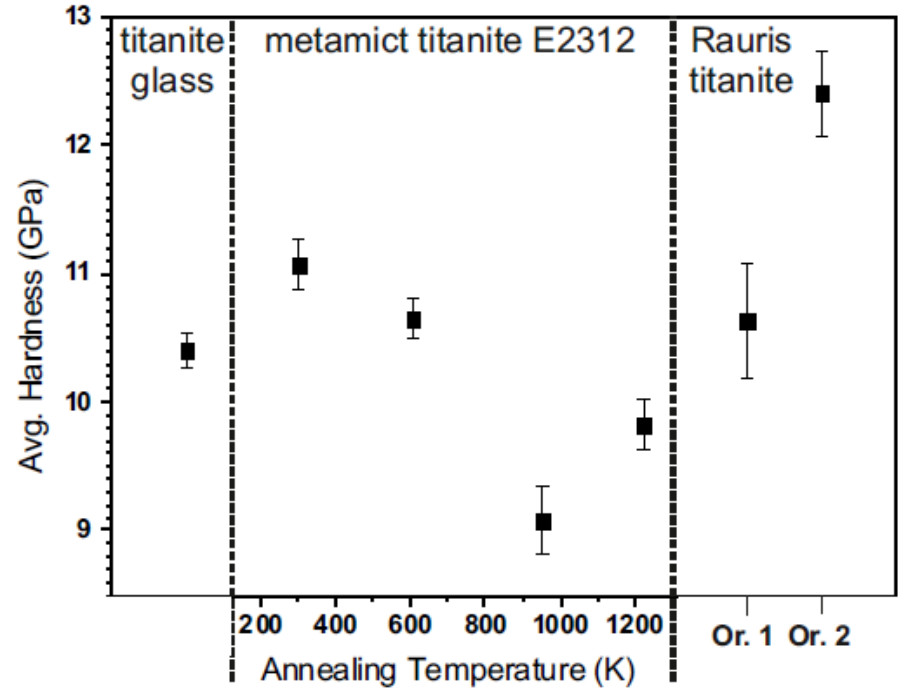

Figure 23a: Average hardness (H) of E2312 titanite at RT and after stepwise annealing for 2 h at 600 K, 950 K and 1220 K. For comparison the H of titanite glass and crystalline Rauris titanite for two orientations (indented perpendicular to $(10\bar{1})_{Or.1}$ and $(2\bar{1}3)_{Or.2}$) are shown at RT.

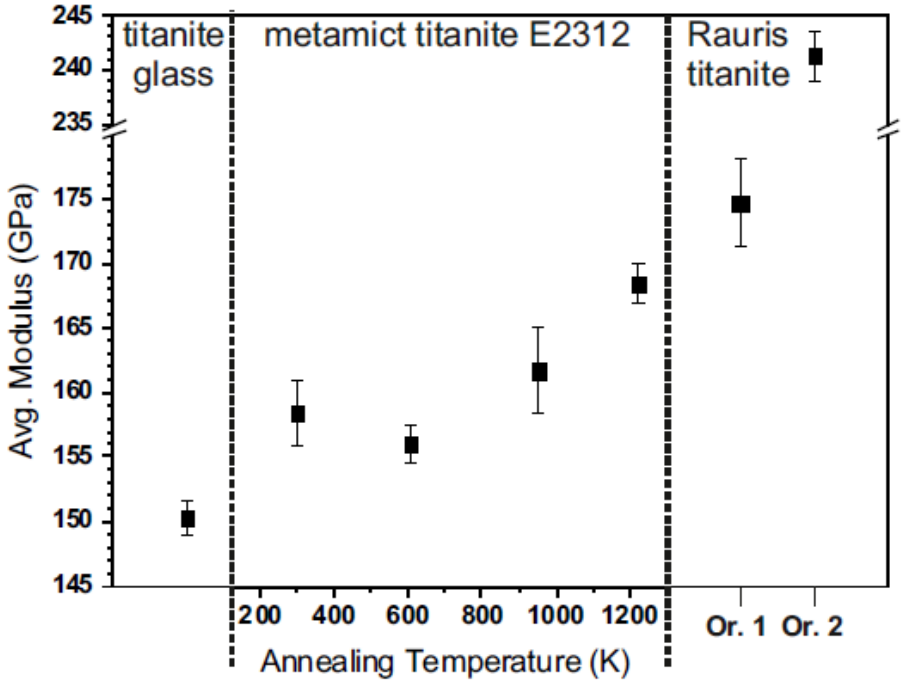

Figure 23b: Average elastic modulus (E) of E2312 titanite at RT and after stepwise annealing for 2 h at 600 K, 950 K and 1220 K. For comparison the E of titanite glass and crystalline Rauris titanite for two orientations (indented perpendicular to $(10\bar{1})_{Or.1}$ and $(2\bar{1}3)_{Or.2}$) are shown at RT.

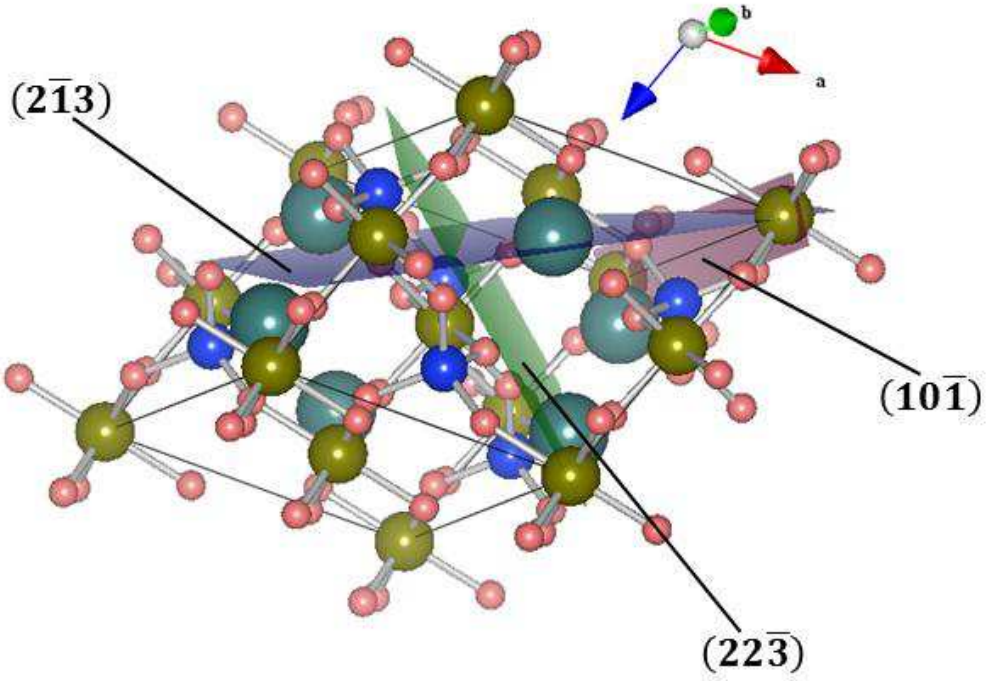

Figure 24: Indentations perpendicular to the crystallographic planes $(22\bar{3})$ in titanite E2312 (blue plane) and $(10\bar{1})$ (orientation 1, red plane) and $(2\bar{1}3)$ (orientation 2, green plane) in Rauris titanite.

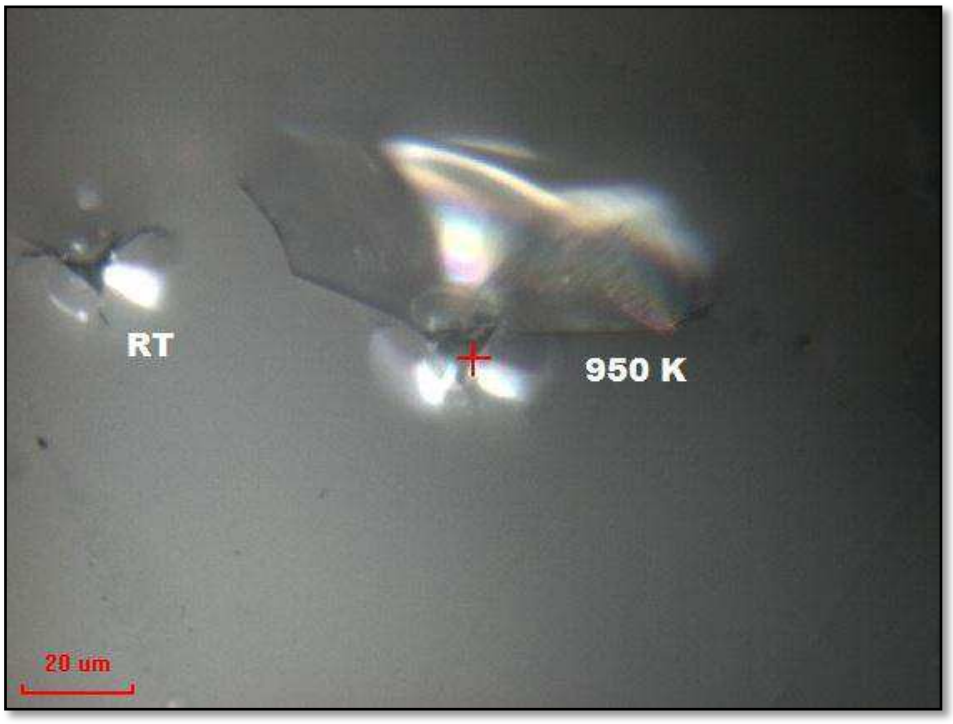

Figure 25: Optical micrograph of nanoindents performed each time at RT in E2312 metamict titanite; unannealed (RT) and after 2 h annealing at 950 K respectively.

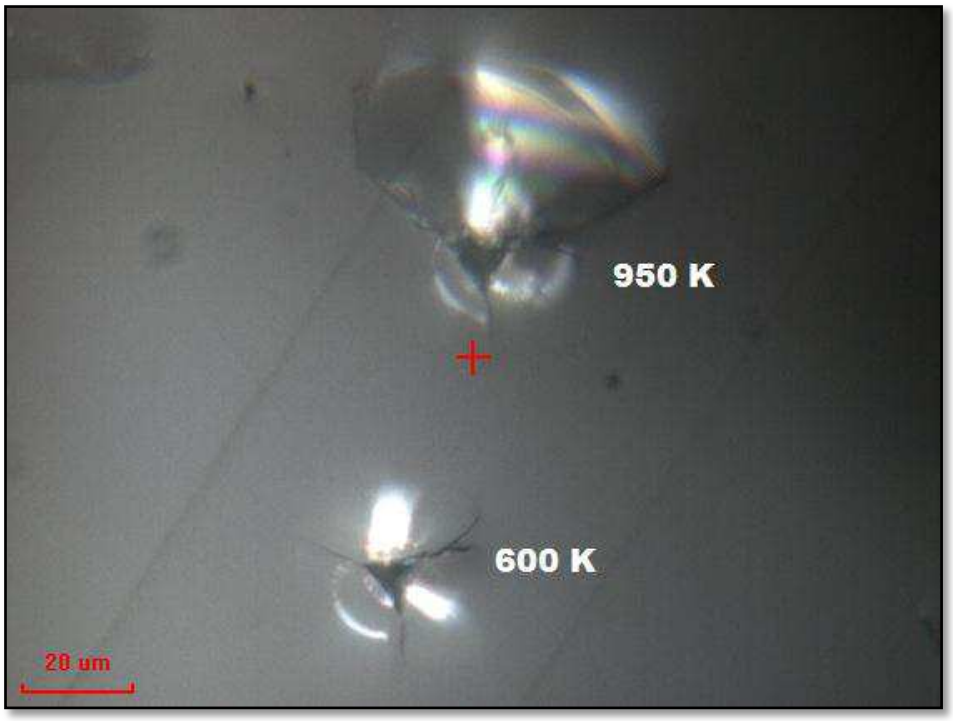

Figure 26: Optical micrograph of nanoindents performed each time at RT in E2312 metamict titanite; after 2 h annealing at 600 K and 950 K respectively.

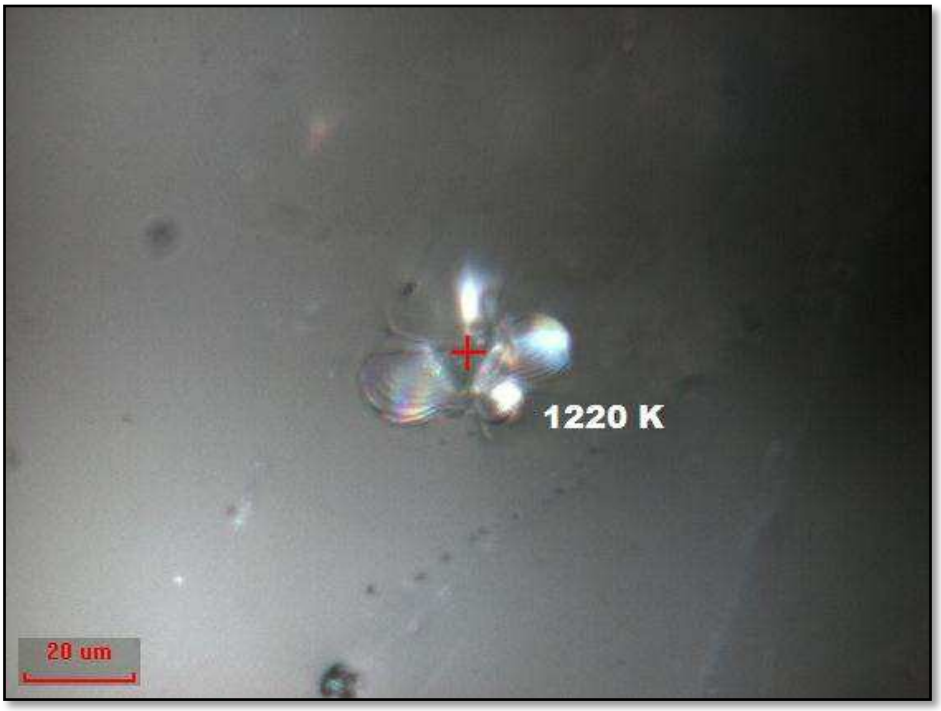

Figure 27: Optical micrograph of nanoindents performed each time at RT in E2312 metamict titanite; after 2 h annealing at 1220 K.

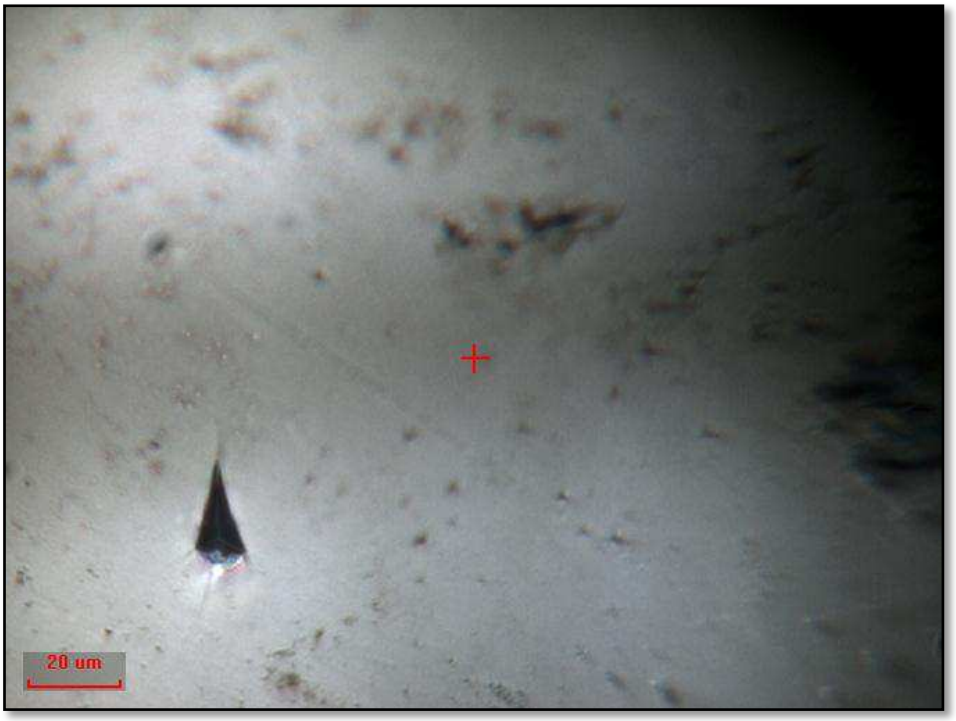

Figure 28: Optical micrograph of a nanoindent performed at RT in titanite glass.

Figure 29: Optical micrograph of a nanoindent performed at RT in nonmetamict titanite from Rauris (Rauris titanite).

Synchrotron X-Ray diffraction

The integrated intensity of the $(\bar{1}\,\overline{11}\,5)$ reflection versus the sample rotation angle φ of metamict titanite E2312 measured at RT and after stepwise annealing for 2 h at 600, 950 and 1220 K is shown in Figure 30. The measurements were always performed after cooling down the sample to RT.

In Figure 31a the decreasing FWHM of the Voigt profile ($FWHM_{Voigt}$) with increasing temperature is shown. The development of the FWHM of the Gaussian ($FWHM_{Gauss}$) and the Lorentzian ($FWHM_{Lor}$) contributions to the Voigt profiles with increasing annealing temperature are displayed in Figure 31b and 31c. The $FWHM_{Lor}$ decreases to nearly zero and the $FWHM_{Gauss}$ shows only a slight decrease. The reduction of the amount of the Lorentzian contribution and the evolution of the Gaussian shape of the rocking curve Voigt profile with increasing annealing temperature is indicated by a decreasing shape factor with increasing annealing temperature (Figure 31d). The results are confirmed by a similar behavior of the $(3\bar{3}6)$ reflection.

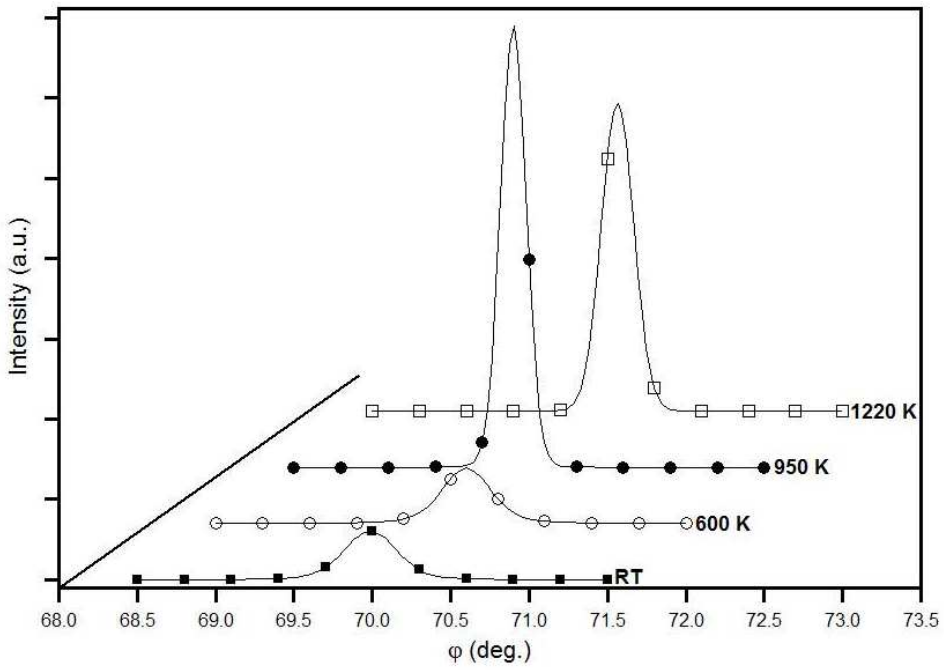

Figure 30: Integrated intensity of the $(\bar{1}\,\overline{11}\,5)$ reflection of E2312 titanite versus sample rotation angle φ at RT and after stepwise annealing for 2 h at 600, 950 and 1220 K.

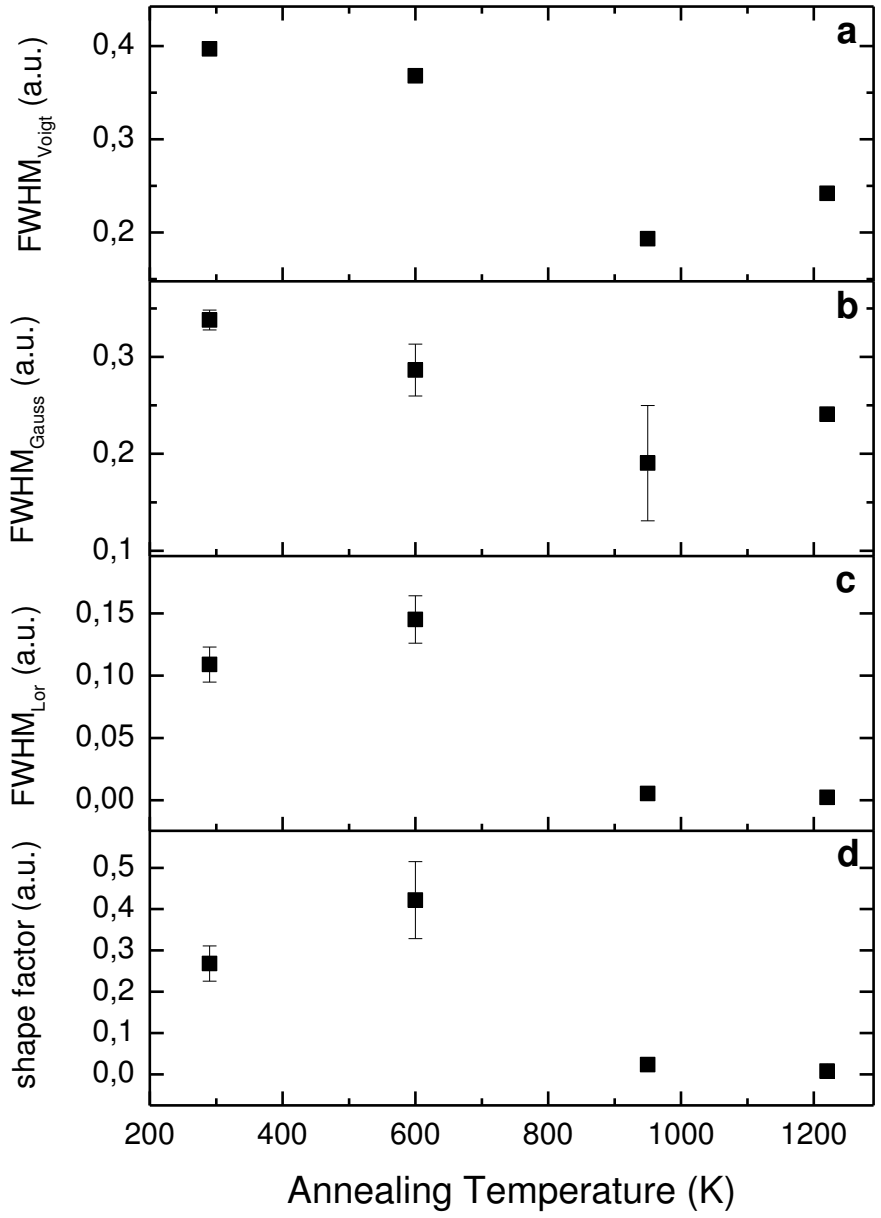

Figure 31: (a) Decreasing width of the Voigt profile (FWHM$_{Voigt}$) with increasing annealing temperature of the ($\bar{1}\ \bar{1}1\ 5$) reflection of E2312 titanite. (b) Evolution of FWHM of the Gaussian (FWHM$_{Gauss}$) and (c) the Lorentzian (FWHM$_{Lor}$) contributions to the Voigt profile. (d) Shape factor for increasing annealing temperature of the rocking curve Voigt profile.

Raman spectroscopy

The Raman spectra of the metamict titanite sample E2312 were measured in two orientations at RT and after stepwise thermal annealing for 2 h at 600, 950 and 1220 K (Figure 32a, b). Both orientations are in the same plane but with the different sample rotation angles of 135° (orientation 1) (Figure 32a) and 45° (orientation 2) (Figure 32b). At these sample positions the spectra show the most prominent differences. Raman spectroscopic measurements were performed at exactly the same sample as the nanoindentation measurements. The Raman spectra from annealed E2312 titanite were effectively fitted using the same number of Lorentzian functions as for non-annealed E2312 titanite (Figure 32). The intensities of the measured spectra distinctly increase and the Raman peaks sharpen after annealing up to 950 K. This is indicated by the increasing wavenumbers und decreasing FWHM.

In orientation 1 the peak related to bond O-Si-O bending modes at 423 ± 0.4 cm^{-1} shifts to 427.5 ± 0.4 cm^{-1} and the peak related to Si-O stretching modes at 878.8 ± 0.4 cm^{-1} to a position at 883.5 ± 0.2 cm^{-1} (Figure 33). The FWHM decreases from 37 ± 4 cm^{-1} to 28.3 ± 2.9 cm^{-1} and from 58.8 ± 1.3 cm^{-1} to 34.1 ± 0.7 cm^{-1}, respectively (Figure 33).

The peak related to bond O-Si-O bending modes measured in orientation 2 shows the same trends in the evolutions of the wavenumber (from 465.8 ± 0.9 cm^{-1} to 467.6 ± 0.6 cm^{-1}) and FWHM (from 48.1 ± 6.7 cm^{-1} to 36.4 ± 3.2 cm^{-1}) (Figure 34).

In contrast the peak near 632 ± 0.7 cm^{-1} generated by Ti-O bond stretching shows a different trend (Figure 34). The wavenumber decreases with increasing annealing temperature from 632 ± 0.7 cm^{-1} to 627.8 ± 0.8 cm^{-1} and the FWHM also decreases from 123.7 ± 3.1 cm^{-1} to 95.8 ± 3.2 cm^{-1} (Figure 34).

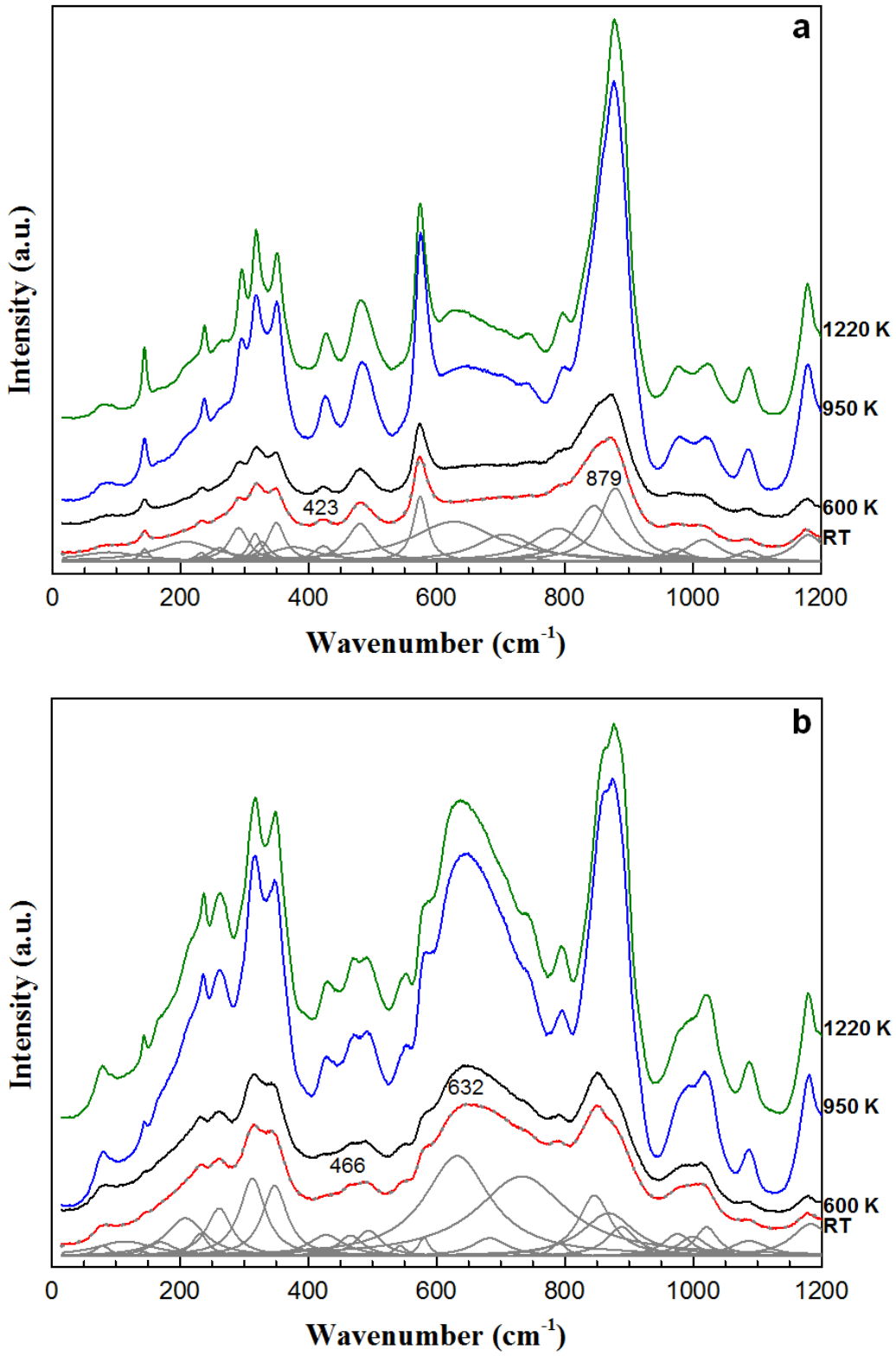

Figure 32: Raman spectra of E2312 titanite measured in orientation 1 (a) sample rotated through 135° and orientation 2 (b) sample rotated through 45°, before and after the multi-step annealing at 600, 950 and 1220 K, with an annealing time of 2 h at each step. The gray lines represent the fitting Lorentzians to the spectra measured before annealing, the dashed lines are the corresponding resultant spectral profiles. Wavenumbers of peaks further discussed in the text are also given in the plots.

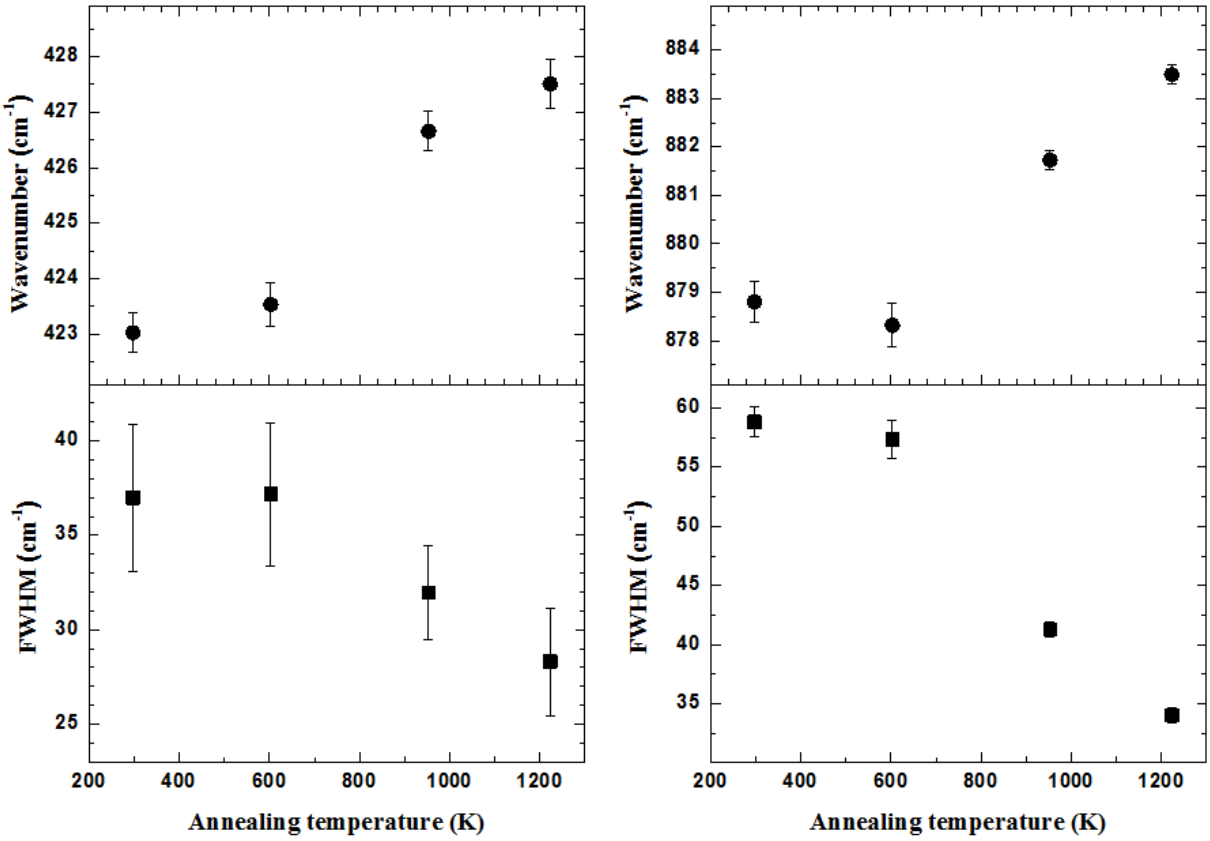

Figure 33: Wavenumber and FWHM versus annealing temperature of the Raman peaks near 423 and 879 cm^{-1} (related to bond O-Si-O bending modes and Si-O stretching modes, respectively) measured from E2312 titanite in orientation 1 (error bars represent the uncertainties obtained from the spectrum-profile fittings).

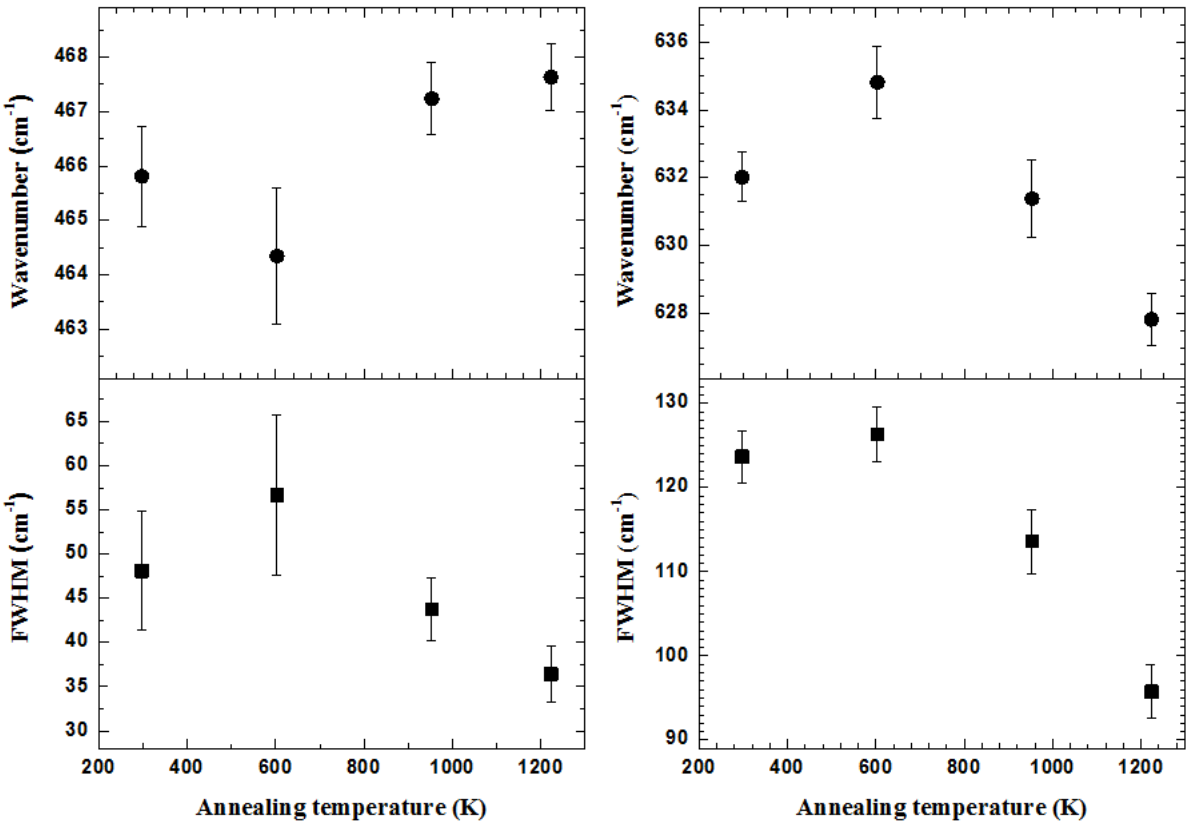

Figure 34: Wavenumber and FWHM versus annealing temperature of the Raman peaks near 466 and 632 cm^{-1} (related to bond O-Si-O bending modes and Ti-O bond stretching, respectively) measured from E2312 titanite in orientation 2 (error bars represent the uncertainties obtained from the spectrum-profile fittings).

Metamict allanite

Chemical analysis

The results of the electron microprobe analysis of metamict allanite R1 are shown in Table 3. Additional analyses by XRF confirmed the EMPA data. The metamict allanite R1 sample contains ~2.87 wt.% ThO_2 and ~18.4 wt.% REE oxides. The chemical composition was calculated from the combined results of the EMPA and XRF analysis (Table 3). The difference of 7.36 wt.% in the sum of the EMPA results (Table 3) is probably due to the presence of OH groups and water in the allanite structure.

Table 3: EMPA results of metamict allanite, R1. Cation distribution deduced from the results of EMPA and XRF analysis.

SiO_2	TiO_2	ThO_2	UO_2	Al_2O_3	Y_2O_3	Ce_2O_3	La_2O_3	Nd_2O_3	FeO*	MgO	CaO	Sum
30.79	0.73	2.87	n.d.	13.02	0.14	10.05	6.15	2.06	15.57	0.61	10.65	92.64
Cations per fomula unit on basis of 12.5 O atoms												
Si	Ti	Th	U	Al	Y	Ce	La	Nd	Fe	Mg	Ca	
1.025	0.018	0.022	–	0.383	0.002	0.092	0.057	0.018	0.217	0.015	0.19	

n.d.: not determined
* total Fe as FeO

X-ray powder diffraction

In Figure 35 the XRD patterns for the room temperature untreated metamict allanite and the effect of annealing for 1800 s each time at 873 K, 1073 K and 1123 K are shown. The Bragg peak at 27º 2θ arises from quartz, and the peaks at 28.20º, 47.32º and 56.10º are produced by CaF_2, which was added as an internal standard. The Bragg peaks produced by allanite are at room-temperature strongly broadened due to the high degree of metamictization. At 27 -34º 2θ only a broad diffuse background is detectable. Thermal annealing at 873 K for 30 min leads to no detectable change in the diffraction pattern, whereas annealing at 1073 K and 1123 K leads to marked increases of the intensities of Bragg peaks. At 1073 K, additional sharp peaks occur at 30.42, 32.22,

32.86, 39.30, 42.38, 50.10 and 50.70º 2θ. Further increases in the intensities of the 013 peak (33.18º 2θ) and the 020 peak (31.26º 2θ) are apparent at 1123 K.

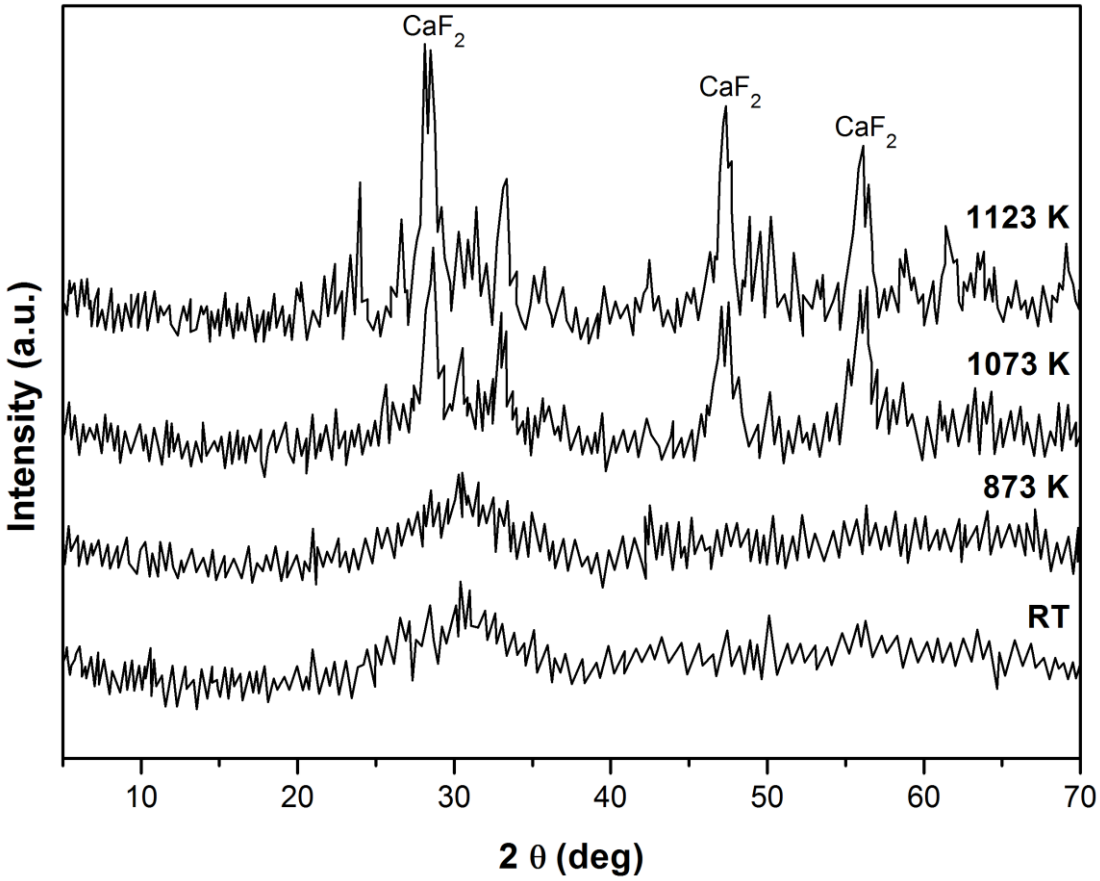

Figure 35: Diffraction patterns of the R1 allanite sample at RT and after annealing for 1800 s at 873 K, 1073 K and 1123 K.

Synchrotron single-crystal XRD

The variation in the intensity of the (007) reflection versus the sample rotation angle φ of allanite R1 at room-temperature and after stepwise annealing for 15 min at 798, 898, 948, 998, 1023 and 1073 K is shown in Figure 36a. The metamict allanite sample was annealed isothermally at 1073 K for another 2 h and the (007) reflection was measured every 30 min; these data are shown as dotted lines. Figure 36b exhibits the slight reduction of the full-width-at-half-maximum (FWHM) of the (007) reflection as a

function of increasing annealing temperature. Because of large uncertainties in the FWHM the weak intensities at 798 K and 898 K are not included. The reduction of the FWHM with annealing time is shown for a 2 h annealing period at 1073 K in Figure 36c.

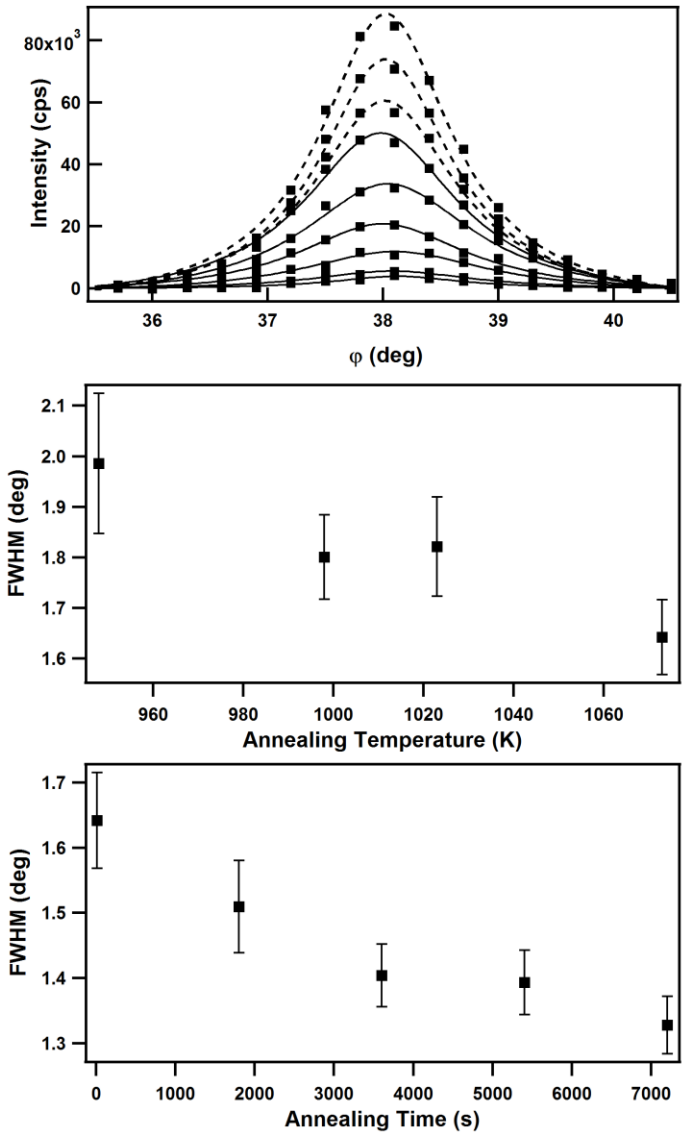

Figure 36: (a) Integrated intensity of the (007) reflection versus the sample rotation angle φ for metamict allanite R1, after stepwise annealing for 900 s at 798 K, 898 K, 948 K, 998 K, 1023 K and 1073 K (solid lines). At 1073 K the allanite sample was annealed for 2 h and measured every 1800 s (dashed lines). (b) FWHM of the (007) reflection as a function of temperature after annealing for 900 s at temperatures 948, 998, 1023 and 1073 K. (c) FWHM of the (007) reflection as a function of annealing time, displayed for a 2 h annealing period at 1073 K.

In Figure 37a the variation of the intensity of the $(2\bar{2}2)$ reflection during annealing at 823 K versus the rotation angle φ of the allanite sample over a total annealing period of 2.6 h is shown. Figure 37c shows the evolution of the FWHM data and Figure 37b the changes of the intensity as functions of time for the $(2\bar{2}2)$ reflection. Because of large uncertainties the FWHM value of the peak that was recorded at the beginning of the series of measurements is not plotted. From Figure 37d a decrease in the unit-cell volume on annealing of ~ 1.2% is evident.

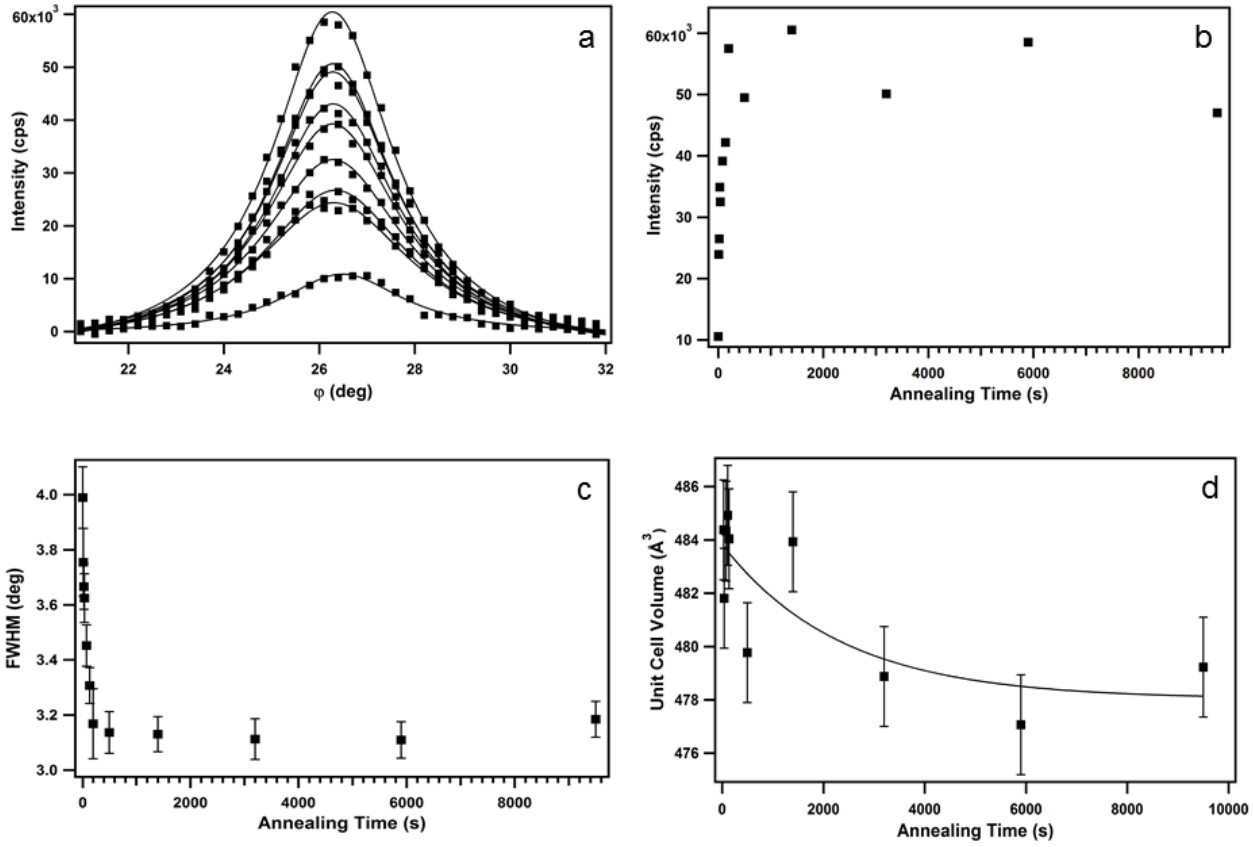

Figure 37: (a) Intensities of the $(2\bar{2}2)$ reflection of metamict allanite R1 during isothermal annealing at 823 K versus the sample rotation angle φ of the allanite sample for a total annealing period of 9500 s (measured at periods of 10 s to 9500 s). (b) Intensity as a function of time of the $(2\bar{2}2)$ reflection. (c) Evolution of the FWHM as a function of time of the $(2\bar{2}2)$ reflection. (d) Decrease of the unit-cell volume with annealing time (line guided for the eyes).

The recrystallization kinetics of the metamict allanite R1 sample during isothermal annealing was investigated using the Sharp-Hancock procedure. The evolution of the normalized inverse FWHM of the $(2\bar{2}2)$ Bragg-reflection of the metamict allanite, defined as α, which is a sensitive index of the increase in the crystallinity of the sample (Hancock and Sharp, 1972). The corresponding Sharp-Hancock plot is of the form

$$\ln[-\ln(1 - \alpha)] = n \ln(t - t_0) + n \ln k \qquad (3.1)$$

in which t is the time of reaction (9500 s) and k is the rate constant of the reaction. The Sharp-Hancock plot displays ln[-ln(1 - α)] versus ln(t) (logarithmic annealing time) (Francis et al., 1999). The Sharp-Hancock plot of the inverse FWHM of the $(2\bar{2}2)$ reflection as a function of annealing time at 823 K (Figure 38) shows at least two distinct linear regimes.

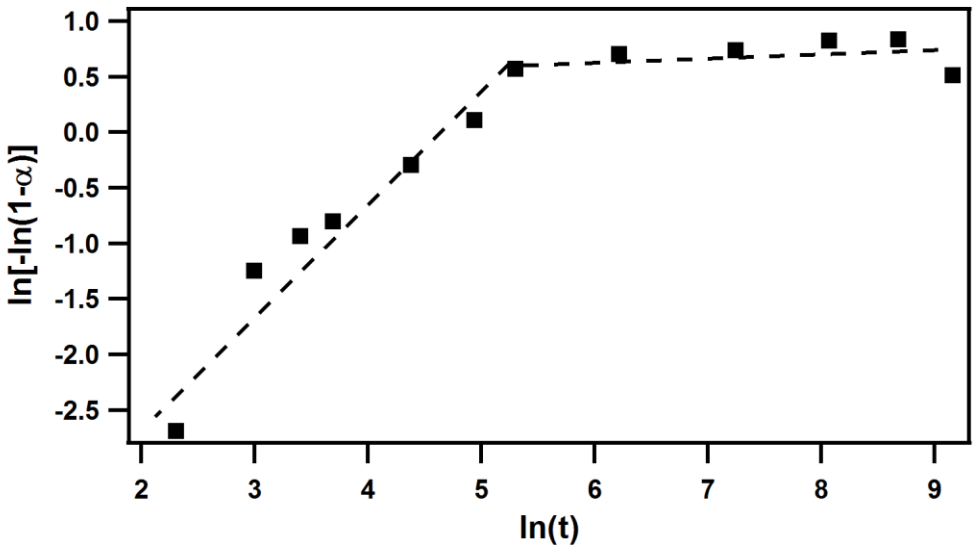

Figure 38: Sharp-Hancock plot of the $(2\bar{2}2)$ diffraction intensity data of metamict allanite R1 obtained at T = 823 K, at least two distinct linear regimes are visible (uncertainties are within the size of the symbols, lines guided for the eyes).

Fourier-transformed infrared spectroscopy (FTIR)

The FTIR spectra of the metamict allanite sample R1 at room-temperature and after annealing at 723, 823 and 923 K for 1200 s are shown in Figure 39. At 723 K the Si-O tilting modes between 400 cm^{-1} and 600 cm^{-1} and the Si-O stretching mode between 900 cm^{-1} and 1100 cm^{-1} remain heavily broadened (Moenke, 1962). The stretching modes of the structural hydroxide groups (O-H) take place between 3350 cm^{-1} and 3600 cm^{-1} and appear almost unchanged by the annealing procedure. Thermal annealing to 823 and 923 K leads to an increase in the intensity of the Si-O tilting mode absorption bands, which lie between 450 cm^{-1} and 700 cm^{-1}, as well as the Si-O stretching mode between 900 cm^{-1} and 1100 cm^{-1} (Moenke, 1962).

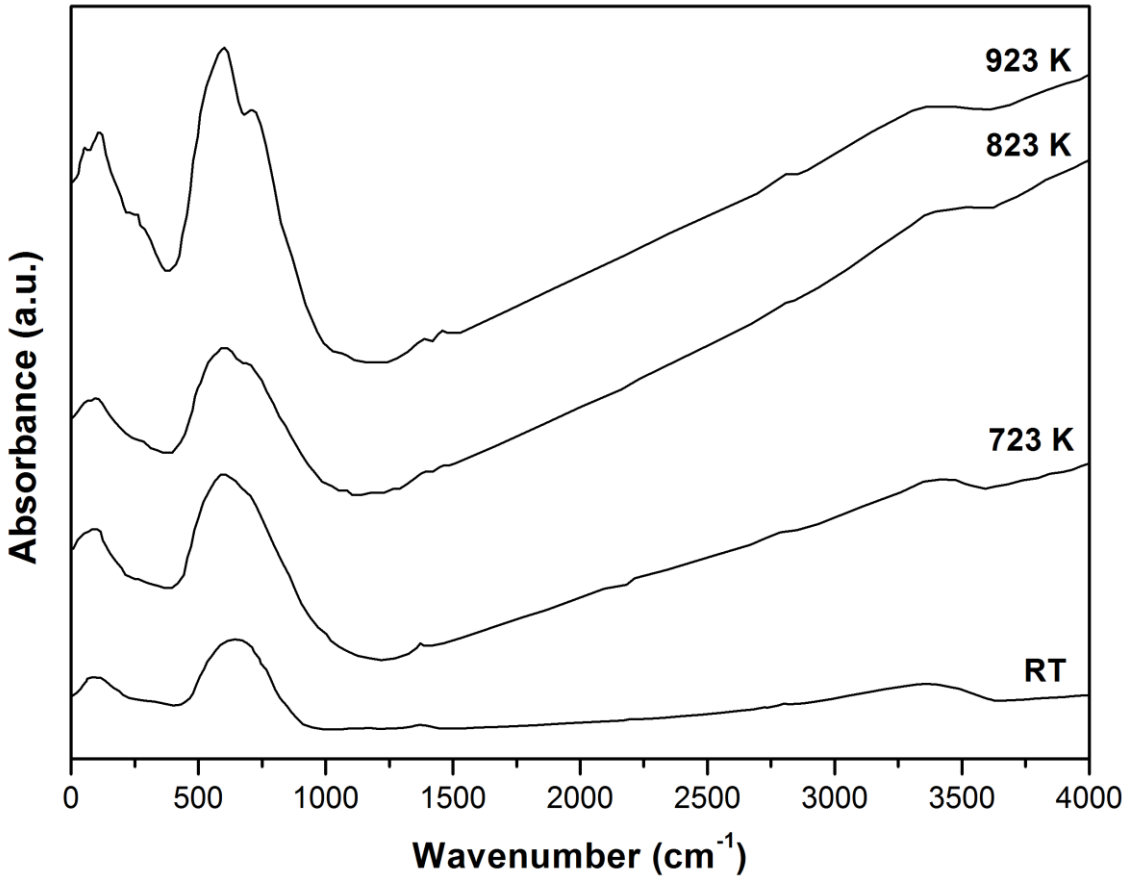

Figure 39: Room temperature IR spectra of metamict allanite R1 before and after annealing at 723, 823 and 923 K for 1200 s each step.

4 Discussion

Metamict Titanite

Relation between Raman scattering and the degree of radiation-induced damage

A remarkable result of this study is that even highly metamict titanite (M28696 Cardiff) exhibits a strong dependence of the Raman spectra on the orientation of the sample with respect to the direction of the polarization of the incident laser light (Figure 8). This clearly shows that the structure is highly anisotropic, which is a typical property of framework structures. This is also supported by the fact that the Raman spectra collected from the Cardiff titanite sample (damage index 10 out of 10) differs from that of titanite glass. The comparison between Raman scattering collected in orientations 1 and 2 suggests that radiation-induced defects anisotropically accumulate in the titanite structure, following a favorable crystallographic direction of the parent crystalline structure.

The behavior of the Raman scattering of metamict titanite measured in orientation 1 (Figure 8) is consistent with the swelling of the unit cell volume (Paulmann et al., 2000) and it seems that in this orientation the inelastic light scattering by atomic vibrations corresponds to an interaction process between photons and phonons in crystallites with slightly disturbed periodicity. Even if these crystallites are separated from each other by amorphous material, their mutual long-range coherence along this particular crystallographic direction is more or less preserved.

It could be assumed that the Raman peak near 670 cm^{-1} in highly metamict titanite arises from IR active Ti–O bond stretching modes which generate the IR absorption band (Figure 8) due to the destruction of periodicity and consequently a breakdown of the symmetry selection rules may be observed. However, if only this would be the case, the peak position would be independent of the damage index and only the intensity would increase with the degree of structural damage. The broad peak near 630 – 660 cm^{-1} in highly metamict titanite may evolve from the peak near 605 cm^{-1} in well-crystalline titanite, which probably arises from a symmetrical mode involving Ti–O bond stretching and Ti–O–Ti bond bending. In metamict titanite, depending on

the degree of radiation induced structural damage, this mode may couple with the higher energy IR-active Ti–O bond stretching modes, which can explain the shift of the broad peak to higher wave numbers with increasing damage index. The strong difference between the Raman spectra collected in orientations 1 and 2 from the same metamict titanite sample clearly indicates that the metamictization structural state is anisotropic. Furthermore, the level of continuum photoluminescence background was much higher in orientation 2 than in orientation 1. This is indicative of a high level of structural defects in the metamict titanite which give rise to low electron energy levels or even bands within the electron energy gap of the host crystalline matrix, i.e. defects are more favorably accumulated along the crystallographic direction corresponding to orientation 2 than to that corresponding to orientation 1. Because of the high degree of periodicity faults, it is difficult to unambiguously determine the crystallographic directions of planes perpendicular to the sample surface that correspond to orientations 1 and 2 for metamict titanite. Examination with polarized light microscopy indicates that for pure synthetic single crystal titanite, orientation 1 should correspond to the case in which the monoclinic b-axis and the polarization of the incident laser light are in the same plane, while orientation 2 corresponds to the case in which the polarization of the incident laser light is approximately perpendicular to the plane containing the b-axis.

Based on the overall Raman-peak broadening, which is indicative of structural defects, it can be suggested that the damage index of sample E2335 is higher than that of M28658 but lower than that of sample M28173 (Figure 8). The Raman scattering data better match the infrared spectroscopy criterion rather than the XRD criterion as defined by Hawthorne et al. (1991). The Raman peak positions and the FWHM apparently correlate with the accumulated radiation doses. In Figure 40 for example, the FWHM of the peak near 462 cm^{-1} measured in orientation 2 is plotted against the α-radiation dose. This peak is particularly suitable to be used for estimating the degree of metamictization because:

1. It arises from the SiO_4 bending mode (Heyns et al. 2000), which means that the peak parameters are least affected by the presence of chemical impurities, which commonly substitute for Ti and Ca.

2. For all metamict samples it is relatively well separated, ensuring small errors in the peak parameters obtained by fitting.

However, a larger number of well characterized samples should be analysed to establish a calibration curve and it should be considered that in general, the Raman peak positions and widths may be also influenced by the geological history of the sample (Geisler and Pidgeon, 2002).

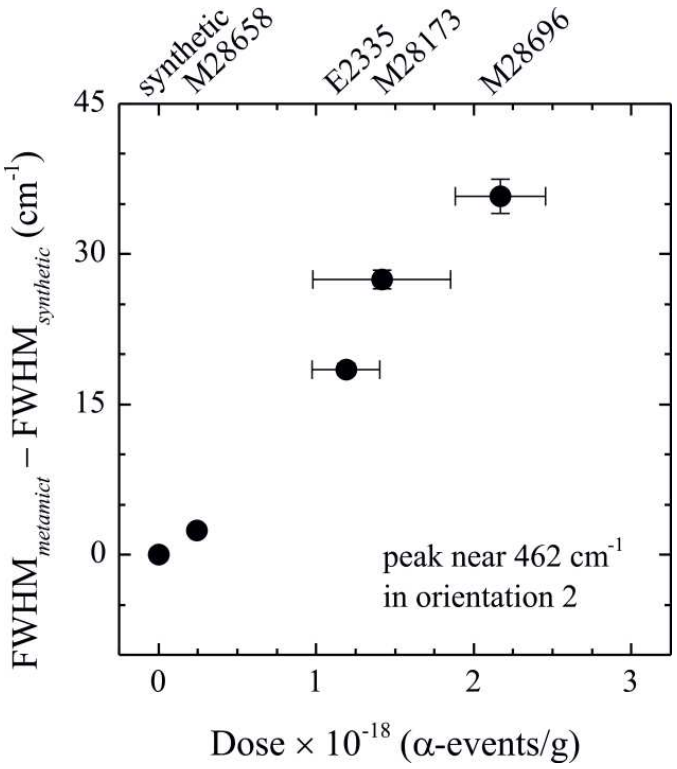

Figure 40: Deviation of the FWHM of the peak near 465 cm^{-1} measured in orientation 2 from the FWHM for synthetic titanite versus the accumulated α-radiation dose (Table 1) (error bars of the widths represent the uncertainties obtained from the spectrum-profile fittings). (Reference FWHM$_{synthetic}$ (of synthetic polycrystalline titanite) = 11.4 ± 0.3 cm^{-1} (Figure 8))

As referred in the second chapter (subitem ‘Group-theory analysis of pure titanite’, page 29) the strongest contribution to the Raman spectra comes from the scattered light which has a polarization $\mathbf{E}_s$ parallel to the polarization of the incident light $\mathbf{E}_i$. The both matrix representations of the Raman polarizability tensors for A_g and B_g modes in a monoclinic system with unique axis b are also given. Hence, the parallel polarized Raman spectra ($\mathbf{E}_i \parallel \mathbf{E}_s$) are generated from the A_g modes, when the monoclinic binary axis coincides with the polarization of the incident light $\mathbf{E}_i$, while the cross polarized spectra ($\mathbf{E}_i \perp \mathbf{E}_s$) result from the B_g modes. In the case of a randomly oriented sample with respect to the scattering geometry, all components of the polarizability tensors for both modes (A_g and B_g) are nonzero, following the transformation rules for a 2^{nd}-rank tensor upon three successive rotations describing the orientation of the sample with respect to the special case b $\parallel \mathbf{E}_i$. Therefore both A_g and B_g modes contribute to the parallel as well as to the cross polarized Raman spectrum and the weight coefficients of the polarizability tensor components are functions of the angles of rotation. For that reason, the Raman scattering intensities in the spectra collected from single crystals of titanite are expected to be orientation-dependent and this dependence should be strong if the difference between the initial tensor components a, b, c, d, e, and f is large. The experimentally observed Raman scattering of synthetic single-crystal titanite exhibits orientational dependence but the disparities in the intensities are not very large. For example, Figure 8 depicts spectra of synthetic single-crystal titanite measured when the monoclinic binary axis was approximately perpendicular to the propagation of the incident light (orientation 1) and when the binary axis was more or less parallel to the propagation of the incident light (orientation 2). The main features of the spectra measured in the two orientations are similar and in particular, the scattering in the range 600-800 cm^{-1} is the same.

M28696 Cardiff titanite

All peaks of the metamict Cardiff titanite Raman spectra in orientation 1 show a shift to lower wavenumbers with increasing temperature due to the thermal expansion effect (Figure 9, 10). However, after annealing the material shows weak recovery of the structure, which is displayed by the peak shifts to higher wavenumbers at 284.8 cm^{-1} (related with external SiO_4 modes), at 419.8 cm^{-1} (O–Si–O bending mode) and at 873.6 cm^{-1} (Si–O stretching mode) observed in orientation 1. As reported in chapter 3 under results the remaining peaks observed in orientation 1 and all those observed in orientation 2 remain unchanged after annealing. This indicates that recovery of the long-range order as detected by XRD is related to stiffening and improvement of the local symmetry of SiO_4 tetrahedra.

Annealing at 600 K for 15 min of this highly metamict sample only slightly affects the degree of disorder. However, annealing at 850 and 900K substantially suppresses the faults in periodicity and improves the crystallite coherence as can be seen from the much better Lorentzian fits to the experimental data sets (Figure 11). The stronger recovery of the periodicity in the titanite structure with higher annealing temperature can be also deduced from the reduction of the FWHM (Figure 12). The width of the Lorentzian peak used to fit the data set measured after annealing at 600 K is within the uncertainties the same as that for thermally untreated Cardiff titanite, whereas the corresponding widths for 850 and 950 K are considerably smaller by approximately a factor of two.

E2335 titanite

The sample E2335 exhibits, similar to other heavily metamict titanite samples with a damage index ≥ 8 (Figure 8), anisotropic Raman spectra (Figure 8). As discussed above, anisotropic Raman scattering is typical of single-crystal solids. The existing crystalline regions are almost coherent to each other, regardless of the amorphous matter between the crystalline nanoregions. This result is in good accordance with the TEM data of E2335, revealing an overall monocrystalline-type electron diffraction pattern recorded from an individual particle and crystalline nanoregions which are only slightly misaligned to each other. On the other hand, as for the other heavily metamict titanite samples, M28173 and M28696, the orientation dependence of the Raman scattering of E2335 is much stronger pronounced than for well crystalline pure titanite and for the nearly undamaged titanite M28658. This result indicates that the strong anisotropy of the Raman scattering of metamict titanite, especially in the range 600-800 cm^{-1}, is related to an anisotropic structural damage. The profile of the Raman signal near 600 cm^{-1} collected from heavily metamict titanite in orientation 1 resembles that of well-crystalline titanite, while the profile of the signal collected in orientation 2 considerably differs from the spectrum of well-crystalline titanite (Figure 8). This Raman peak is typical of TiO_6 stretching (Heyns et al. 2000, Su et al. 2000; Kostov-Kytin et al. 2005). In orientation 1 it slightly broadens and shifts towards lower wavenumbers with increasing degree of metamictization (~ 572 cm^{-1} for the most heavily metamict sample M28696). By contrast, the Raman scattering near 600 cm^{-1} measured in orientation 2 substantially broadens and the intensity maximum shifts towards higher wavenumbers with increase in the degree of metamictization (~ 650 cm^{-1} for the most heavily metamict sample M28696), approaching but not reaching the position of the band near 750 cm^{-1} in the spectrum of titanite glass. The orientation dependence of the Raman scattering of pure single-crystal titanite was thoroughly checked and no Raman spectrum was observed in which the signal at 600 cm^{-1} is suppressed on the account of new signals near 570 or near 650 cm^{-1}. Therefore, these spectral changes cannot be related with orientational effects of pure crystalline titanite but reflect the changes of the Ti-O bond stretching modes related to the radiation-induced structural damage.

The decrease in the position of the Raman peak near 600 cm^{-1} observed in orientation 1 with the degree of metamictization is in full accordance with the radiation-

induced enlargement of the unit-cell volume detected by XRD (Hawthorne et al. 1991). This indicates that the Raman scattering collected in orientation 1 mainly represents the structural state of the crystalline nanoregions.

In amorphous Ti-Si-O frameworks the Ti^{4+} cations can be 6-, 5- and 4-coordinated (Alberto et al. 1995; Nasu et al. 1997). Penta- and tetra-coordinated Ti^{4+} has also been suggested to occur in heavily metamict titanite (Hawthorne et al. 1991; Farges et al. 1997; Zhang et al. 2002). With decreasing Ti coordination the Ti-O bond strength increases. As a consequence the resultant Ti-O bond stretching mode in a disordered framework comprising octa-, penta- and tetrahedrally coordinated Ti would be positioned at higher wavenumbers as compared to the Ti-O bond stretching mode in a framework containing only TiO_6 octahedra. This indicates that the metamictization-related spectral features observed in orientation 2 are sensitive also to radiation-induced amorphization involving a partial change in the Ti coordination and subsequent to rearrangements of the Ti-O-Ti and Si-O-Ti linkages. The local structural species responsible for the atomic vibrations giving rise to the Raman scattering in the two distinctive orientations strongly supports this suggestion. A close examination of the atomic arrangements of titanite shown in Figure 41 reveals that in orientation 1 the polarization of the incident light $\mathbf{E}_i$ lies in a plane approximately perpendicular to the chains of TiO_6 octahedra, while in orientation 2 the vector $\mathbf{E}_i$ is in a plane approximately parallel to the TiO_6-chains. The interchain connectivity is implemented by SiO_4-TiO_6 linkages forming four-membered polyhedral rings of SiO_4-TiO_6-SiO_4-TiO_6 as the two octahedra are from different TiO_6 chains. As shown in Figure 41, these 4-membered rings are approximately in the same plane as $\mathbf{E}_i$ in orientation 1 and therefore peaks generated by ring "breathing" modes, involving in-plane vibrations of the SiO_4-TiO_6 bridging oxygen atoms, would be very sensitive to any connectivity and stacking faults in the periodic atomic framework. On the other hand, the Ti-O stretching vibrations of oxygen atoms linking the TiO_6 octahedra in chains should generate strong Raman peaks in orientation 2. A plausible change in the Ti coordination would not only influence the inter-chain connectivity but it would also induce broken TiO_6-TiO_6 linkages, meaning loss of periodicity in all directions. Therefore, the Raman scattering measured in orientation 2 is much more sensitive to the presence of radiation-induced amorphous regions than that collected in orientation 1.

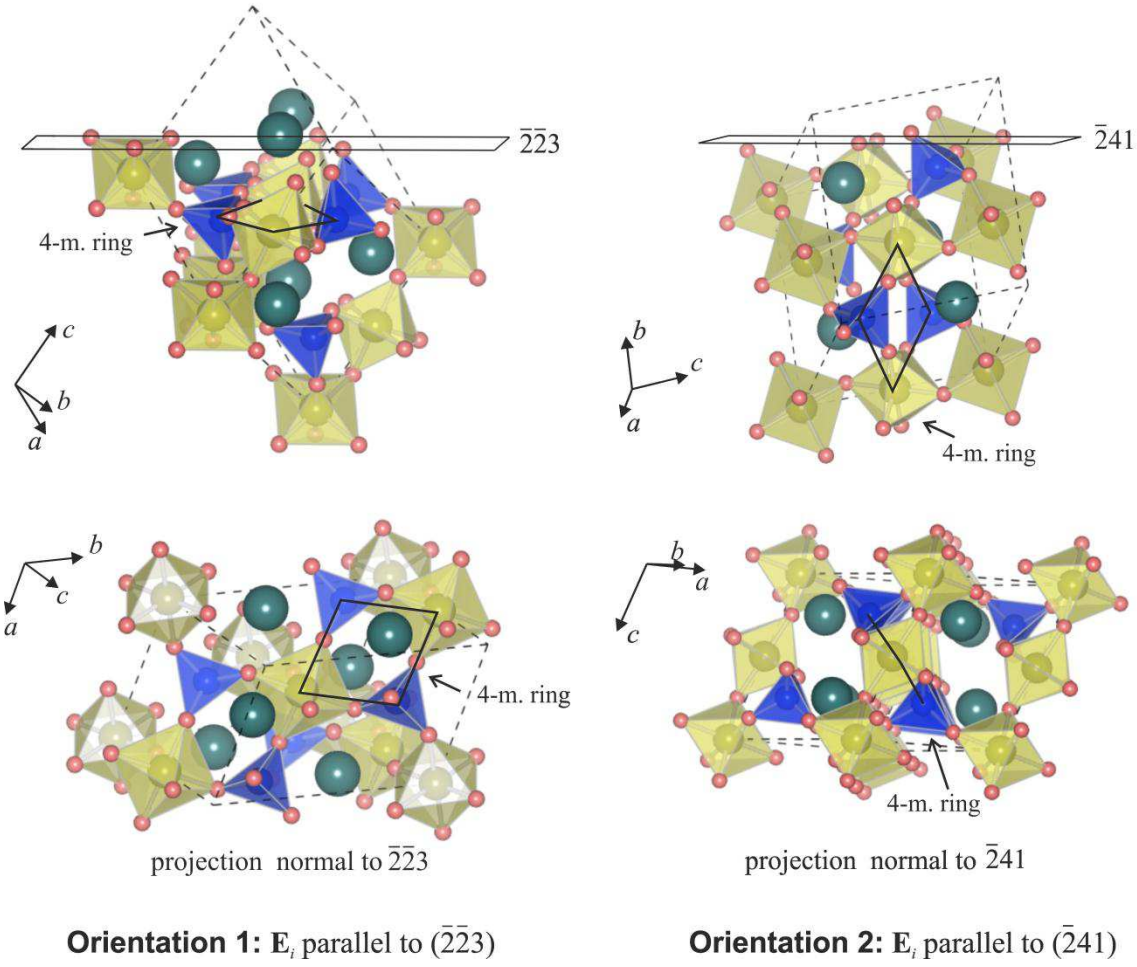

Figure 41: Projections of the titanite structure corresponding to orientations 1 (left) and 2 (right), (figure was prepared using the VESTA software package (Momma and Izumi, 2008)).

The effect of annealing

The dependence of the FWHM on the annealing time for the above-mentioned peaks indicates a gradual recovery of the structure, i.e., it is related to the suppression of defects and enlarged length of structural coherence in the crystalline regions. The saturation of the wavenumbers of the corresponding TiO_6 and SiO_4 phonon modes above T_{an} ~ 900 K indicates that further annealing will lead to negligible improvement of the connectivity of the SiO_4-TiO_6-SiO_4-TiO_6 rings.

As expected, the annealing time dependences of the Raman peaks observed in orientation 2 differ from the trends measured in orientation 1. The excess in the FWHM with a maximum near 750 K of the Raman signal near 603 cm^{-1} generated by Ti-O bond stretching, indicates the occurrence of structural transformations (Figure 20). Conformable to hard-mode spectroscopy (Salje and Bismayer, 1997), a maximum of the FWHM of a Raman or infrared peak as a function of temperature (or any other thermodynamic variable characterizing the system under consideration) reflects the damping of the corresponding phonon mode when the system approaches a phase transition. In the case of metamict titanite exposed to annealing, the maximum of the FWHM as a function of the annealing time corresponds to the temperature at which the fraction of amorphous matter undergoing recrystallization is maximum. Thus, the spectral changes suggest that annealing leads to a recovery of the octahedral coordination of Ti atoms in the titanite structure and consequent improvement of the Ti-O-Ti chain connectivity. The Raman peaks related to O-Si-O bond bending vibrations (orientation 2) show a broadening between 650 and 950 K with a strong maximum of the FWHM near 750 K, which also reveals the occurrence of structural transformations (Figure 21). In addition, the lowest-energy mode occurring near 72 cm^{-1} (orientation 2), which should be indicative of the overall atomic rearrangements, also shows a maximum of the FHWM near 750 K (Figure 22). Thus, all annealing-induced spectral changes detected in orientation 2 indicate that the system undergoes significant structural alteration, which could be attributed to annealing-induced recrystallization of the preexisting amorphous nanoregions in metamict titanite. Annealing enhances the reappearance of 6-coordiated Ti in the non-crystalline regions and thus induces polyhedral linkages typical of crystalline titanite. Therefore, by changing the short- and the intermediate-range order, thermal annealing drives the framework of the radiation-amorphized parts to develop periodicity typical of titanite. The annealing-induced reduction of periodic faults and improved structural correlation in the crystalline nanoregions should facilitate the recrystallization of the amorphous nanoregions in the material. Since the SiO_4 modes giving rise to Raman peaks in orientation 2 show significant excess of FWHM in the T_{an}-range 650 - 950 K, while the SiO_4 modes generating Raman peaks in orientation 1 do not, it can be speculated that the intermediate-range order, namely Ti-O-Si linkages, within the planes normal to the TiO_6

chains is more or less preserved, which supports the process of structural recovery of titanite. However, the annealing of heavily metamict titanite (damage index ≥ 8) up to 1173 K for 2 h per step of 50 K cannot lead to a complete recrystallization of the global titanite structure. The Raman spectral profiles of E2335 measured after the final annealing (Figure 17) clearly show that the titanite structure is only partially recovered and still heavily damaged.

E2312 titanite

Nanoindentation measurements at E2312 titanite indicate a material softening for T ≤ 950 K (Figure 23a) which could be a result of the shrinking amorphized regions in the structure (Salje et al., 2011b) and the ongoing recoordination of the Ti atoms in the structure. The subsequently material hardening at higher temperatures might be related to the advanced structural recovery of the titanite. These results are in good accordance with the results of resonance ultrasound spectroscopic measurements at metamict titanite (E2335) performed by Salje et al. (2011b). Metamict titanite E2312 has an average hardness value comparable to the value of Rauris titanite (Or.1) and higher than that of titanite glass (Figure 23a). The increasing E values allocate the rising crystallinity of the sample and approach the E values of fully crystalline Rauris titanite and are always higher than the E of titanite glass (Figure 23b). The different shapes of the nanoindents (Figure 25-29) are related to the different and changing (after each annealing step) material properties.

The diffraction profile of metamict titanite E2312 varies towards a nearly fully Gaussian shape (Figure 31). A higher Lorentzian shape contribution results from the diffuse part of the scattering correlated with the short-range order in the material whereas a high Gaussian shape contribution suggests a higher degree of long-range order (Chrosch et al., 1997). Increasing diffraction intensities at each annealing step (Figure 30) together with the reduction of the FWHM (Figure 31) confirm increasing correlation length in the crystal lattice with increasing annealing temperature and time. Because of low numbers of data points of the diffraction profiles the fits can only provide a tendency of the FWHM on annealing.

The increasing Raman intensities and the peak sharpening also indicate a recrystallization of the titanite structure (Figure 32). As in E2335 titanite a decrease in the wavenumber with rising annealing temperature of the peak related to Ti-O bond stretching (Figure 20) is also observed in E2312 titanite (near 632 cm^{-1}) (Figure 34) and may also indicate the decreasing Ti coordination, hence an increasing bond strength of the Ti-O bonds, with increasing crystallinity.

Metamict Allanite

As well as metamict titanite, metamict allanite recrystallizes at high temperatures. This is indicated by the results of the comparative powder XRD, synchrotron single-crystal XRD and IR spectroscopy studies. In contrast to titanite, allanite contains structural OH groups, but the results give no evidence for a remarkable influence on the recrystallization behavior.

Synchrotron single-crystal XRD measurements show, corresponding to the recrystallization of metamict material, the increasing intensity (Figure 36a) and the decreasing FWHM (Figure 36b,c) of the (007) reflection. This indicates an increasing correlation length with rising annealing temperature and time. Similar behavior of the $(1\bar{5}5)$ and $(35\bar{3})$ reflections confirm these results. Annealing at higher temperatures leads to a faster, and for longer annealing periods, to further recovery of the structural periodicity in allanite, as indicated by the results of the annealing experiment over a longer time period (2.6 h) at 823 K (Figure 37). A single kinetic mechanism should produce a linear trend in the Sharp-Hancock plot (e.g. Hancock and Sharp, 1972; Francis et al., 1999; Kiebach et al., 2005), and therefore, the results of the $(2\bar{2}2)$ reflection reveal that at least two distinct kinetic mechanisms are involved in the increase in the structural order of allanite during annealing (Figure 38). The obvious change in kinetics occurs at approximately ln(t) = 5.3, corresponding to ~200 s annealing at 823 K.

The increasing intensities of the Bragg peaks and the occurring of new sharp peaks in the measured powder XRD patterns with increasing annealing temperature also proof the recrystallization of metamict allanite R1 at higher temperatures (Figure 35).

As a result of the structural damage produced by alpha decay the Si-O tilting modes between 400 cm^{-1} and 600 cm^{-1} and the Si-O stretching mode between 900 cm^{-1} and 1100 cm^{-1} in the IR spectra of metamict allanite R1 remain heavily broadened at 723 K. First annealing to 823 K shows recrystallization effects, indicated by the increasing intensities of the Si-O tilting mode absorption bands (between 450 cm^{-1} and 700 cm^{-1}), as well as the Si-O stretching mode.

5 Conclusions

Metamict - recrystallization - increasing order

The structural state of heavily metamict natural titanite is highly anisotropic, indicating coherence between the different crystalline regions. Insofar, the structure of metamict titanite consists of a crystalline matrix with high degree of periodic faults and abundant amorphous nanoregions embedded in the matrix.

According to Raman spectroscopic studies the radiation-induced damages in the crystalline substance are related to the disturbance of SiO_4-TiO_6-SiO_4-TiO_6 rings including TiO_6 octahedra from different chains. The radiation-induced amorphization comprises the partial change of the coordination of Ti atoms from octahedral to pyramidal and/or tetrahedral, which in turn violates the Ti-O-Ti intrachain linkages. The results indicate that the affinity of the structure as a whole to accumulate radiation-induced defects, which leads to the development of amorphous regions, varies in the different crystallographic planes of titanite. The plane containing Si-O-Ti-O bond closed contours is less susceptible to a self-accumulation of induced defects as compared to the perpendicular plane, which contains chains of Ti-O bonds.

Raman spectra and XRD signals show that thermal annealing of the heavily damaged metamict M28696 Cardiff titanite sample for a relatively short period from RT to 825 K results in a slight recovery of the structure. The recovery of the long-range order is related to stiffness and improved local structure of SiO_4 tetrahedra, while the system of TiO_6 octahedra does not seem to be affected by this short annealing period.

Multistep annealing of metamict titanite E2335 by 50 K for 2 h per step gradually suppresses the structural defects occurring in the crystalline substance as the improvement of the SiO_4-TiO_6 connectivity within planes near perpendicular to the TiO_6 chains reaches saturation at ~ 900 K. The annealing-induced recrystallization process of the radiation-induced amorphous nanoregions begins at ~ 650 K, the process is most intense near 750 K, and considerably weakens above 950 K. The Raman scattering shows that annealing up to 1173 K is insufficient to fully recover the crystalline structure of the studied metamict titanite sample, which is in full accordance

with the results from Salje et al. (2011b) obtained by resonance ultrasound spectroscopy.

In their work Salje et al. (2011b) detected a softening of the same metamict titanite sample (E2335) until approximately 950 K. Recrystallization occurs in metamict titanite at annealing temperatures above 575 K. At these temperatures the amorphized beads embedded in the crystalline matrix of the metamict titanite structure begin to shrink by 3% (Salje et al., 2011b, 2012). The resulting volume reduction of the amorphized beads leads to a disconnection from the crystalline matrix, referred to as 'rattling', which may lead to the observed titanite softening in the temperature range between 600 and 1000 K. At temperatures above 1000 K Salje et al. (2011b) detected a hardening of the sample as a result of the recovery of the connections between the matrix and the beads, when amorphous intersections and amorphous islands vanish with increasing crystallinity of the system. These results are confirmed in this work by nanoindentation measurements at the metamict titanite sample E2312. The nanoindentation measurements integrate over contributions from amorphous areas and rims as well as from remaining crystalline material. The results show a decreasing average hardness of the titanite sample for an annealing temperature $\leq$ 950 K and further a hardening at higher temperatures. Together with the rising average elastic modulus the sample hardening is indicative for an increasing crystallinity of the titanite sample. The Raman spectroscopic studies on metamict titanite E2335 have shown that in the investigated temperature region the titanium coordination of a metamict sample increases on annealing from pyramidal and/or tetrahedral to octahedral. Raman measurements of metamict titanite E2312 support this assumption. It is assumed that the Ti coordination of the Ti-O bonds also influences the hardness of the sample. At first by softening because of the resulting decrease in the bond strength when the amorphous rims shrink. At a later stage by hardening because the ongoing recrystallization increases the structural order of the titanite sample.

Synchrotron experiments reveal the recrystallization of the metamict titanite samples during annealing when the FWHM values decrease on annealing following a linear trend from RT to 1220 K.

Metamict allanite was investigated because it contains in contrast to titanite structural OH groups, but the results of this study give no evidence for a marked

influence on the recrystallization behavior in relation to metamict titanite. As referred by Janeczek and Eby (1993) the recrystallization behavior of allanite is strongly influenced by the annealing atmosphere. In this study the atmosphere was air. The XRD patterns and IR spectra of metamict allanite R1 recorded during high-temperature thermal annealing show a marked increase in correlation length, which corresponds to structural recovery. As reported by Janeczek and Eby (1993) and Cobic et al. (2010) a decrease in the unit-cell volume during recrystallization is also observed. The results provide a corroboration of Janeczek and Eby (1993), who found that major changes in the crystallinity of metamict allanite occur within the first hour of annealing and that the change in the unit-cell volume of annealed allanite is $\leq$ 2%. The evolution of the FWHM (Figure 37c) and the increasing intensity of the $(2\bar{2}2)$ reflection (Figure 37b), as well as the reduction of the unit-cell volume (Figure 37d) of the metamict allanite sample R1, demonstrate that annealing for 600 s leads to considerable recovery at 823 K. After the rapid changes registered by XRD at the beginning of the thermal annealing, a plateau-like response to further annealing follows. This observation is consistent with previous experimental results of isothermal annealing performed by Paulmann and Bismayer (2001). Kinetic analysis following Sharp-Hancock shows that there are at least two different kinetic time scales: (1) an initial rapid annealing of probably aggregated Frenkel-defects with a correlated relaxation of the surrounding lattice, and (2) on a longer time scale for the rearrangement of more heavily damaged crystalline regions. During the annealing experiments at 823 and 1073 K, no chemical decomposition of allanite was observed. The decomposition temperature of allanite is, according to Janeczek and Eby (1993) and Cobic et al. (2010), 1123 - 1273 K. Cobic et al. (2010) undertook hydrothermal recrystallization experiments on metamict allanite and reported that the decomposition at higher annealing temperatures is related to the removal of structural H_2O.

References

Alberto, H.V., de Campos, N.A. and Mysen, B.O. (1995) The structural role of titanium in silicate glasses - a Raman-study of the system CaO-SiO_2-TiO_2. Physics and Chemistry of Glasses, 36, 114-122.

Armstrong, B.H. (1967) Spectrum line profiles: the Voigt function. Journal of Quantitative Spectroscopy and Radiative Transfer, 7, 61-88.

Bismayer, U. (1990) Hard mode Raman spectroscopy and its applications to ferroelastic and ferroelectric phase transitions. Phase Transitions, 27, 211-267.

Bismayer, U., Schmahl, W., Schmidt, C. and Groat, L. (1992) Linear Birefringence and X-Ray Diffraction Studies of the Structural Phase Transition in Titanite, $CaTiSiO_5$. Physics and Chemistry of Minerals, 19, 260-266.

Bismayer, U., Zhang, M., Groat, L.A., Salje, E.K.H. and Meyer, H.-W. (1999) The β-γ phase transition in titanite and the isosymmetric analogue in malayaite. Phase Transitions, 68, 545-556.

Bismayer, U., Paulmann, C., Groat, L. and Zhang, M. (2010) Local Phenomena in metamict Titanite. Acta Physica Polonica A, 117, 74-77.

Bonazzi, P. and Menchetti, S. (1994) Structural variations induced by heat-treatment in allanite and REE-bearing piemontite. American Mineralogist, 79, 1176-1184.

Chrosch, J., Bismayer, U. and Salje, E.K.H. (1997) Anti-phase boundaries and phase transitions in titanite: An X-ray diffraction study. American Mineralogist, 82, 677-681.

Chrosch, J., Colombo, M., Malcherek, T, Salje, E.K.H., Groat, L.A. and Bismayer, U. (1998) Thermal annealing of radiation damaged titanite. American Mineralogist, 83, 1083-1091.

Cobic, A., Bermanec, V. and Tomasic, N. (2010) The hydrothermal recrystallization of metamict allanite-(Ce). The Canadian Mineralogist, 48, 513-521.

Dollase, W.A. (1971) Refinement of the crystal structures of epidote, allanite and hancockite. American Mineralogist, 56, 447-464.

Dove, M.T. (2003) Structure and Dynamics: An atomic view of materials, Oxford University Press.

Dowty, E. (1987) Vibrational interactions of tetrahedra in silicate glasses and crystals: I. Calculations on ideal silicate-aluminate-germanate structural units. Physics and Chemistry of Minerals, 14, 80–93.

Ewing, R.C. (1987) The structure of the metamict state. Pp. 41-48 in: Second International Conference on Natural Glasses (J. Konta, editor). Charles University, Prague.

Ewing, R.C., Chakoumakos, B.C., Lumpkin, G.R. and Murakami, T. (1987) The metamict state. Materials Research Society Bulletin, 12, 58-66.

Ewing, R.C., Chakoumakos, B.C., Lumpkin, G.R., Murakami, T., Greegor, R.B. and Lytle, F.W. (1988) Metamict minerals: natural analogues for radiation damage effects in ceramic nuclear waste forms. Nuclear Instruments and Methods in Physics Research Section B: Beam Interactions with Materials and Atoms, 32, 487-497.

Ewing, R.C. (1994) The metamict state: 1993 – the centennial. Nuclear Instruments and Methods in Physics Research B, 91, 22-29.

Ewing, R.C., Meldrum, A., Wang L.M. and Wang, S.X. (2000) Radiation-induced amorphization. Reviews in Mineralogy and Geochemistry, P.H. Ribbe, series ed., Redfern, S.A.T. and Carpenter, M.A., eds., Washington, USA, Min. Soc. Am., 39, 319–361.

Ewing, R.C. (2007a) Ceramic matrices for plutonium disposition. Progress in Nuclear Energy, 49, 635-643.

Ewing, R.C. (2007b) Materials science - Displaced by radiation. Nature, 445, 161-162.

Ewing, R.C. (2008) Nuclear Fuel Cycle: Environmental Impact. Materials Research Society Bulletin, 33, 338-340.

Ewing, R.C. (2011) Actinides and radiation effects: impact on the back-end of the nuclear fuel cycle. Mineralogical Magazine, 75, 2359-2377.

Farges, F. (1997) Fivefold-coordinated Ti^{4+} in metamict zirconolite and titanite: A new occurrence shown by Ti K-edge XANES spectroscopy. American Mineralogist, 82, 44–50.

Farnan, I., Cho, H. and Weber W.J. (2007) Quantification of actinide α-radiation damage in minerals and ceramics. Nature, 445, 190-193.

Francis, R.J., O'Brien, S., Fogg, A.M., Halasyamani, P.S., O'Hare, D., Loiseau, T. and Ferey, G. (1999) Time-resolved in-situ energy and angle dispersive X-ray diffraction studies of the formation of the microporous gallophosphate ULM-5 under hydrothermal conditions. Journal of the American Chemical Society, 121, 1002-1015.

Geisler-Wierwille, T. (1999) U-Th-Gesamtblei-Datierung von Zirconen mit Hilfe der Elektronenstrahl-Mikrosonde: Methodik und Anwendungsbeispiele. Dissertation, Universität Hamburg.

Geisler, T. and Pidgeon R.T. (2002) Raman scattering from metamict zircon: comments on ‘‘Metamictisation of natural zircon: accumulation versus thermal annealing of radioactivity-induced damage’’ by Nasdala et al. 2001. Contributions to Mineralogy and Petrology, 143, 750-755.

Giacovazzo, C., Monaco, H.L., Artioli, G., Viterbo, D., Ferraris, G., Gilli, G., Zanotti, G. and Catti, M. (2002) Fundamentals of Crystallography Second Edition. Oxford University Press.

Groat, L.A., Hawthorne, F.C., Carter, R.T. and Ercit, T.S. (1985) Tantalian niobian titanite from the Irgon Claim, Southeast Manitoba. Canadian Mineralogist, 23, 569-57 l.

Hancock, J.D. and Sharp, J.H. (1972) Method of comparing solid-state kinetic data and its application to decomposition of kaolinite, brucite and $BaCO_3$. Journal of the American Ceramic Society, 55, 74-77.

Hawthorne, F.C. (1987) A general structural classification for oxy-salt minerals. Geological Association of Canada - Mineralogical Association of Canada, Abstracts with Program, 10, 30.

Hawthorne, F.C., Groat, L.A., Raudsepp, M., Ball, N.A., Kimata, M., Spike, F.D., Gaba, R., Halden, N.M., Lumpkin, G.R., Ewing, R.C., Greegor, R.B., Lytle, F.W., Ercit, T.S., Rossman, G.R., Wicks, F.J., Ramik, R.A., Sherriff, B.L., Fleet, M.E. and McCammon, C. (1991) Alpha-decay damage in titanite. American Mineralogist, 76, 370-396.

Heyns, A. M., Harden, P.M. and Prinsloo, L.C. (2000) Resonance Raman study of the high-pressure phase transition in chromium-doped titanite, $CaTiOSiO_4$. Journal of Raman Spectroscopy, 31, 837-841.

Higgins, J.B. and Ribbe, P.H. (1976) The crystal chemistry and space groups of natural and synthetic titanites. American Mineralogist, 61, 878-888.

Hollabaugh, C.L. and Rosenburg, P.E. (1983) Substitution of Ti for Si in titanite and new end-member cell dimensions for titanite. American Mineralogist, 68, 177-180.

Hollabaugh, C.L. and Foit, F.F. Jr. (1984) The crystal structure of an Al-rich titanite from Grisons, Switzerland. American Mineralogist, 69, 725-732.

Hughes, J.M., Bloodaxe, E.S., Hanchar, J.M. and Foord, E.E. (1997) Incorporation of rare earth elements in titanite: Stabilization of the A2/a dimorph by creation of antiphase boundaries. American Mineralogist, 82, 512-516.

Humlicek, J. (1982) Optimized computation of the Voigt and complex probability functions. Journal of Quantitative Spectroscopy and Radiative Transfer, 27, 437-444.

Jaggi, N. and Vij, D.R. (2006) Handbook of Applied Solid State Spectroscopy, chapter FOURIER TRANSFORM INFRARED SPECTROSCOPY, pages 411-450. Springer Science+Business Media, LLC New York.

Jahn, B.M., Wu, F.Y. and Chen, B. (2000) Massive granitoid generation in Central Asia: Nd isotope evidence and implication for continental growth in the Phanerozoic. Episodes, 23, 82-92.

Janeczek, J. and Eby, R.K. (1993) Annealing of radiation-damage in allanite and gadolinite. Physics and Chemistry of Minerals, 19, 343-356.

Joskow, P. and Parsons, E. (2012) The Future of Nuclear Power After Fukushima. Massachusetts Institute of Technology Center for Energy and Environmental Policy Research Working Paper, WP-2012-001, 1-30.

Kek, S., Aroyo, M., Bismayer, U., Schmidt, C., Eichhorn, K. and Krane, H.G. (1997) The two-step phase transition of titanite, CaTiSiO5: a synchrotron radiation study. Zeitschrift für Kristallographie, 212, 9-19.

Kiebach, R., Schaefer, M., Porsch, F. and Bensch, W. (2005) In-situ energy dispersive X-ray diffraction studies of the crystallization of (1,2-$DAPH_2)_2Ge_9(OH)_4O_{18}\cdot 2H_2O$ under solvothermal conditions. Zeitschrift für anorganische und allgemeine Chemie, 631, 369-374.

Kiefer, W. (1995) Spektroskopie amorpher und kristalliner Festkörper, chapter Raman-Spektroskopie, pages 117-147. Dr. Dietrich Steinkopff Verlag, GmbH & Co. KG Darmstadt.

Kostov-Kytin, V., Mihailova, B., Kalvachev, Yu. and Tarassov, M. (2005) Atomic arrangements in amorphous sodium titanosilicate precursor powders. Microporous and Mesoporous Materials, 86, 223-230.

Kroumova, E., Aroyo, M.I, Perez-Mato, J.M., Kirovm A., Capillas, C., Ivantchev, S. and Wondratschek, H. (2003) Bilbao Crystallographic Server: Useful Databases and Tools for Phase-Transition Studies. Phase Transitions**,** 76, 155-170.

Lumpkin, G.R., Eby, R.K. and Ewing, R.C. (1991) Alpha-recoil damage in titanite ($CaTiSiO_5$): Direct observation and annealing study using high resolution transmission electron microscopy, Journal of Materials Research, 6, 560-564.

Malcherek, T., Domeneghetti, C.M., Tazzoli, V., Salje, E.K.H. and Bismayer, U. (1999) A high temperature diffraction study of synthetic titanite $CaTiOSiO_4$. Phase Transitions, 69, 119-131.

Malcherek, T., Paulmann, C., Domeneghetti, M.C. and Bismayer, U. (2001) Diffuse scattering anisotropy and the $P2_1/a$ – A2/a phase transition in titanite, $CaTiOSiO_4$. Journal of Applied Crystallography, 34, 108-113.

Malczewski, D. and Grabias, A. (2008) Fe-57 Mössbauer spectroscopy of radiation damaged allanites. Acta Physica Polonica A, 114, 1683-1690.

Meyer, H.W., Zhang, M., Bismayer, U., Salje, E.K.H., Schmidt, C., Kek, S., Morgenroth, W. and Bleser, T. (1996) Phase transformation of natural titanite: An infrared, Raman spectroscopic, optical birefringence and X-ray diffraction study. Phase Transition, 59, 39-60.

Mitchell, R.S. (1973) Metamict minerals: a review. Mineralogical Record, 4, 177-223.

Moenke, H. (1962) Mineralspektren. Akademie-Verlag, Berlin.

Momma, K. and Izumi, F. (2008) VESTA: a three-dimensional visualization system for electronic and structural analysis. Journal of Applied Crystallography, 41, 653-658.

Muir, I.J., Metson, J.B. and Bancroft, G.M. (1984) 57Fe Mössbauer spectra of perovskite and titanite. Canadian Mineralogist, 22, 689-694.

Muller, I. and Weber, W.J. (2001) Plutonium in crystalline ceramics and glasses. Materials Research Society Bulletin, 26, 698-706.

Nasdala, L., Wenzel, M., Vavra, G., Irmer, G., Wenzel, T. and Kober, B. (2001) Metamictization of natural zircon: accumulation versus thermal annealing of radioactivity-induced damage. Contribution to Mineralogy and Petrology, 141, 125-144.

Nasu, H., Kurachi, K., Mito, A., Matsuoka, J. and Kamiya, K. (1997) Second harmonic generation and structure of mixed alkali titanosilicate glasses. Journal of Non-Crystalline Solids, 217, 182-188.

Oliver, W.C. and Pharr, G.M. (2004) Measurement of hardness and elastic modulus by instrumented indentation: Advances in understanding and refinements to methodology. Journal of Materials Research, 19, 3-20.

Otwinowski, Z. and Minor, W. (1997) Processing of X-ray diffraction data collected in oscillation mode. Methods in Enzymology, 276, 307-326.

Paul, B.J., Cerny, P., Chapman, R. and Hinthorne, J.R. (1981) Niobian titanite from the Huron Claim Pegmatite, Southeastern Manitoba. Canadian Mineralogist, 19, 549-552.

Paulmann, C., Bismayer, U. and Groat, L.A. (2000) Thermal annealing of metamict titanite: A synchrotron radiation and optical birefringence study. Zeitschrift für Kristallographie, 215, 678-682.

Paulmann, C. and Bismayer, U. (2001) Anisotropic recrystallization effects in metamict allanite on isothermal annealing. Hasylab Annual Report 2001, 435-436.

Pharr, G.M. (1998) Measurement of mechanical properties by ultra-low load indentation. Materials Science Engineering, A253, 151-159.

Putnis, A. (1992) Introduction to Mineral Sciences. Cambridge University Press.

Raman, C.V. and Krishnan, K.S. (1928) A new type of secondary radiation. Nature, 121, 501-502.

Rollinson, H.R. (1993) Using Geochemical Data: Evaluation, Presentation, Interpretation, chapter Geochemical data, pages 10-12, 15-16. Person Education Limited.

Salje, E.K.H., Schmidt, C. and Bismayer, U. (1993) Structural Phase Transition in Titanite, $CaTiSiO_5$: A Ramanspectroscopic Study. Physics and Chemistry of Minerals, 19, 502-506.

Salje, E.K.H. and Bismayer, U. (1997) Hard Mode Spectroscopy: The Concept and Applications. Phase Transitions, 63, 1-75.

Salje, E.K.H., Safarik, D.J., Taylor, R.D., Pasternak, M.P., Modic, K.A., Groat, L.A. and Lashley, J.C. (2011a) Determination of iron sites and the amount of amorphization in radiation-damaged titanite ($CaTiSiO_5$). Journal of Physics: Condensed Matter, 23, 105402 (3pp).

Salje, E.K.H., Safarik, D.J., Lashley, J.C., Groat, L.A. and Bismayer, U. (2011b) Elastic softening of metamict titanite $CaTiSiO_5$: Radiation damage and annealing. American Mineralogist, 96, 1254-1261.

Salje, E.K.H., Taylor, R.D., Safarik, D.J., Lashley, J.C., Groat, L.A., Bismayer, U., Evans, R.J. and Friedman, R. (2012) Evidence for direct impact damage in metamict titanite $CaTiSiO_5$. Journal of Physics: Condensed Matter, 24, 1-5.

Schreier, F. (1992) The Voigt and complex error function: a comparison of computational methods. Journal of Quantitative Spectroscopy and Radiative Transfer, 48, 743-762.

Speer, J.A. and Gibbs, G.V. (1976) The crystal structure of synthetic titanite, $CaTiOSiO_4$, and the domain texture of natural titanites. American Mineralogist, 61, 238-247.

Stefanovsky, S.V., Yudintsev, S.V., Nikonov, B.S., Omelianenko, B.I. and Lapina, M.I. (2000) Isomorphic Capacity of Synthetic Sphene with Respect to Gd and U. Materials Reasearch Society Symp. Proc., 608, 455-460.

Steiger, R.H. and Jäger, E. (1977) Subcommission on Geochronology: Convention on the use of decay constants in Geo- and Cosmochronology. Earth and Planetary Science Letters, 36, 359-362.

Su, Y., Balmer, M.L. and Bunker, B.C. (2000) Raman Spectroscopic Studies of Silicotitanates. Journal of Physical Chemistry B, 104, 8160-8169.

Tanaka, I., Obuchi, T. and Kohima, H. (1988) Growth and characterization of titanite ($CaTiSiO_5$) single crystals by the floating zone method. Journal of Crystal Growth, 87, 169–174.

Taylor, M. and Brown, G.E. (1976) High-temperature structural study of the $P2_1/a \leftrightarrow$ A2/a phase transition in synthetic titanite, $CaTiSiO_5$. American Mineralogist, 61, 435-447.

Trachenko, K.O., Dove, M.T. and Salje, E.K.H (2001) Atomistic modeling of radiation damage in zircon. Institute of Physics Publishing, 13, 1947-1959.

Vance, E.R. and Metson, J.B. (1985) Radiation Damage in Natural Titanites. Physics and Chemistry of Minerals, 12, 255-260.

Vance, E.R., Carter, M.L., Begg, B.D., Day, R.A. and Leung, S.H.F. (2000) Solid Solubilities of Pu, U, Hf, and Gd in Candidate Ceramic Phases for Actinide Waste Immobilization. Materials Reasearch Society Symp. Proc., 608, 431-436.

Vladimirov, A.G., Ponomareva, A.P., Shokalskii, S.P., Khalilov, V.A., Kostitsyn, Y.A., Ponomarchuk, V.A. Rudnev, S.N., Vystavnoi, S.A., Kruk, N.N. and Titov, A.V. (1997) Late Paleozoic early Mesozoic granitoid magmatism in Altai. Geologiya & Geofizika, 38, 715-729.

Weber, W.J. (1990) Radiation-induced defects and amorphization in zircon. Journal of Materials Research, 5, 2687-2697.

Weber, W.J., Ewing, R.C., Angell, C.A., Arnold, G.W., Cormack, A.N., Delaye, J.M., Griscom, D.L., Hobbs, L.W., Navrotsky, A., Price, D.L., Stoneham, A.M. and Weinberg, W.C. (1997) Radiation effects in glasses used for immobilization of high-level waste and plutonium disposition. Journal of Materials Research, 8, 1946-1978.

Weber, W.J., Ewing, R.C., Catlow, C.R.A., de la Rubia, T.D., Hobbs, L.W., Kinoshita, C., Matzke, H., Motta, A.T., Nastasi, M., Salje, E.K.H., Vance, E.R. and Zinkle, S.J. (1998) Radiation effects in crystalline ceramics for the immobilization of high-level nuclear waste and plutonium. Journal of Materials Research, 6, 1434-1484.

Weber, W.J., Navrotsky, A., Stefanovsky, S., Vance, E.R. and Vernaz, E. (2009) Materials Science of High-Level Nuclear Waste Immobilization. Materials Research Society Bulletin, 34, 46-53.

Zhang, M., Salje, E.K.H., Bismayer, U., Unruh, H.-G., Wruck, B. and Schmidt, C. (1995) Phase Transition(s) in Titanite $CaTiSiO_5$: An Infrared Spectroscopic, Dielectric Response and Heat Capacity Study. Physics and Chemistry of Minerals, 22, 41-49.

Zhang, M., Salje, E.K.H. and Bismayer, U. (1997) Structural phase transition near 825 K in titanite: Evidence from infrared spectroscopic observations. American Mineralogist, 82, 30-35.

Zhang, M., Salje, E.K.H., Malcherek, T., Bismayer, U. and Groat, L.A. (2000) Dehydration of metamict titanite: an infrared spectroscopic study. The Canadian Mineralogist, 38, 119-130.

Zhang, M., Salje, E.K.H., Bismayer, U., Groat, L.A. and Malcherek, T. (2002) Metamictization and recrystallization of titanite: An infrared spectroscopic study. American Mineralogist, 87, 882-890.

Curriculum vitae

entfällt aus datenschutzrechtlichen Gründen

List of publications

Beirau, T., Mihailova, B., Matveeva, G., Kolb, U., Malcherek, T., Groat, L. and Bismayer, U. Structural anisotropy and annealing-induced nanoscale atomic rearrangements in metamict titanite. American Mineralogist, in print 2012.

Angel, R., **Beirau, T.**, Mihailova, B., Paulmann, C. and Bismayer, U. The role of lone pairs in the ferroelastic phase transition in the palmierite-type lead phosphate-arsenate solid solution. Zeitschrift für Kristallographie, in print 2012.

Beirau, T., Paulmann, C. and Bismayer, U. (2011) Recrystallization of metamict allanite. Mineralogical Magazine, 75, 2393-2399.

Beirau, T., Bismayer, U., Mihailova, B., Paulmann, C. and Groat, L. (2010) Structural phenomena of metamict titanite: a synchrotron, X-ray diffraction and vibrational spectroscopic study. Phase Transitions, 83, 694-702.

Salje, E.K.H., **Beirau, T.**, Mihailova, B. and Bismayer, U. (2010) Chemical mixing and hard mode spectroscopy in ferroelastic lead phosphate-arsenate: local symmetry splitting and multiscaling behavior. J. Physics: Condensed Matter, 22, 045403 (6pp).

Contributions to conferences

Beirau, T., Mihailova, B., Paulmann, C. and Bismayer, U. Annealing behavior of radiation damaged minerals. In Deutsche Gesellschaft für Kristallographie Jahrestagung 2012, Munich, Germany, March 2012. Poster presentation.

Beirau, T., Paulmann, C., Mihailova, B. and Bismayer, U. Kinetic behaviour of metamict titanite and allanite. In Conference: Geological Disposal of Radioactive Waste: Underpinning Science and Technology, Loughborough, United Kingdom, October 2011. Poster presentation.

Beirau, T., Paulmann, C., Mihailova, B. and Bismayer, U. Metamict systems - amorph to crystalline. In 1. Berichtskolloquium DFG-Schwerpunktprogramm SPP 1415, Boppard, Germany, October 2011. Oral and poster presentation.

Beirau, T., Paulmann, C., Mihailova, B. and Bismayer, U. Recrystallisation behaviour and structural phenomena of metamict titanite. In Deutsche Mineralogische Gesellschaft, Deutsche Gesellschaft für Kristallographie und Österreichische Mineralogische Gesellschaft Jahrestagung 2011, Salzburg, Austria, September 2011. Oral presentation.

Beirau, T., Paulmann, C., Mihailova, B. and Bismayer, U. Metamictisation vs Crystallinity. In DFG-Schwerpunktprogramm SPP 1415 Winterschool: Theorie und Simulation von Festkörpern und ihren Eigenschaften, Eisenach, Germany, March 2011. Poster and short oral presentation.

Beirau, T., Paulmann, C., Mihailova, B. and Bismayer, U. Metastability and crystallization of metamict minerals. In BMBF Small-scale Russian-German-Workshop, Hamburg, Germany, December 2010. Oral presentation.

Beirau, T., Paulmann, C., Mihailova, B. and Bismayer, U. Re-equilibration and structural recovery of metamict titanite. In Mineralogical Society Annual Conference: Nuclear Waste Management: Research Challenges for the future, Cambridge, United Kingdom, September 2010. Poster and short oral presentation.

Beirau, T., Paulmann, C., Mihailova, B. and Bismayer, U. Recrystallization of Metamict Titanite. In Deutsche Mineralogische Gesellschaft Jahrestagung 2010, Münster, Germany, September 2010. Poster presentation.

Beirau, T., Paulmann, C., Mihailova, B. and Bismayer, U. Metamict titanite. In European Crystallographic Meeting 26, Darmstadt, Germany, August 2010. Poster presentation.

Beirau, T., Paulmann, C., Mihailova, B. and Bismayer, U. Metastabilität und Kristallisation metamikter Minerale. In DFG-Schwerpunktprogramm SPP 1415 Tagung, Bad Staffelstein, Germany, June 2010. Oral presentation.

HASYLAB Annual Reports

Beirau, T., Paulmann, C. and Bismayer, U. (2010) Recrystallization effects in metamict titanite on progressive annealing. Hasylab Annual Report 2010.

Beirau, T., Paulmann, C. and Bismayer, U. (2010) Re-equilibration and structural recovery of metamict allanite. Hasylab Annual Report 2010.

Acknowledgements

I would particularly like to thank my supervisors Prof. Dr. Ulrich Bismayer and Dr. habil. Boriana Mihailova for their great support and guidance during the three years of my PhD studies.

I am also grateful for the help received from Dr. Carsten Paulmann, Dr. Thomas Malcherek from the University of Hamburg and Dr. Bernd Maier from the University of Munich.

I like to thank Prof. Dr. Lee A. Groat from the University of British Colombia for providing the metamict titanite samples and Prof. Dr. Gerold Schneider and his PhD student Paula Guglielmi from the Technical University Hamburg Harburg for the possibility to perform nanoindentation measurements at their institute and their assistance during the measurements.

For technical and experimental support I like to thank Dipl.-Min. Stefanie Heidrich, Peter Stutz and Joachim Ludwig from the University of Hamburg.

Finally I like to thank my girlfriend Sabrina, my parents and my brother for their great support.

This work was financially supported by the Deutsche Forschungsgemeinschaft via the Schwerpunktprogramm 1415 Kristalline Nichtgleichgewichtsphasen (KNG) - Präparation, Charakterisierung und in situ-Untersuchung der Bildungsmechanismen which is gratefully acknowledged by the author.